



This is to certify that the

dissertation entitled

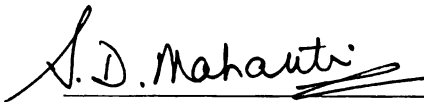
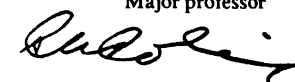
"Studies of the Magnetic Properties of Clay
Intercalation Compounds and Diffusion of
Inert Gases in Mixed Ion Systems"

presented by

Ping Zhou

has been accepted towards fulfillment
of the requirements for

Ph.D. degree in Physics


Major professor


Date July 25, 1991

**LIBRARY
Michigan State
University**

**PLACE IN RETURN BOX to remove this checkout from your record.
TO AVOID FINES return on or before date due.**

DATE DUE	DATE DUE	DATE DUE
_____	_____	_____
_____	_____	_____
_____	_____	_____
_____	_____	_____
_____	_____	_____
_____	_____	_____
_____	_____	_____

MSU is An Affirmative Action/Equal Opportunity Institution

c:\circ\datedue.pm3-p.1

**STUDIES OF THE MAGNETIC PROPERTIES OF CLAY INTERCALATION COMPOUNDS
AND DIFFUSION OF INERT GASES IN MIXED ION SYSTEMS**

By

Ping Zhou

A DISSERTATION

Submitted to

Michigan State University

in partial fulfillment of the requirements

for the degree of

DOCTOR OF PHILOSOPHY

Department of Physics and Astronomy

1991

115-899

ABSTRACT

STUDIES OF THE MAGNETIC PROPERTIES OF CLAY INTERCALATION COMPOUNDS
AND DIFFUSION OF INERT GASES IN MIXED ION SYSTEMS

By

Ping Zhou

The magnetic properties of a clay layered silicate, vermiculite (ver), intercalated with 3d transition metal ions (Mn^{2+} , Co^{2+} , Ni^{2+} and Cu^{2+}) as interlayer cations have been investigated by studies of the magnetic susceptibility of these compounds. The paramagnetic behavior of these magnetic ions in vermiculite with and without water molecules coexisting in the gallery has been analyzed by using crystal field theory. Numerical estimations of the crystal field strength with and without water have been obtained from the Lande g factor measured from the susceptibility. A substantial decrease of crystal field strength has been observed when water molecules are removed from the gallery.

Mn^{2+} -ver and Cu^{2+} -ver are found to be paramagnetic systems for temperatures down to 2K regardless of the hydration conditions. Although Co^{2+} -ver and Ni^{2+} -ver do not exhibit magnetic ordering while water is present in the gallery, they show indications of antiferromagnetic ordering at temperatures of a few Kelvin after water is removed. The physical origin for such behavior has been discussed

from the considerations of anisotropy from spin-orbit coupling and properties of various magnetic systems in different spatial dimensions.

In order to examine the percolation phenomenon in two dimensional microporous media, we also have carried out a study of diffusion of Helium and Argon in a mixed ion layered system $[\text{Co}^{3+}(\text{en})_3]_{1-x}[\text{Cr}^{3+}(\text{en})_3]_x$ -FHT, here en is ethylenediamine and FHT is a layered silicate called fluorohectorite. The mass uptake of argon in this system indicates a percolation threshold at $x_c = 0.8$. We have observed the complete blockage of Argon by enlarged cations for the first time which shows a strong evidence of dynamical movement of argon in the gallery spaces.

ACKNOWLEDGMENTS

I would like to express my deepest gratitude to my thesis advisor Professor Stuart A. Solin, whose intuitive insight and inspirations have guided me through out all my graduate school years. Without his supports, this work would not be possible.

I also would like to thank Professor S.D. Mahanti whose help and advises have enabled me to go through the last stage of my thesis work. I am also very grateful to Professor T.J. Pinnavaia for his invaluable help on the sample preparation and analysis. The collaboration with him and his group in chemistry department is crucial to my thesis work. Especially Dr. J. Amarasekera is acknowledged for his assistant help on the sample synthesis.

I would like to thank Professor M. Thorpe and Professor J. Cowen for their advises on magnetism in solids and crystal field theory. Also the discussions with my friends and colleagues Dr. M. Holtz, T.Y. Park, Carrie Huang, Y.B.Fan, X.W. Qian are also very valuable to me. I thank Vivion E. Shull for his assistant in using the electron microscope and Reza Loloee for his help in using the SQUID.

Finally, I like to acknowledge the financial support from NSF, Center for Fundamental Material Research and Department of Physics and Astronomy at Michigan State University.

This thesis is dedicated to my wife who has spent countless lonely hours during all these years.

TABLE OF CONTENTS

Chapter	I.	Overview.....	1
	I.1	Layered intercalation compounds.....	1
	I.2	Magnetism in solids.....	4
	I.3	Scope of the Thesis.....	9
Chapter	II	Structure of vermiculite and fluorohectorite.....	11
Chapter	III	The DC magnetic susceptibility of vermiculite intercalation compounds with 3d metal ions as intercalants.....	19
	III.1	Introduction.....	19
	III.2	Experiments.....	20
	III.3	Results of the DC magnetic susceptibility of vermiculite with magnetic intercalants.....	29
	III.4	Remarks.....	38
Chapter	IV	Crystal field, exchange interaction, and phase transition in vermiculite intercalation compounds with 3d metal ions as intercalants.....	41
	IV.1	Introduction.....	41
	IV.2	Lande g factors and anisotropic Hamiltonian.....	41
	IV.3	The exchange interaction between magnetic ions and magnetic phase transition.....	56
	IV.4	Concluding remarks.....	65
Chapter	V	Diffusion and absorption of inert gases in a mixed ion system.....	67
	V.1	Introduction.....	67

V.2	Experiment and results.....	73
V.3	Discussion.....	85
V.4	Concluding remarks.....	96
Appendix I	Divalent Co and Ni ions in an octahedral crystal field with a trigonal distortion along the C_3 axis..	97
Appendix II	Divalent Cu ion in an octahedral crystal field with a trigonal distortion along the C_3 axis.....	104
Reference.....		108
List of publications.....		111

LIST OF TABLES

<u>Table</u>	<u>Page</u>
I.1	Magnetic ordering of different systems in different spatial dimensions.8
III.1	Parameters for Mn ²⁺ -ver obtained from a least square fit to the Curie-Weiss formula.31
III.2	Parameters for Co ²⁺ -ver obtained from a least square fit to the Curie-Weiss formula.34
III.3	Parameters for Ni ²⁺ -ver obtained from a least square fit to the Curie-Weiss formula.37
III.4	Parameters for Cu ²⁺ -ver obtained from a least square fit to the Curie-Weiss formula.40
IV.1	The Lande g factor calculated from the effective moments of different ions under different hydration conditions.43
IV.2	The crystal field strength 10Dq and Dt (unit cm ⁻¹) Calculated from the g factors of Co ²⁺ and Ni ²⁺ for different hydration conditions. Furthermore, g values for Cu ²⁺ ions were obtained from these parameters.55
IV.3	The Curie's temperatures for all ions in vermiculite.57
V.1	Porosity sets and their corresponding behaviors.70
V.2	Dimensions of pillaring agents.71
V.3	Parameters for Helium in the unannealed Co ³⁺ (en) ₃ -FHT membrane.88

Table

Page

V.4 Parameters for Helium in the annealed $\text{Co}^{3+}(\text{en})_3\text{-FHT}$ membrane.91

V.5 Parameters for Argon in the unannealed $\text{Co}^{3+}(\text{en})_3\text{-FHT}$ membrane.94

V.6 Diffusion coefficients for Helium and Argon in the $\text{Co}^{3+}(\text{en})_3\text{-FHT}$ membrane.95

LIST OF FIGURES

<u>Figure</u>	<u>Page</u>
I.1	Classification of layered intercalation compounds.2
I.2	Relations of four conventional exchange couplings.6
II.1	Schematic view of a 2:1 layered silicate.12
II.2	Schematic view of the Kagome lattice formed by the basal oxygen atoms.14
II.3	The stacking sequence in vermiculite.16
II.4	The staggering between two basal oxygen planes shifted relatively by $b/3$17
III.1	The x-ray diffraction pattern for Mg^{2+} -ver, $(CH_3)_3NH^+$ -ver and Co^{2+} -ver at ambient conditions.22
III.2	The weight loss of Co^{2+} -ver and Mg^{2+} -ver versus T measured by the TGA method.24
III.3	The x-ray diffraction patterns for Co^{2+} -ver and Ni^{2+} -ver before and after annealing.25
III.4	The inverse susceptibility, $\chi^{-1}(T)$, of hydrated Mg^{2+} -ver versus T.27
III.5	The inverse susceptibility, $\chi^{-1}(T)$, of Mn^{2+} -ver under different hydration conditions.30
III.6	The dc magnetic susceptibility $\chi(T)$ and its inverse of Co^{2+} -ver under different hydration conditions.33
III.7	The dc magnetic susceptibility $\chi(T)$ and its inverse of

<u>Figure</u>	<u>Page</u>
Ni ²⁺ -ver under different hydration conditions.	36
III.8 The dc magnetic susceptibility $\chi(T)$ of Cu ²⁺ -ver under different hydration conditions.	39
IV.1 Schematic illustration of a gallery cation surrounded by six water molecules at ambient conditions.	48
IV.2 The Kagome lattice with in plane distortion.	62
IV.3 A rectangular Ising system with anisotropic interactions. ..	64
V.1 The inplane structure of $[\text{Co}^{3+}(\text{en})_3]_{1-x}[\text{Cr}^{3+}(\text{en})_3]_x$ -FHT. ...	75
V.2 The x-ray diffraction patterns of $\text{Co}^{3+}(\text{en})_3$ -FHT before and after annealing.	76
V.3 The surface morphology of film and bulk $\text{Co}^{3+}(\text{en})_3$ -FHT.	77
V.4 Three possible path ways for Argon to diffuse in a $\text{Co}^{3+}(\text{en})_3$ -FHT film.	79
V.5 Schematic illustration of the experimental set up for mass conduction measurement.	80
V.6 The amount of Argon absorbed by $[\text{Co}^{3+}(\text{en})_3]_{1-x}[\text{Cr}^{3+}(\text{en})_3]_x$ -FHT and by the physical mixture of the pure samples.	82
V.7 Helium partial pressure in the sampling chamber versus T. The membrane is unannealed.	83
V.8 Argon partial pressure in the sampling chamber before and after the $\text{Co}^{3+}(\text{en})_3$ -FHT film has been annealed.	84

<u>Figure</u>	<u>Page</u>
V.9	Helium partial pressure in the sampling chamber for different applied pressures after the $\text{Co}^{3+}(\text{en})_3$ -FHT film has been annealed.90
V.10	Argon partial pressure in the sampling chamber for different applied pressures before the $\text{Co}^{3+}(\text{en})_3$ -FHT film has been annealed.93
AI.1	Energy splitting of a Ni^{2+} ion in an O_h field with a trigonal distortion.103
AII.2	Energy splitting of a Cu^{2+} ion in an O_h field with a trigonal distortion.107

Chapter I

Overview

I.1 Layered intercalation compounds

Layered intercalation compounds have been the objects of interest for scientists for many years. Intercalation means the insertion of guest species into a layered material without disturbing the main structural features of the host.¹ The guest species are called intercalants. These layered systems are interesting because they provide a two dimensional arena to study physical properties such as magnetism, percolation, electronic structure, optical and vibrational properties and so on. They also have potential for practical applications such as hydrogen storage,² batteries,³ catalysis^{4,5} etc.

There are many different ways to characterize layered intercalation compounds depending on the physical properties one is interested in. One can classify them into three classes by looking at the rigidity of the layers themselves (see figure I.1).⁶ Class I contains "floppy" layer hosts. Such materials for example can be graphite intercalation compounds (GIC) or boron nitride. Materials in class II have layers with intermediate stiffness. Examples are layered dichalcogenides such as TiS_2 , HfS_2 , FeCl_2 , CoCl_2 , and FeOCl -type compounds, etc.⁷ These two classes of layered intercalation compounds show an unusual "staging effect" meaning that two adjacent intercalant layers are separated by a fixed number of host layers.⁸ In the case of graphite the number of the host layers (called stage number) between two intercalant layers can be from one up to more than ten depending on the conditions under which the

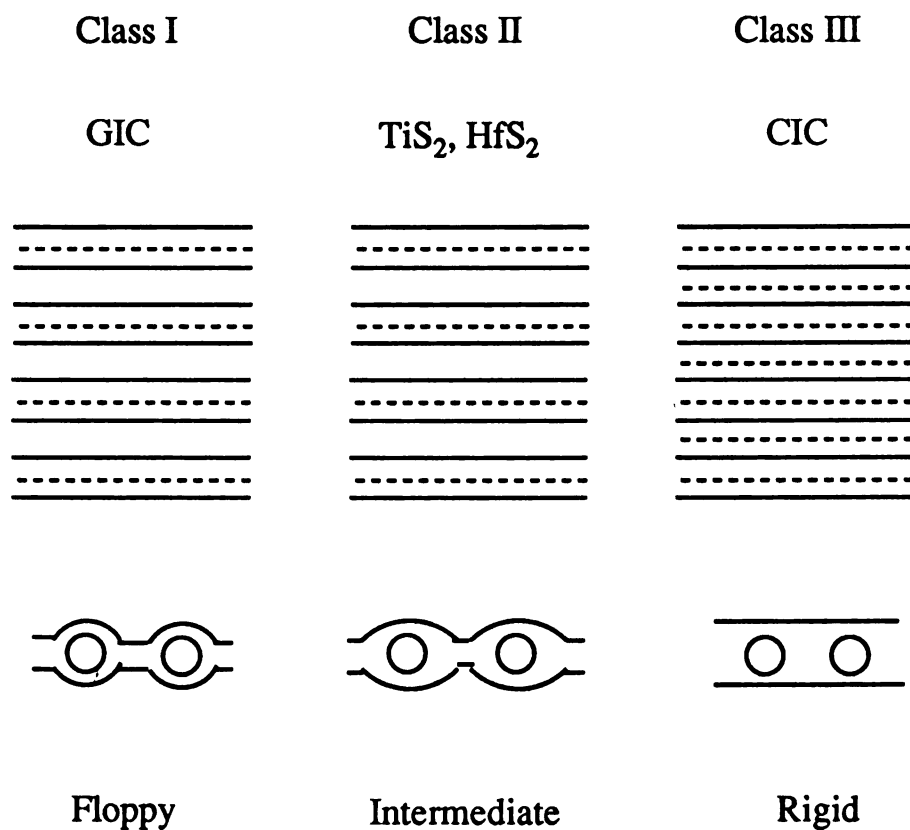


Figure I.1 Classification of layered intercalation compounds. Solid lines represent host layers. Dashed lines are intercalants. GIC/CIC stands for graphite/clay intercalation compounds.

samples are made.

Clay intercalation compounds (CIC) represent examples of class III layered materials which have the stiffest layers. The layers in these materials can be pillared by intercalants which are laterally far apart. In most clay intercalation compounds, the gallery height is comparable to the size of intercalant indicating that the host layers are stiff and are propped apart. There is no staging effect in CIC compounds with only one kind of intercalant. For some CIC compounds with two or more different intercalants, the guest species segregate to form domains or form separate layers of each kind between host layers. This effect called interstratification is caused by the difference of either the size or the charge of the intercalants.

Clay intercalation compounds are ideal for studies of physical properties in lower dimensions. One particular interest is the magnetic properties of these layered compounds with magnetic species inside the gallery. They have several distinctive features compared with other classes of intercalation compounds. First of all, in most clays, there is some unbalanced negative charge in the host layers. These charges are compensated by positively charged intercalants in the gallery spaces. These gallery intercalants can be replaced by various ions including magnetic ions whose collective magnetic properties are determined by their locations in the host gallery. In contrast, other magnetic intercalation compounds such as graphite intercalation compounds exhibit magnetic properties of the pristine guest. An example can be CoCl_2 -Graphite in which sandwich-like Cl-Co-Cl layers are intercalated between the neutral graphite layers.⁹⁻¹² The magnetic properties of this compound are dominated by the mechanism which obtains

in bulk CoCl_2 . Thus, clay intercalation compounds provide a better two dimensional arena in which we can intercalate magnetic ions directly into the interlamellar gallery spaces. Secondly, we can control the magnetic moments and the distance between magnetic ions in CIC by intercalating ions with different spins and charges. Thirdly, clay intercalation compounds readily accept water layers inside the gallery spaces.^{13,14} At ambient conditions, there are generally two layers of water molecules coexisting with intercalants in the gallery of most CIC compounds. The number of water layers can be reduced to one or zero when these compounds are heated or water vapor pressure is reduced. These water molecules affect the magnetic properties in a very complicated way. Nevertheless, they still provide a channel to manipulate the interaction between magnetic intercalants.

I.2 Magnetism in solids

Magnetism in solids has been extensively studied in many different systems. Besides the classic dipole-dipole interaction, there is an exchange interaction between two spins. The mechanism of the exchange interaction was investigated first by Heisenberg¹⁵ whose famous Hamiltonian is

$$H_{\text{ex}} = -2 \sum_{i,j} J_{i,j} \hat{\mathbf{s}}_i \cdot \hat{\mathbf{s}}_j \quad (\text{I.1})$$

where $J_{i,j}$ is the exchange interaction energy between two spins. A positive $J_{i,j}$ results in ferromagnetic alignment of spins while a negative $J_{i,j}$ causes antiferromagnetic alignment of spins.

Many investigations for exchange interaction have been initiated and various mechanisms have been developed in order to explain the magnetic behaviors of different systems including transition metals, rare earth metals, and insulators with magnetic ions. Figure I.2 shows all types mechanism which have been applied to various systems.¹⁵ In transition metals and rare earth metals, the spins are delocalized. Their magnetic behaviors are complicated and can be explained by theories involving the itinerancy of these electrons. In magnetic insulators, the spins can be treated as localized moments. In our study here, we only concern the spin-localized systems.

Magnetic properties of insulator such as transition metal oxides and rare earth metal salts are straightforward and systematic. It has been found that almost all 3d and 4f ionic salts are antiferromagnetic with only one exception, EuO ¹⁹. To explain this universal behavior, Kramers²⁰ and Anderson^{21,22} invoked the superexchange mechanism in 1950s. In this theory, virtual transfer of an electron from one lattice site to another through a ligand is crucial and results in antiferromagnetism. It agrees qualitatively with experimental results on these ionic salts. Quantitative first-principles estimation of the exchange energy is more complicated than expected due to various correlations and many-body effects.

The magnetic response of the above systems at different temperatures have been well studied. When $k_B T$ is higher than the magnetic coupling between spins, a system will behave paramagnetically. The magnetic susceptibility χ follows follows the so-called Curie-Weiss law:

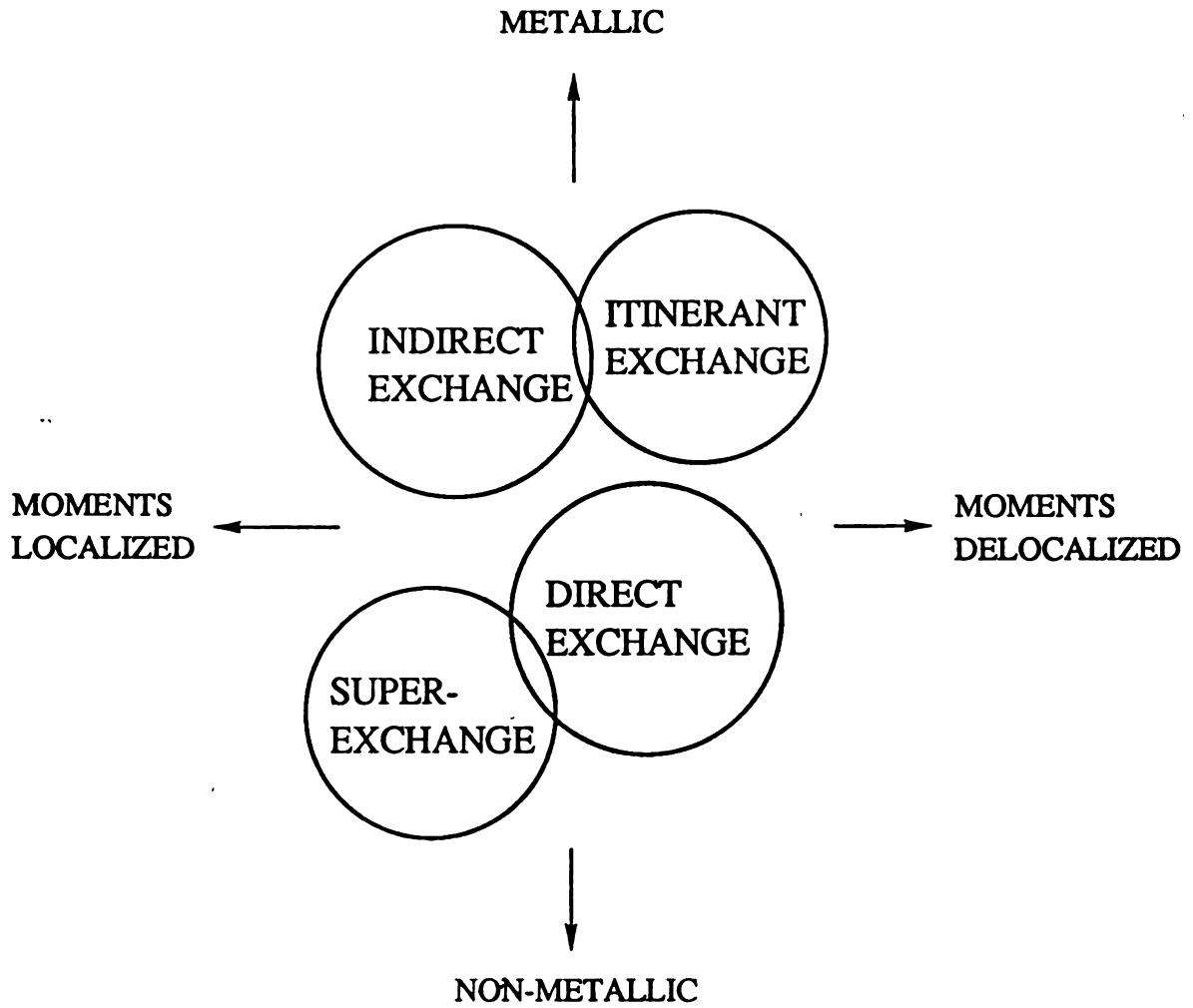


Figure I.2 Relations of four conventional exchange couplings. Each cricle represents a different central idea.

$$\chi = \frac{C}{T - \theta} \quad (\text{I.2})$$

where θ is the Curie-Weiss temperature which is closely related to the interaction between nearest neighbor magnetic ions, and C is called Curie constant which is related to the magnetic moment of each ion.

When $k_B T$ is lower than the interaction energy of two spins, the magnetic properties become complicated. Basically, spins tend to order parallel or antiparallel depending on the nature of the interaction. But whether the system goes to a final ordered state or not is circumstantial. The complication comes from the fact that the interaction between spins can be either isotropic or anisotropic. And they behave differently in different spatial dimensions. The Hamiltonian can be generally expressed as

$$H_{\text{ex}} = -2 \sum_{i,j} J_{ij} (a_x S_{ix} S_{jx} + a_y S_{iy} S_{jy} + a_z S_{iz} S_{jz}) \quad (\text{I.3})$$

where J_{ij} is the exchange interaction between spins at sites i and j , and (a_x, a_y, a_z) characterize the anisotropy. One can classify them into three categories: the Ising system ($a_z=1, a_x=a_y=0$), the X-Y system²³ ($a_z=0, a_x=a_y=1$) and isotropic Heisenberg system¹⁵ ($a_x=a_y=a_z=1$). Their behaviors have been studied theoretically and are summarized in table I.1.

As one can see, the highly anisotropic Ising system will order in two and three dimensions but not in one dimension. Isotropic systems only order in three dimension. The classical X-Y system is quite unique, it orders in three dimension and does not in one dimension. In

	1-D	2-D	3-D
Ising system	No	Yes	Yes
X-Y system	No	No, χ has a peak*	Yes
Heisenberg system	No	No	Yes

Table I.1 Magnetic ordering for different systems in different spatial dimensions. (*) for an antiferromagnetic system

two dimension, there is no long range correlation between spins at finite temperature. However, the susceptibility still show a peak at certain finite temperatures although the spins are not ordered.²³

The main reason that the exchange interaction becomes anisotropic can be traced to the effect of spin-orbit coupling which results in not only an anisotropic paramagnetic Hamiltonian (the g factor is anisotropic) for individual ions but also an anisotropic exchange interaction between magnetic ions at different lattice sites.²⁴ Despite the fact that the orbital angular momentum is quenched by the crystal field and exchange interaction tends to be isotropic in most solids such as 3d ionic oxides, the ground state and excited states are mixed through the spin-orbit interaction yielding an anisotropic g factor. Also the spin-orbit coupling affects the exchange interaction between two spins at two different lattice sites if the local symmetry for these two ions are different.^{25,26}

I.3 The scope of the thesis

The purpose of the work associated with magnetic clay intercalation compounds is twofold. First we would like to study the magnetic properties such as susceptibility, paramagnetic g factors, exchange interaction, and magnetic ordering for different ions with different spins in a similar environment. It will be facilitated by the ease of inserting of different transition metal ions into clay silicates. Secondly, it is important to study the effect of water molecules on the magnetic properties. Accordingly, we present in Chapter III the most recent experimental results of the dc magnetic susceptibility of a

specific clay, vermiculite, with four 3d transition ion (namely Mn^{2+} , Co^{2+} , Ni^{2+} , and Cu^{2+}) as intercalants. The crystal field and magnetic phase transition in these compounds under different hydration conditions are also discussed in the chapter IV.

Since clay silicates are such rigid layered materials, the intercalants prop apart the host layers which introduces a significant amount of free space in the gallery. Thus these microporous system are quite useful in catalysis. Furthermore one can intercalate two or more different cations into the gallery. This makes these systems appealing arenas in which to study physical phenomena such as percolation. Thus, we have carried out a study of mass absorption and dynamical motions of guest atoms in a ternary intercalated system $A_{1-x}B_x-Y$ (where A and B present different intercalants, and Y is the host). The particular system we have chosen is $[Co^{3+}(en)_3]_{1-x}[Cr^{3+}(en)_3]_x$ -Fluorohectorite (here en stands for ethylenediamine). In Chapter V, the most recent results related to the absorption and diffusion of inert gases such as Helium and Argon in this system have been discussed.

Chapter II

Structures of vermiculite and fluorohectorite

Clay minerals include a vast number of different natural layered alumino-silicates.²⁷ They all contain basic building elements of MO_4 tetrahedra and $M'O_6$ octahedra, where M is Si^{4+} and sometimes Al^{3+} or Fe^{3+} and M' is a metal ion such as Mg^{2+} , Li^+ , Al^{3+} , or Fe^{3+} . It is also true that in some clays certain oxygen atoms in the octahedra are replaced by hydroxyl groups such as OH^- or F^- . These elements form infinite tetrahedral and octahedral sheets shown in figure II.1. These sheets are linked together through common oxygen planes to form layers. All clay minerals are composed of layers of these sheets and they are divided into two basic types based on the numbers of sheets in one layer. Some of them contain layers which have two tetrahedral sheets and one octahedral sheet. The octahedral sheet is sandwiched by the tetrahedral sheets. This type of clay is called 2:1 layered silicate. There is another type of silicate in which each layer consists of one tetrahedral sheet and one octahedral sheet. This type of clays is called a 1:1 layered silicate.

The specific layered host material we have used for magnetic studies here is a natural vermiculite (originally from Llano, Texas) which is a typical 2:1 layered silicates (figure II.1).²⁷ Its layers are formed from a sheet of edge connected octahedra which is bounded to two sheets of corner connected tetrahedra. The positive ions in the center of octahedra are mostly divalent ions such as Mg^{2+} . This is called a trioctahedral 2:1 layered silicate in contrast to dioctahedral 2:1 silicates in which the positive ions in the octahedra are mostly

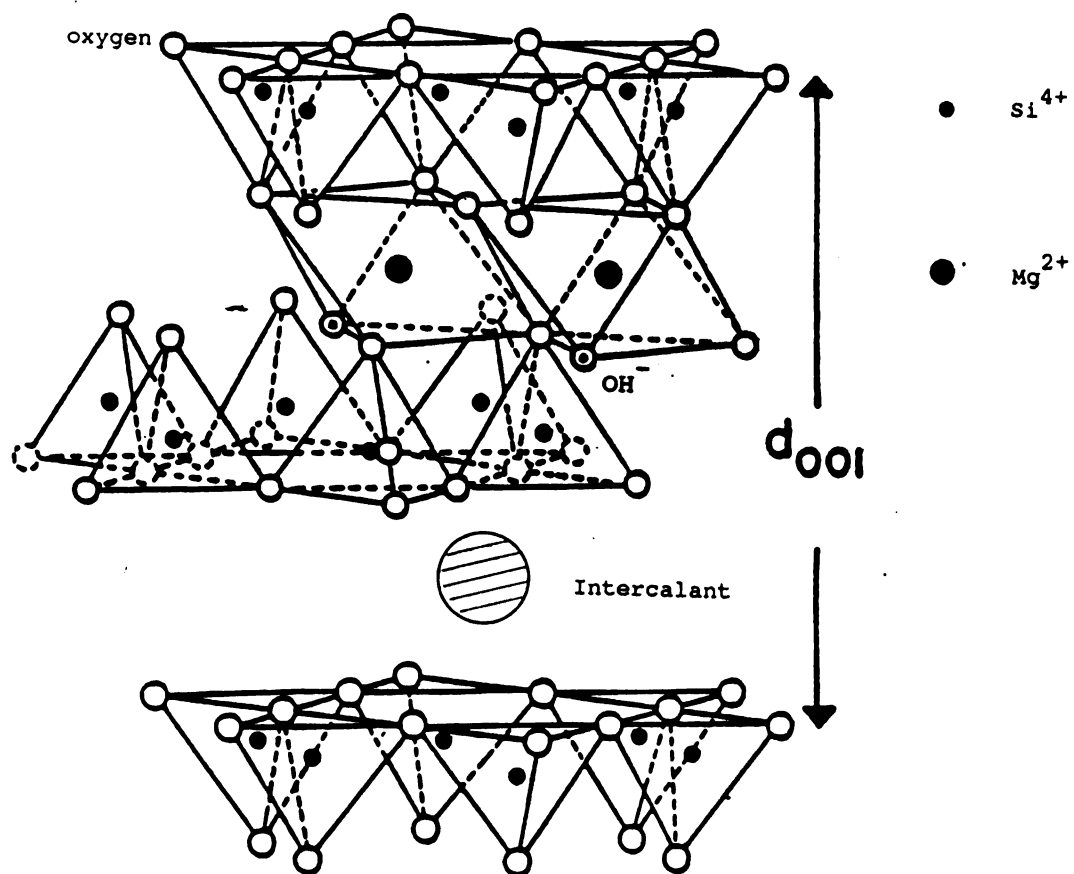


Fig. II.1 Schematic view of a 2:1 layered silicate. The c-axis basal spacing d_{00l} is normally 14.5 Angstrom for hydrated vermiculite.

trivalent ions such as Al^{3+} . The oxygen atoms which are between tetrahedral and octahedral sheets and not shared by both sheets are alternated by hydroxyl groups such as OH^- . For an ideal situation when all ions in tetrahedra are Si^{4+} and all ions in octahedra are divalent (Mg^{2+}), charge neutrality is satisfied within the clay layers. This is a special kind of clay called talc in which there are no charged particles in the intralamellar gallery spaces. Talc is rather uninteresting because one can not insert ions into the gallery. For vermiculite, however, some portion of Si^{4+} ions in the tetrahedra are randomly replaced by trivalent ions such as Al^{3+} . This results in a fixed unbalanced negative charges in the host layers. These residual charges depend on the concentration of Al^{3+} and normally have a magnitude of $1.2e^-$ to $2.2e^-$ per unit formula of vermiculite. It is compensated by the positive cations in the gallery spaces. As mentioned in the overview, these cations can be replaced by other ions by the process of ion exchange.

The basal oxygen atoms from the tetrahedral sheet form a so-called Kagome lattice (Figure II.2) in which the distance between two adjacent hexagons is about 5.28 Å. Each triangle represents the bottom surface of the tetrahedra. Normally a rectangular unit cell (also shown in figure II.2) obtains and it yields a stoichiometry $\text{Si}_{8-x}\text{Al}_x\text{Mg}_6\text{O}_{20}(\text{OH})_4 \cdot \mu\text{M}$ (where M is the exchangeable ions in the gallery, x is normally close to 2). The number of intercalants per unit cell, μ , depends on x and its charge. Each basal oxygen atom has sp^2 type hybridization, resulting in three orbits of which two point to Si^{4+} ions in tetrahedra to form chemical bonds and one points out of the layer. These orbits are doubly occupied. There is a less perturbed p

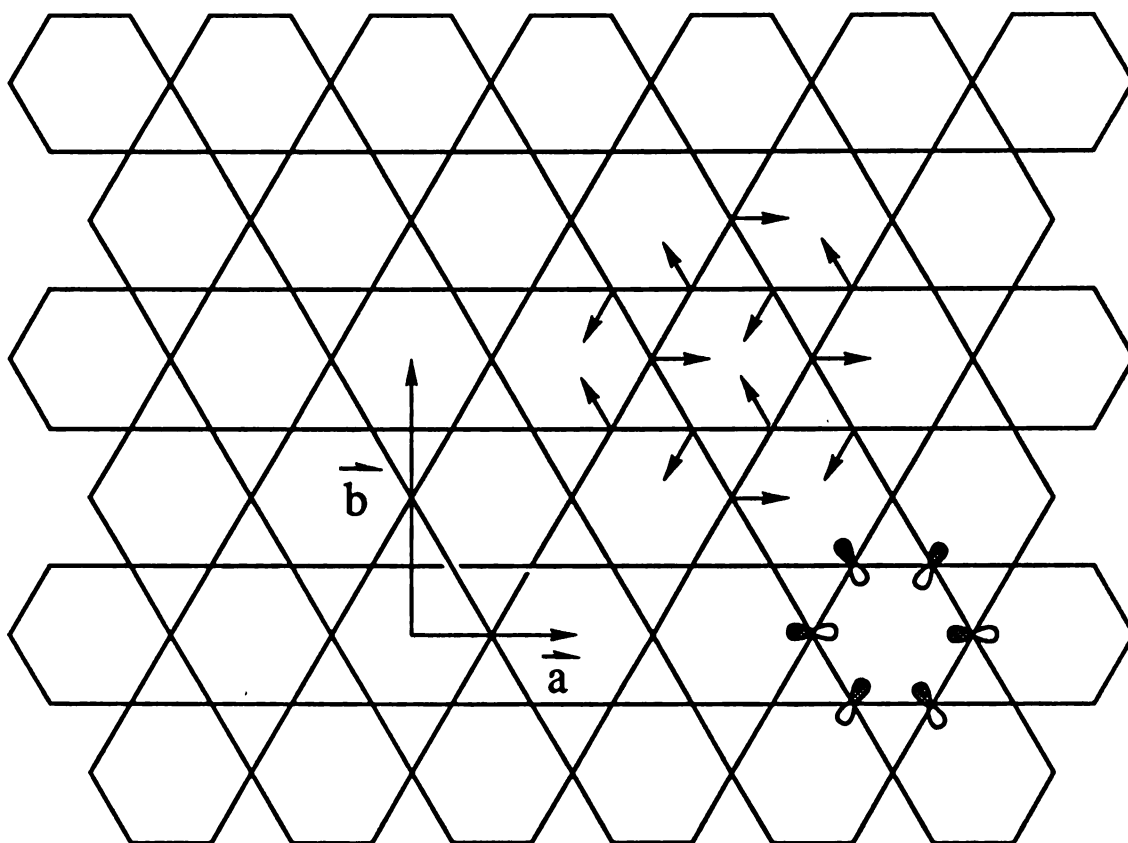


Figure II.2 Schematic view of the Kagome lattice formed by the basal oxygen atoms (located at corners of each equal lateral triangle). Arrows indicate the directions of in plane rotation. The in plane p orbit is also shown for some sites.

orbital for each oxygen lying in the plane and pointing to the center of two adjacent hexagons(see figure II.2).

Another important structural characteristics of vermiculite is the inplane distortion.²⁸ The oxygen-oxygen distances in these tetrahedra and octahedra are not identical. This mismatch in the common oxygen plane between tetrahedral and octahedral sheets causes clockwise and counter-clockwise rotations of adjacent tetrahedra within the tetrahedral sheet (directions are shown by arrows in figure II.2). This effect is common in other clays.²⁷ The tilting angle depends on the mismatch of the distance and the cations in the gallery. In our case, it is about 5 degrees. This distortion lowers the symmetry and changes the strength of local crystal field.

When water molecules are present in the interlamellar spaces, they are bonded to basal oxygen atoms and form two layers sandwiching the exchangeable cations. The C-axis basal spacing ranges from 14.5 Å to 9.02 Å depending on the temperature and water vapor pressure (see ref. 27, p110). The dependence of the c-axis basal spacing on water content in vermiculite has been studied extensively²⁹. Figure II.3 shows the stacking sequence between host layers in vermiculite with interlayer cations and water molecules in the gallery. Cations and water molecules occupy only a portion of the sites depending on the charge density of the host layer. At ambient conditions, there is a random $\frac{1}{3}$ shift between layers to accommodate the water molecules in the gallery. This effect is called "Staggering" which is a common phenomenon in all layered silicates. The $\frac{1}{3}$ shift within a host layer is the natural consequence of putting two tetrahedral sheets together with an octahedral sheet in the middle.

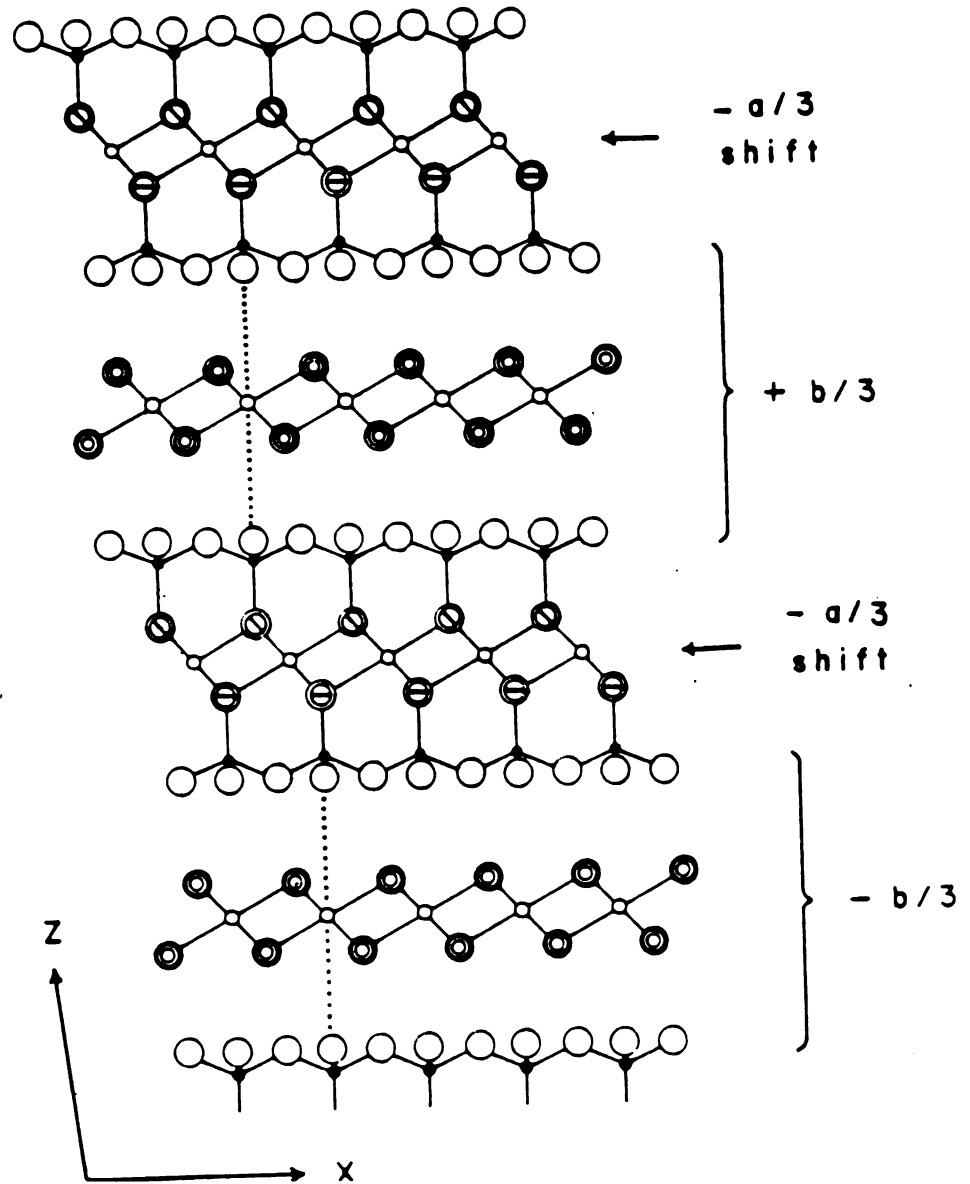


Fig. II.3 The stacking sequence in vermiculite.

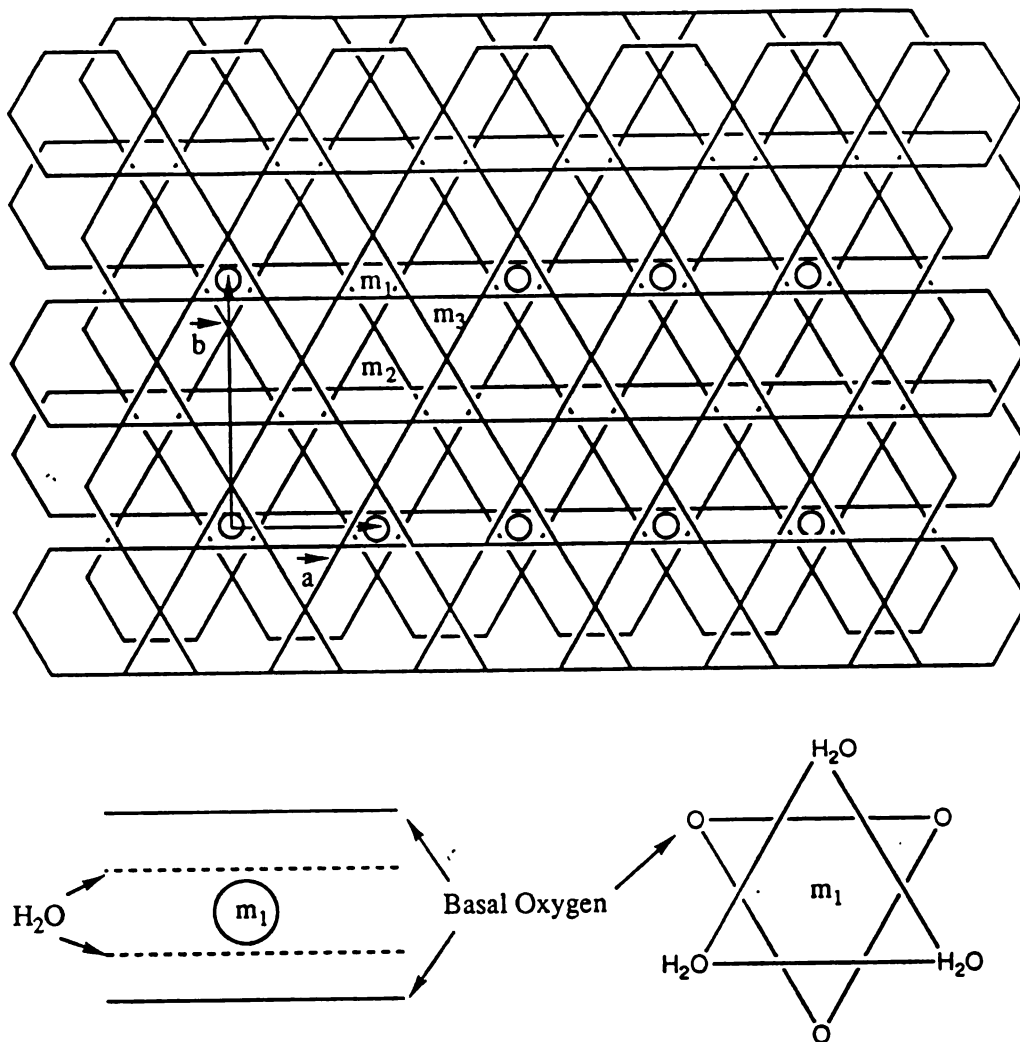


Fig. II.4 The staggering between two basal oxygen planes shifted relatively by $b/3$. The three possible gallery cation sites (m_1 , m_2 , m_3) are shown. Open circles occupy a rectangular lattice. The relative positions between basal oxygens and interlayer water molecules at site m_1 are also shown. An intercalant sits on the top of three water molecules and is covered by the other three water molecules (not shown).

There are three different gallery sites for exchangeable cations for b/3 staggering (illustrated in Figure II.4). It has been found that cations such as Mg^{2+} and Ni^{2+} are likely to be retained in the tetrahedral cavity sites (m_1) (see figure II.4, relative positions between water molecules and basal oxygen plane are also shown.). And for Na^+ and Ca^{2+} , the cation positions can be all three sites (m_1, m_2 and m_3). More detailed discussion about this topic will be given in Chapter III.

Another important aspect is that in the vermiculite with charge density of $2e^-$ per unit cell, the lattice structure formed by divalent intercalants is rectangular as shown in fig. II.4. In reality, the lattice arrangement of divalent cations can be thought of as a rectangular network with site occupancy disorder.

Fluorohectorite (FHT) is also a trioctahedral 2:1 layered silicate. Its structure is basically the same as vermiculite (Figure II.1). There are three differences between them. First, in FHT the ion substitution happens in the octahedral sheet instead of in the tetrahedral sheets. Secondly, FHT has a charge density of about $1.6e^-$ per unit cell formula which is less than in vermiculite. Thirdly, the oxygens in the common plane between a tetrahedral sheet and an octahedral sheet and not shared by both sheets are F^- instead of $(OH)^-$. The interlayer cations can also be replaced by other intercalants as in vermiculite.

Chapter III

The dc magnetic susceptibility of vermiculite intercalation compounds with 3d metal ions as intercalants

III.1 Introduction

The magnetic properties of lower dimensional systems including layered metallic superlattices and layered magnetic insulators are particularly interesting relative to the behavior of the bulk hosts. An example can be La_2CuO_4 which has been attracting considerable attention recently because of its relation to high- T_c materials. Layered silicates such as vermiculite provide natural layered structures on which one can carry out the same kinds of studies as well. The advantages of the latter have been stated in the overview (Chapter I).

Although there are recent studies of the magnetic properties of vermiculite (ver) with several 3d metal ions and 4f metal ions as intercalants³⁰ (namely Mn^{2+} , Co^{2+} , Ni^{2+} , Cu^{2+} , Dy^{3+} , and Er^{3+}) cointercalated with water, there are still significant questions remaining. First, Ni^{2+} -ver shows a Curie-Weiss behavior in the high temperature region and the Curie-Weiss temperature is positive (≈ 10 K) indicating that the intraplanar exchange interaction between Ni^{2+} ions is probably ferromagnetic. But the magnetic susceptibility does not diverge for temperatures down to 4.3K indicating there is no phase transition corresponding to ferromagnetic ordering for temperatures from 4.3K up to 300K. Secondly, other compounds such as Co^{2+} -ver, Mn^{2+} -ver and Cu^{2+} -ver exhibit negative Curie-Weiss temperatures suggesting an antiferromagnetic interaction between these cations. But again previous

authors³⁰ have failed to observe any phase transition corresponding to antiferromagnetic ordering. In other words, all these systems behave paramagnetically at temperatures near 4.3K.

In order to clarify the behavior of these interesting compounds we have conducted more careful studies on the magnetic susceptibility for samples with higher intercalant concentration and under different hydration conditions. Specific compounds studied here are Mn²⁺-ver, Co²⁺-ver, Ni²⁺-ver and Cu²⁺-ver in which the magnetic intercalants are all divalent and their spins are 5/2, 3/2, 1 and 1/2, respectively. As one should expect, there are two major factors which influence the magnetic properties dramatically. First is the distance between two nearest neighbor intercalants which depends on the cation concentration. Due to the fact that the magnetic exchange interaction will decay exponentially as the distance between intercalants increases, we should have a cation concentration as high as possible. Thus, we have developed a new method to synthesize powder samples with higher intercalant concentration than previously obtained. The second factor is the presence of water molecules in the gallery spaces which will affect the magnetic properties dramatically as well. Therefore, we have conducted more careful studies of the dc magnetic susceptibility under three different conditions: hydrated, dehydrated and rehydrated.

III.2 Experiments

III.2.1 Sample preparation

The original sample starting material for our studies is trioctahedral Mg^{2+} -vermiculite (Llano, Texas) which has been ground into very fine powders with particle size of a few micrometers. In order to purify the gallery, the exchange sites are saturated with Mg^{2+} ions to replace other impurities ions such as Ca^{2+} or Na^{1+} in the gallery. Chemical analysis by using Induced Coupled Plasma (ICP) method shows the following unit cell stoichiometry



which is abbreviated as $\text{X} \cdot \text{M}_u \cdot (\text{H}_2\text{O})_\mu$, where X stands for the host layer matrix and M stands for the exchangeable metal ions in the gallery. Here Si^{4+} and Al^{3+} ions are randomly located at the centers of the tetrahedra. There are some Al^{3+} , Fe^{2+} and Ti^{2+} ions in the octahedral layer as impurities which can not be replaced.

To ensure complete exchange of gallery Mg^{2+} ions with the desired transition metal ions we have carried out a two-step ion exchange procedure. In the first step, all the Mg^{2+} ions in the gallery have been exchanged with alkyl-ammonium ions such as $(\text{CH}_3)_3\text{NH}^+$ ions, by the reaction of the powdered parent compound with excess $[(\text{CH}_3)_3\text{NH}]\text{Cl}$. The next procedure is to replace $(\text{CH}_3)_3\text{NH}^+$ ions by the desired magnetic ions. This is done by putting intermediate product into suspensions with the desired ions. These two ion-exchange procedures are complete and can be confirmed using their X-ray diffraction patterns (Figure III.1). Due to the different sizes of Mg^{2+} , $(\text{CH}_3)_3\text{NH}^{1+}$ and 3d metal ions, the c-axis basal spacings for these compounds are quite different (the basal spacings are 14.5Å, 12.8Å and 14.5Å for Mg^{2+} -ver, $(\text{CH}_3)_3\text{NH}^{1+}$ -

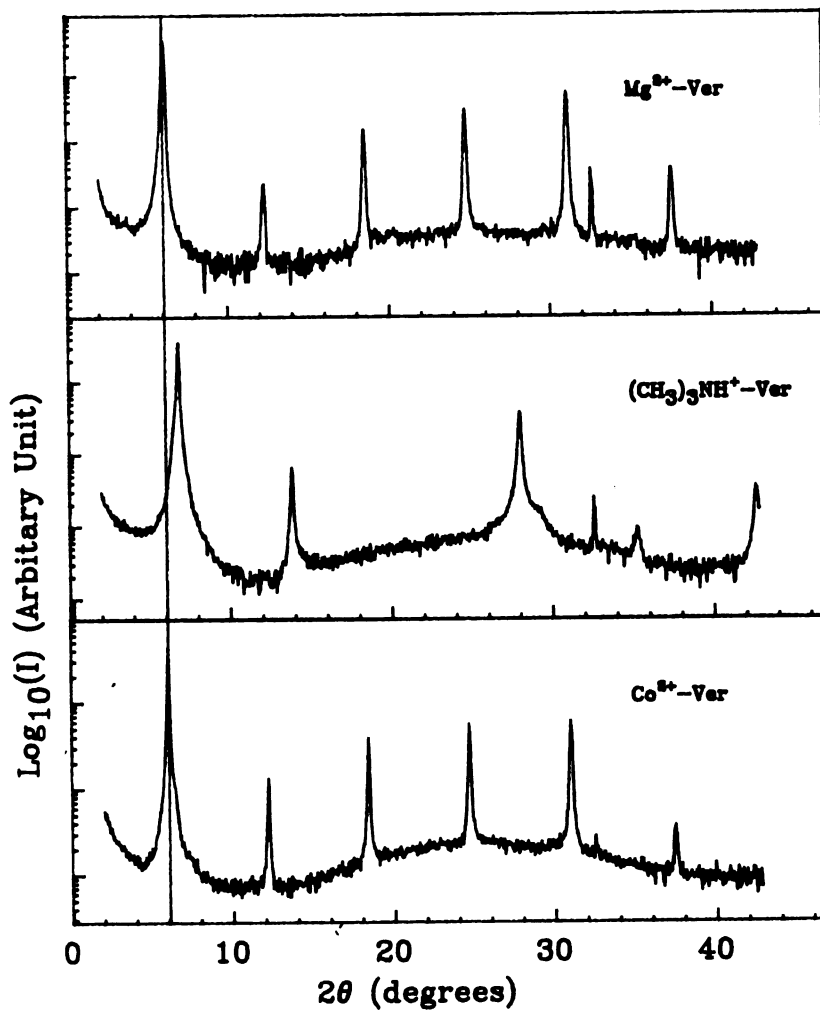


Fig. III.1 The X-ray diffraction pattern for $\text{Mg}^{2+}\text{-ver}$, $(\text{CH}_3)_3\text{NH}^+\text{-ver}$, and $\text{Co}^{2+}\text{-ver}$ at ambient conditions. The vertical line is the guide to eye. These pattern were obtained at room temperature using $\text{Cu}(K_\alpha)$ radiation.

ver and M-ver, respectively. Here M stands for the desired magnetic ions). By monitoring the c-axis basal spacing from X-ray diffraction spectrum we are able to see the completion of the ion exchange reactions. The purity of the final compounds has been further confirmed by infra-red spectroscopy and by chemical analyses such as ICP.

Four different vermiculite intercalation compounds have been synthesized with different cations such as Mn^{2+} , Co^{2+} , Ni^{2+} and Cu^{2+} ions. At ambient conditions, these compounds contain two layers of water in the gallery spaces surrounding the cations. By heating these compounds to 600 C one can remove water completely.³¹ At that temperature, the host layers undergo dehydroxylation and this process is irreversible. It has been found from thermal gravimetric analysis (TGA) that most of water is removed at temperatures above 150 C (Figure III.2). Therefore, we have annealed our samples at between 170C and 180 C in vacuum for more than 12 hours. Figure III.3 shows the X-ray diffraction spectrum of the hydrated sample at ambient condition and that of a annealed sample. The basal spacing has decreased from 14.5 Å to 10.5 Å. All of our powder samples have been pressed into pellets for easy handling.

III.2.2 DC magnetic susceptibility measurement and techniques for data analysis

The DC magnetic susceptibility ($\chi(T)$) of these magnetic intercalation compounds has been measured from temperature of 2 K to 300 K by using a Superconducting Quantum Interference Device (SQUID) magnetometer from Quantum Design. The applied magnetic field H was 100

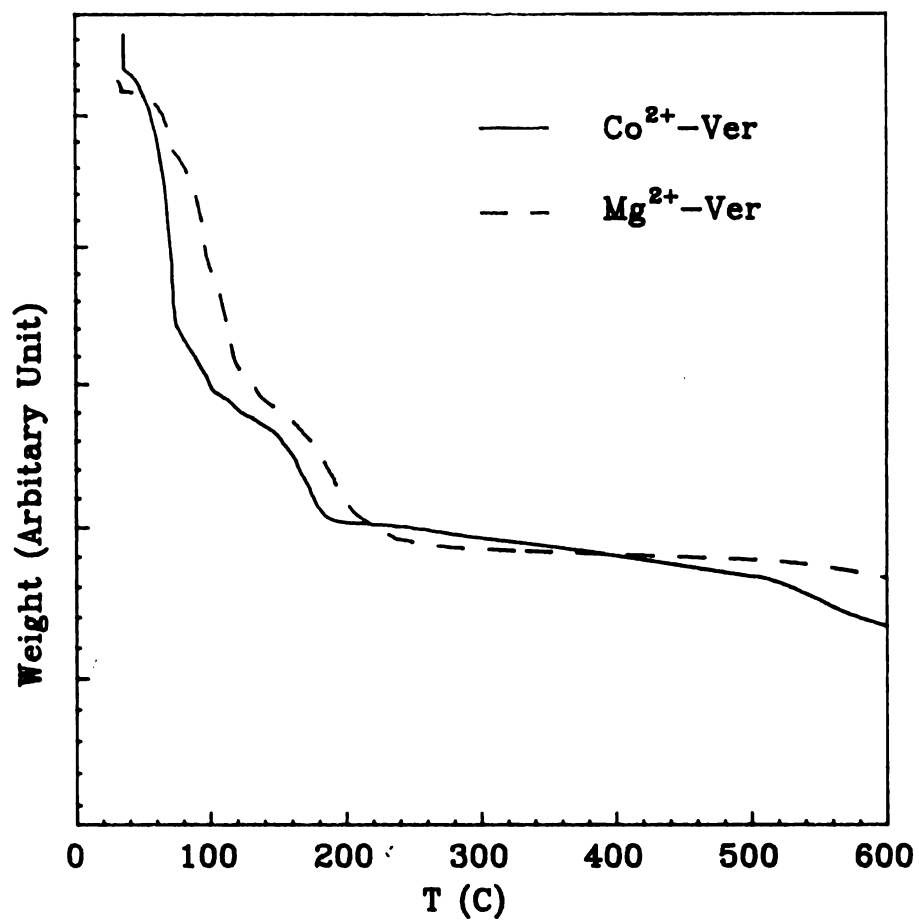


Fig. III.2 The weight loss of $\text{Co}^{2+}\text{-ver}$ and $\text{Mg}^{2+}\text{-ver}$ versus temperature measured by the TGA method

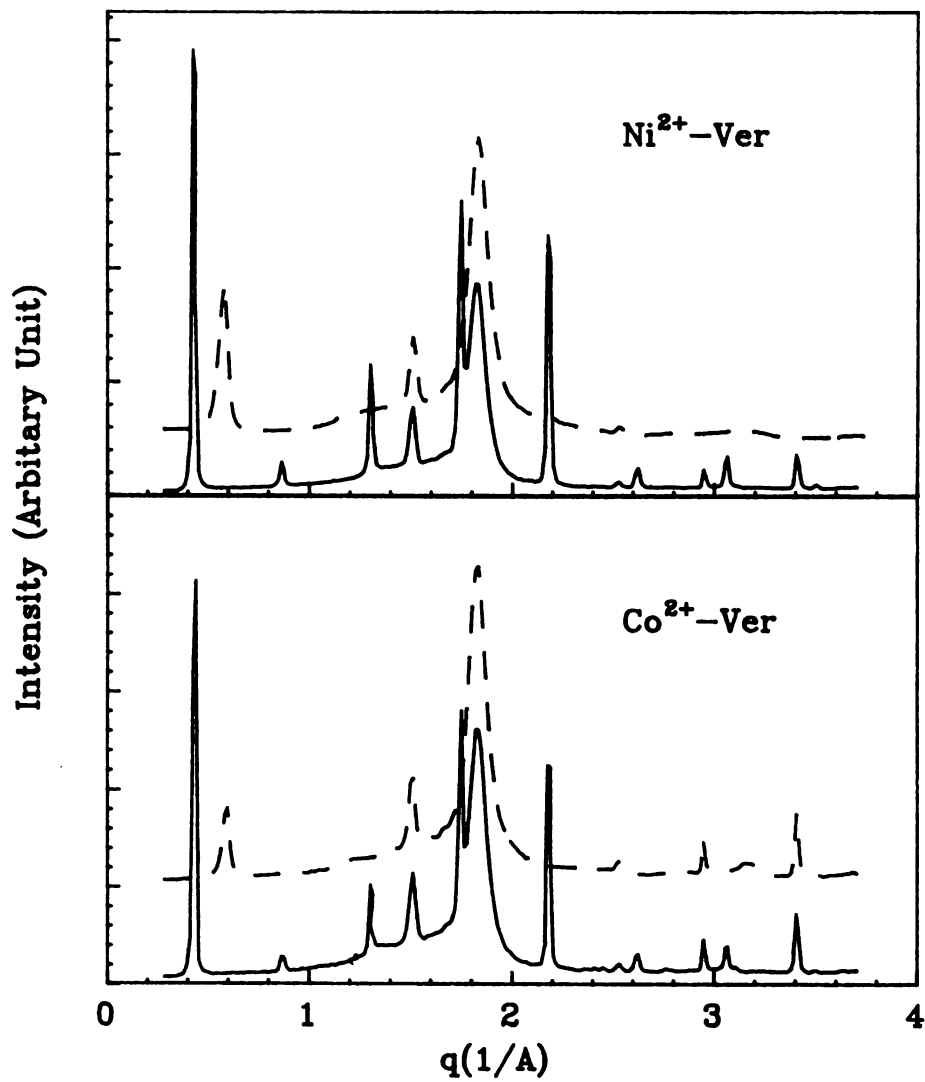


Fig. III.3 The X-ray diffraction patterns for Co^{2+} -ver and Ni^{2+} -ver before annealing (solid lines) and after annealing (dashed lines). The c-axis basal spacing are about 14.5 Å and 10.5 Å for both compounds before and after annealing, respectively. The source radiation is Cu K_α .

Gauss. And the error bar in the susceptibility measurement is extremely small (about 1/1000 of the magnitude measured).

Since there are some residual magnetic impurities such as Fe^{2+} ions in the octahedral layers and they contribute to the total magnetic moment, we have first measured the susceptibility of the parent compound Mg^{2+} -ver to find out the contribution from these impurities. Figure III.4 shows the susceptibility χ of Mg^{2+} -ver versus temperature. As one expects, this system behaves paramagnetically indicating that the impurities from the host layers are isolated and do not interact with each other. By fitting the data with the Curie formula³²

$$\chi = \chi_0 + \frac{C_g}{T} \quad (\text{III.1})$$

where χ_0 is the the contribution from the full shell electrons and C_g is the Curie constant. We have found χ_0 to be -0.91×10^{-7} emu/gram which is obviously the diamagnetic contribution from the full shell electrons. The next term is from the magnetic impurity from the host layers. The Curie constant C_g of Mg^{2+} -ver has been found to be about 1.33×10^{-4} emu K /gram. The Curie constant is related to other parameters as follows³²

$$C_g = \frac{1}{3} \frac{N_A}{M} \frac{\mu_B^2 P_{\text{eff}}^2}{k_B} \quad (\text{III.2})$$

where N_A is Avogadro's constant, M the molar mass of the unit-cell stoichiometry $X.M(\text{H}_2\text{O})_x$, μ_B is the Bohr magneton, k_B is the Boltzmann constant, and P_{eff} is the effective magnetic moment defined as³²

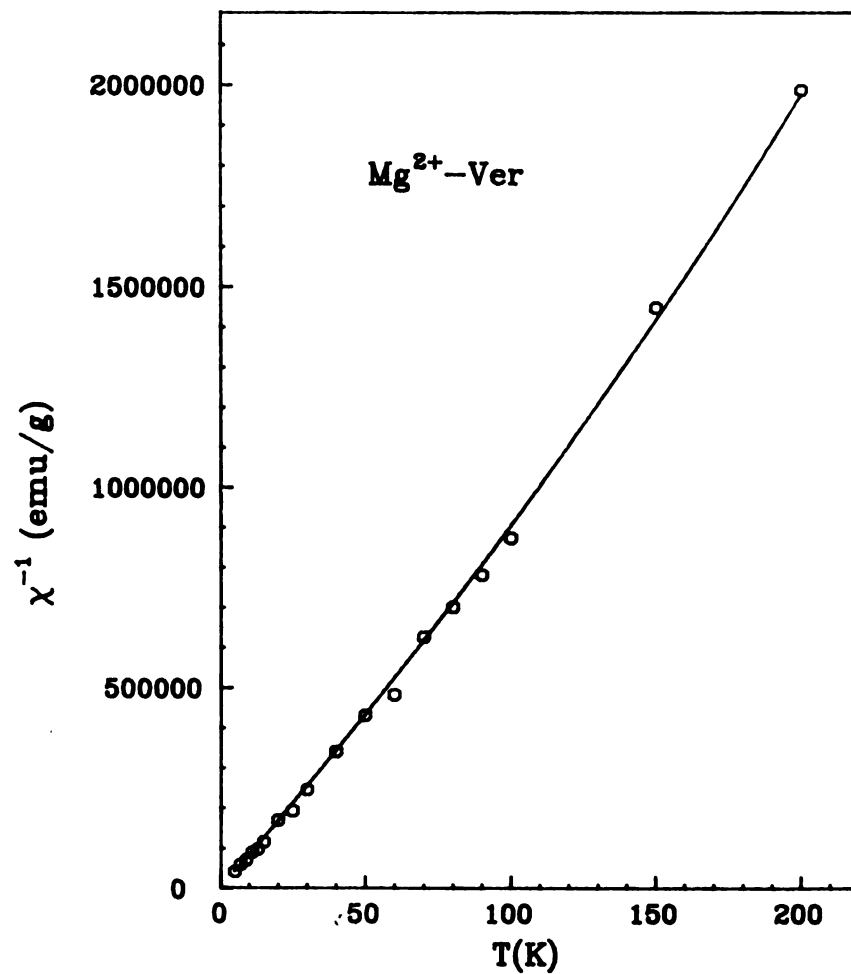


Fig. III.4 The inverse susceptibility χ^{-1} of hydrated Mg^{2+} -ver versus temperature. The open circles are the data points and the solid line is the least square fit to the Curie law.

$$P_{\text{eff}} = g(JLS)\sqrt{J(J+1)} \quad (\text{III.3}).$$

From C_g obtained above and the concentration of Fe^{2+} ions in Mg^{2+} -ver (obtained from the unit cell formula) , we have obtained the effective magnetic moment to be $5.21\mu_B$. This is close to the value found in the literature for Fe^{2+} ions³² ($5.4 \mu_B$). Since the impurities are very dilute and located in the octahedral layer, we ignore any interaction between them and the magnetic cations in the gallery and subtract out the paramagnetic signal from them by using the parameters measured from Mg^{2+} -ver.

We have measured the dc susceptibility for Mn^{2+} -ver, Co^{2+} -ver, Ni^{2+} -ver, and Cu^{2+} -ver under three different conditions: hydrated, dehydrated, and rehydrated. The dehydration procedure has been carried out using the methods described earlier. The dehydrated samples were transferred and sealed in polyethylene bags to prevent hydration. After the measurement had been done for dehydrated samples, they were exposed to air for more than 6 hours in order to regain water into the intralamellar gallery spaces. Their masses have been measured in different hydration stages to monitor how much water has been removed and reabsorbed. The experimental data have been analyzed by least square fitting the higher temperature portions of the susceptibility curve to the Curie-Weiss formula (also see ref.32, p712)

$$\chi = \chi_0 + \frac{C_g}{T - \theta} \quad (\text{III.4}).$$

Therefore, the Curie constants C_g and Curie-Weiss temperatures θ have been obtained for each case. The relations in equations (III.2) and (III.3) are maintained. Thus the effective magnetic moments P_{eff} and the Lande g factors for different ions under different conditions have been also calculated as for Fe^{2+} ions in the Mg^{2+} -ver.

III.3 Results of the DC magnetic susceptibility of vermiculite with magnetic intercalants

III.3.1 Mn^{2+} -ver

The Mn^{2+} ion has electronic structure $3d^5$ and spin $5/2$. Five d electrons occupy all five d orbitals and the total spin moment is $5/2$. Figure III.5 shows the inverse of the magnetic susceptibility, χ , per gram sample versus temperature for a pellet sample under three conditions: hydrated, dehydrated; and rehydrated. The sample lost about 16% of the initial weight after annealing and regained all of the weight back when it has been rehydrated. The impurity signal has been subtracted by using the parameters obtained from Mg^{2+} -ver. As one can see, the inverse of χ for the three different hydration linearly depend on the temperature. This demonstrates that the system is paramagnetic for temperatures down to 2K (which is the lowest temperature limit of the SQUID we use here) regardless of whether water molecules are present in the gallery or not.

By least square fitting to the high temperature portion of χ , We have obtained C_g and θ for various conditions and in addition we have obtained the effective magnetic moments, P_{eff} , and g factors from C_g .

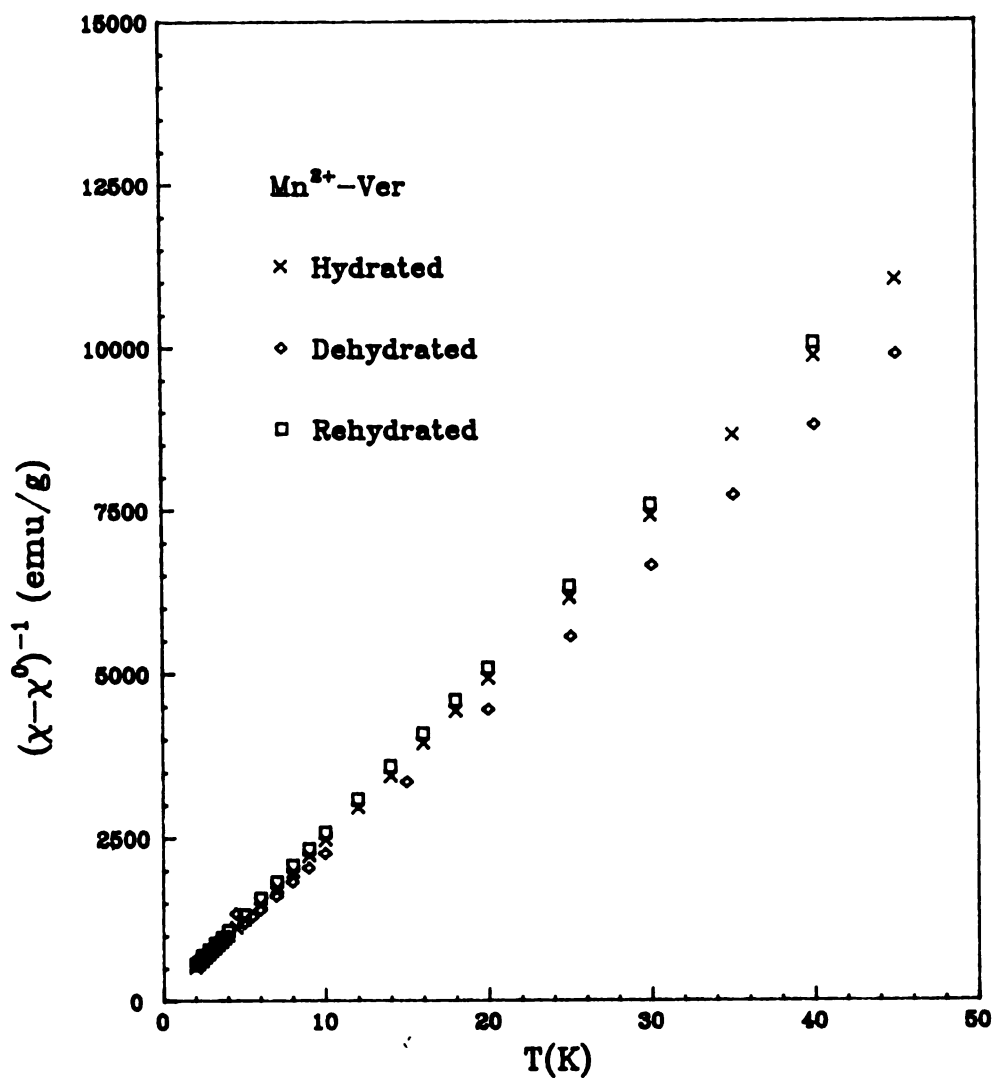


Fig. III.5 The inverse susceptibility $\chi^{-1}(T)$ of Mn^{2+} -ver under different hydration conditions.

	χ^0 (emu/g)	C_g (emuK/g)	θ_c (K)	at low temp.	T_c (K)
Hydrated	1.59×10^{-5}	4.40×10^{-3}	0.08	Paramag.	None
Dehydrated	1.86×10^{-5}	5.23×10^{-3}	-0.80	Paramag..	None
Rehydrated	1.61×10^{-5}	4.25×10^{-3}	-0.10	Paramag.	None

(Continued)	P_{eff} (μB)	g value
Hydrated	5.81	1.95
Dehydrated	5.87	1.98
Rehydrated	5.71	1.93

Table III.1 Parameters for Mn^{2+} -Ver from a least square fit to the Curie-Weiss formula.

These physical quantities are summarized in Table III.1. As one can see, the Curie temperature θ is close to zero and is scattered for the hydrated compounds. The most important feature of table III.2 is that the effective magnetic moments for different hydration conditions are essentially the same. This implies that the magnetic properties of a Mn^{2+} ion in vermiculite are apparently not affected by the change of its hydration environment.

III.3.2 Co^{2+} -ver

Co^{2+} ions have the electronic structure of $3d^7$ and spin $3/2$. The DC susceptibility χ for different hydration states of this vermiculite is shown in figure III.6. So is the inverse of the susceptibility χ^{-1} . We can see a Curie-Weiss behavior for the higher temperature portions for all cases. In lower temperature region, both hydrated and rehydrated compounds are paramagnetic in agreement with other authors' results for hydrated samples³⁰.

In the absence of H_2O molecules, the susceptibility χ shows a peak at around 5K while χ decreases with temperature. By fitting the higher temperature portions of $\chi(T)$, we have obtained C_g and θ for the different hydration conditions and calculated the effective magnetic moment P_{eff} and g factors. They are listed in Table III.2. The Curie-Weiss θ values are negative indicating that the nearest neighbor interaction is antiferromagnetic. Another feature one should notice is that the Curie temperature θ clearly depends on the hydration conditions of the sample. When water is present in the gallery, θ shifts from about -7K to about -2K indicating that the interaction is weakened. The

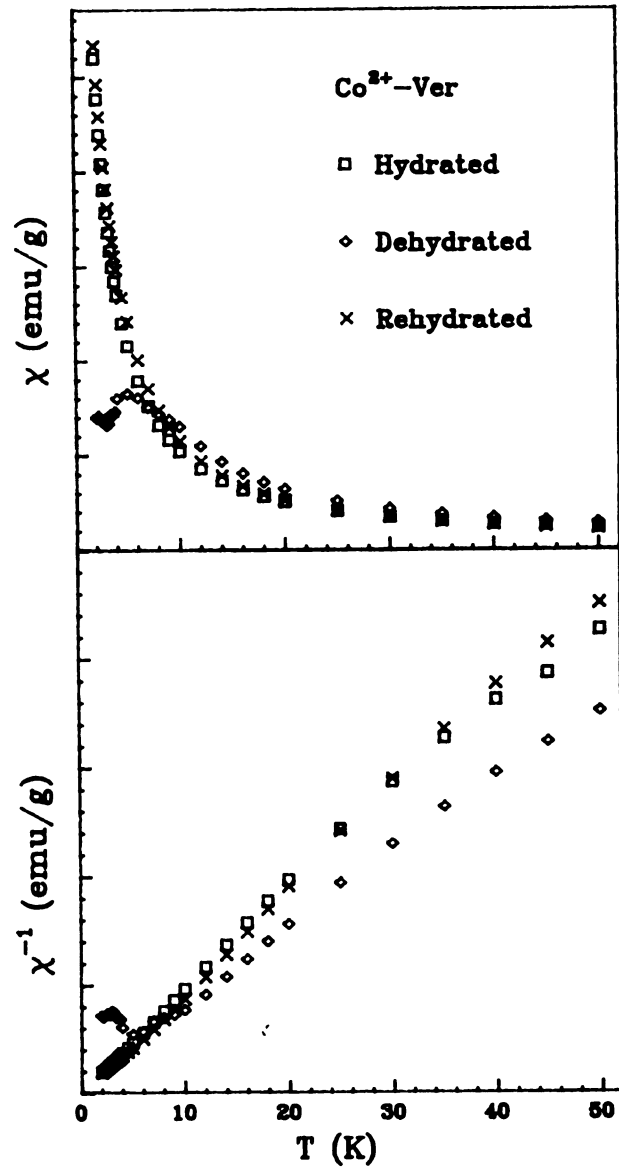


Fig. III.6 The dc magnetic susceptibility $\chi(T)$ and its inverse $\chi^{-1}(T)$ of Co^{2+} -ver under different hydration conditions.

	χ^0 (emu/g)	C_g (emuK/g)	θ_c (K)	at low temp.	T_C (K)
Hydrated	7.135×10^{-6}	2.38×10^{-3}	-1.98	Paramag.	None
Dehydrated	3.424×10^{-6}	3.49×10^{-3}	-7.07	Antiferro.	~5K
Rehydrated	5.722×10^{-6}	2.37×10^{-3}	-1.43	Paramag.	None

(Continued)	$P_{\text{eff}} (\mu_B)$	g value
Hydrated	4.28	2.21
Dehydrated	4.80	2.48
Rehydrated	4.28	2.21

Table III.2 Parameters for Co^{2+} -Ver obtained from a least square fit to the Curie-Weiss formula.

effective moment increases from $4.28 \mu_B$ to $4.8 \mu_B$ as water is removed from the gallery. P_{eff} for Co^{2+} in the dry sample is consistent with the literature value (see ref.32, p658).

III.3.3 Ni^{2+} -ver

A Ni^{2+} ion has 8 electrons in the 3d shell and has spin 1. The susceptibility χ for a hydrated Ni^{2+} -ver is shown in Figure III.7. It also shows a Curie-Weiss behavior for higher temperatures for different hydration conditions. Figure III.7 also shows the lower temperature portions of the inverse susceptibility χ^{-1} . The curves corresponding to hydrated and rehydrated samples behave in the same way as temperature is reduced to 2K in agreement with previous work³⁰, indicating that hydrated/rehydrated compounds behave paramagnetically. The inverse of the susceptibility χ^{-1} for dehydrated case levels off for $T < 4\text{K}$. Although the signal fluctuates, a dramatic difference between the dehydrated case and hydrated/rehydrated cases still can be seen. We have fit the higher temperature portions of χ for all cases and all parameters are summarized in table III.3.

The Curie temperature θ is negative for the dehydrated compound which indicates antiferromagnetic exchange interaction between Ni^{2+} ions. And it becomes positive as water is admitted in the gallery. This phenomenon demonstrates a dramatic change of the exchange interaction from antiferromagnetic to ferromagnetic. The effective moment also increases when water is taken out of the gallery.

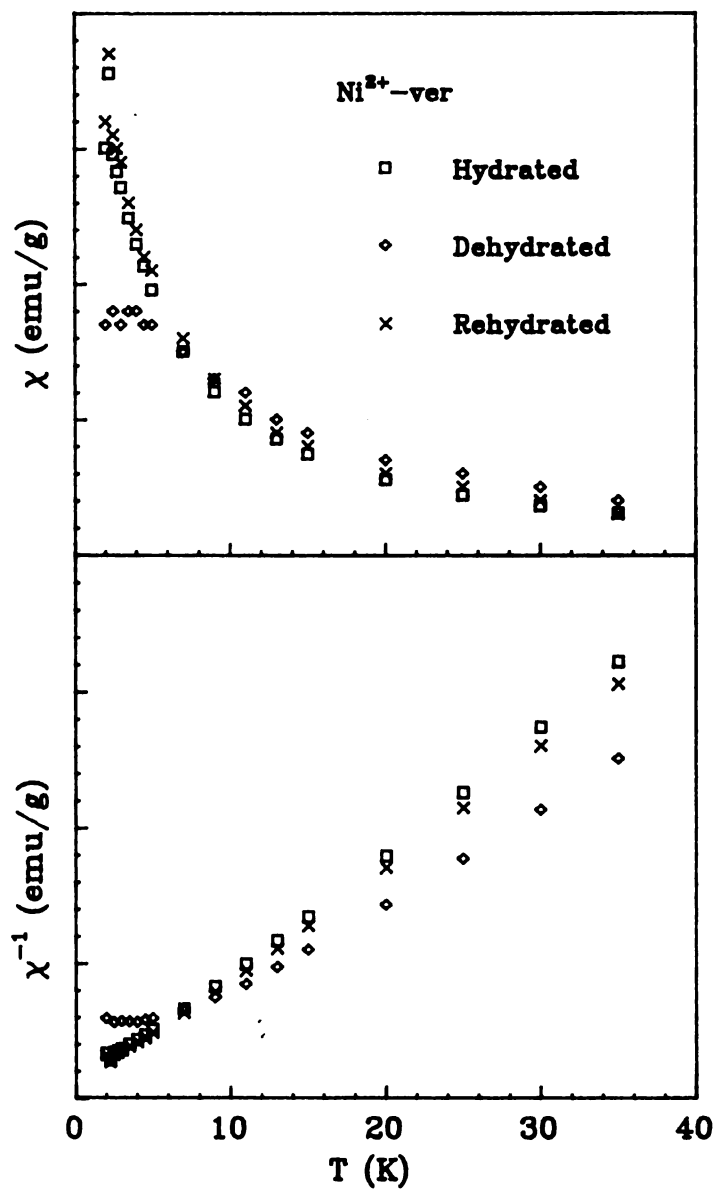


Fig. III.7 The DC magnetic susceptibility $\chi(T)$ and its inverse $\chi^{-1}(T)$ of Ni^{2+} -ver under different hydration conditions.

	χ^0 (emu/g)	C_g (emuK/g)	θ_c (K)	at low Temp.	T_C (K)
Hydrated	-6.26×10^{-7}	1.22×10^{-3}	4.13	Paramag.	None
Dehydrated	-5.20×10^{-7}	1.59×10^{-3}	-0.66	Antiferro.	~ 3K
Rehydrated	1.04×10^{-7}	1.19×10^{-3}	1.66	Paramag.	None

(Continued)	P_{eff} (μ_B)	g value
Hydrated	3.07	2.17
Dehydrated	3.24	2.29
Rehydrated	3.03	2.14

Table III.3 Parameters for Ni^{2+} -Ver obtained from a least square fit to the Curie-Weiss formula.

III.3.4 Cu²⁺-ver

A Cu²⁺ ion has the electronic structure of 3d⁹ and spin 1/2. Since the spin is small, one should expect so-called quantum fluctuation which may quench any magnetic phase transition caused by relatively weak interactions. The dehydrated sample has lost about 16% of its initial weight and regained back this weight after it was exposed in air. Figure III.8 shows the susceptibility χ versus temperature for Cu²⁺-ver under different hydration conditions. All three curves follow a Curie-Weiss law for temperatures down to 2K regardless of whether water is present or not. We have fit the higher temperature portions of χ for different hydration cases and the results are tabulated in table III.4. As can be seen, the effective moment increases from 2.0 μ_B to about 2.15 μ_B when water is removed from the gallery. The Curie temperature is negative for all cases indicating an antiferromagnetic interaction between cations.

III.4 Remarks

In this chapter, we have present the DC magnetic susceptibility data of hydrated and dehydrated vermiculites with four different transition metal ions Mn²⁺, Co²⁺, Ni²⁺, and Cu²⁺ as intercalants. Data have been analyzed by using Curie-Weiss formula. Therefore, the Curie-Weiss temperature θ and Curie constants C_g have been obtained from the least square fitting. Furthermore, the average g factors have been extracted from the Curie constants.

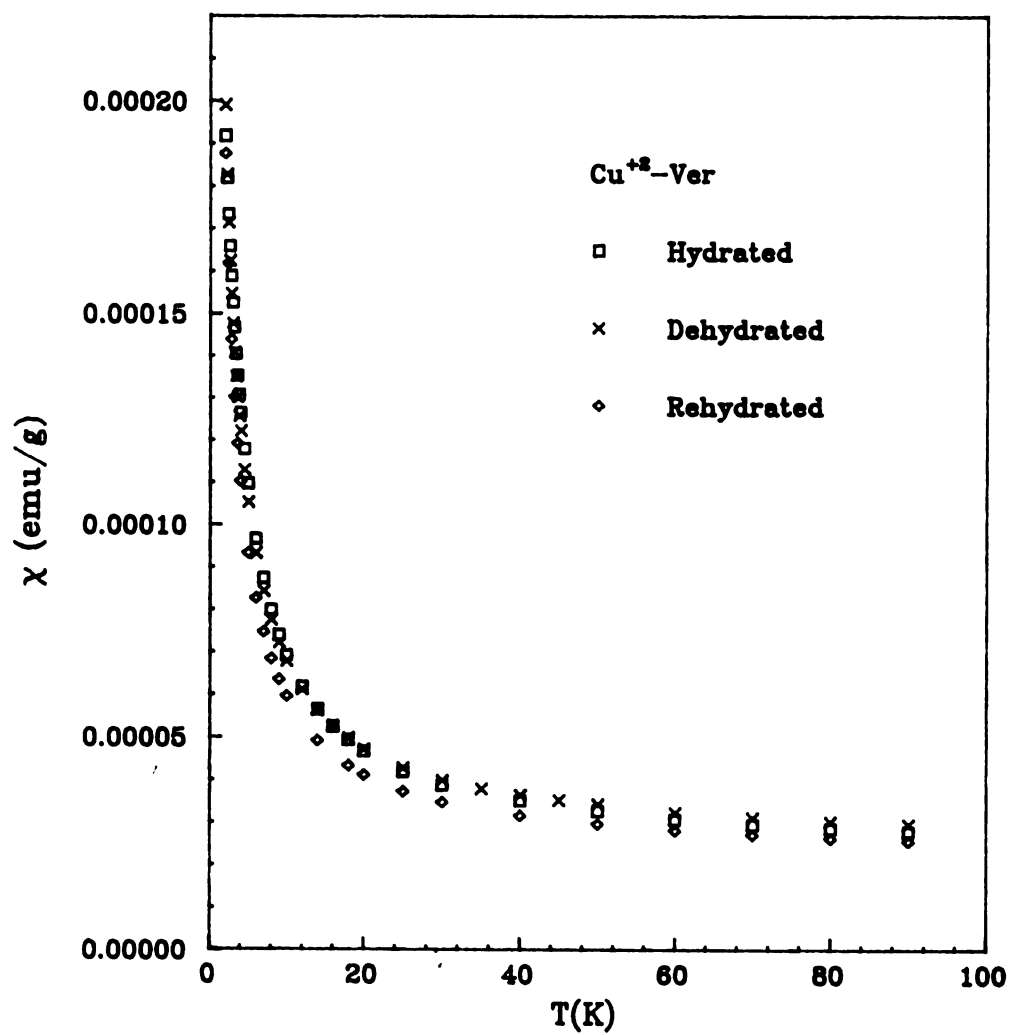


Fig. III.8 The DC magnetic susceptibility $\chi(T)$ of Cu^{2+} -ver under different hydration conditions.

	χ^0 (emu/g)	C_g (emuK/g)	θ_c (K)	at low Temp.	T_C (K)
Hydrated	2.18×10^{-5}	5.22×10^{-4}	-1.16	Paramag.	None
Dehydrated	2.39×10^{-5}	6.97×10^{-4}	-1.16	Paramag..	None
Rehydrated	2.20×10^{-5}	4.97×10^{-4}	-0.77	Paramag.	None

(Continued)	P_{eff} (μ_B)	g factor
Hydrated	2.01	2.32
Dehydrated	2.15	2.48
Rehydrated	1.96	2.26

Table III.4 Parameters for Cu^{2+} -Ver obtained from a least square fit to the Curie-Weiss formula.

Chapter IV

Crystal field, exchange interaction, and phase transition in vermiculite intercalation compounds with 3d metal ions as intercalants

IV.1 Introduction

In chapter III, we have presented the experimental data of the vermiculite intercalation compounds with Mn^{2+} , Co^{2+} , Ni^{2+} , and Cu^{2+} as intercalants. As mentioned in the Overview, the paramagnetic properties of a single ion are manifested in the high temperature portion of the susceptibility. An important quantity is the Lande g factor which is related to the electronic structure of the ion and the crystal field environment. Although the paramagnetic properties of various ions in different crystal fields have been studied by using crystal field theory, there are no such detailed studies on our specific CIC compounds. Therefore we present in this chapter a very detailed investigation of the paramagnetic behaviors of the four ions in hydrated and dehydrated vermiculite. Furthermore, these four compounds exhibit different behaviors when temperature is very low. Thus a discussion on the magnetic exchange interaction and phase transition in these CIC compounds will be also given to understand our experimental results.

IV.2 Lande g factors and anisotropic Hamiltonian

From the effective magnetic moments, we have calculated the Lande g factors for various ions under different conditions by using equation

(III.3). Because our samples are powders, we can only obtain average g values. They are summarized in table IV.1.

As one can see, the g factor for Mn^{2+} ions is very close to 2 for all three cases. This is consistent with the results of many other Mn^{2+} complexes which have been investigated previously.³³ The reason is that a Mn^{2+} ion has electronic structure of d^5 . The ground state of a free Mn^{2+} ion is 6S which has no orbital momentum. In the solid, the ion behaves like a single s electron and exhibits no splitting regardless of the symmetry of the local crystal field. The g factor is always 2 for an orbital singlet since the expectation values for \vec{L} vanishes. Another result is that this system is isotropic because the moment derives from the spin only. Mn^{2+} ions are considered to form a classical Heisenberg system since they have large spin moments ($s=5/2$) and interact with each other isotropically.

The g factor for Co^{2+} ions varies significantly between hydrated/rehydrated states and dehydrated state. When water is present, the g factor is about 10% greater than 2. This indicates that in the ground state of a Co^{2+} ion, the orbital angular moment is quenched but the spin-orbit coupling still contributes to the magnetic moment by mixing in higher excited states. When water is taken out of the gallery, there is about an additional 13.0% increase in the g factor. There are two factors which will affect g : the symmetry and the strength of the crystal field. A change of Symmetry will result in different energy spectrum. A change of the crystal field strength can result in less or more mixing of energy levels through L-S coupling.

For Ni^{2+} ion, the g factor is about 7% higher than 2 when water is present in the gallery indicating the effect of spin-orbit coupling as

	Mn²⁺	Co²⁺	Ni²⁺	Cu²⁺
Hydrated	1.95	2.21	2.17	2.32
Dehydrated	1.98	2.48	2.29	2.48
Rehydrated	1.93	2.21	2.14	2.26

Table IV.1 The Lande g factor calculated from the effective moments of different ions under different hydration conditions.

well. When water is removed, the g factor increases by an additional 6% to a value of 2.29. This result is close to what has been observed in other Ni^{2+} complexes such as $\text{Ni}^{2+}(\text{H}_2\text{O})_6$ which normally has g value of 2.25.³⁴

For Cu^{2+} ions, the g factor value is 2.28 ± 0.3 when water is present and increases by about 8.7% when water is removed. The study of Cu^{2+} in many complexes has been reported³⁵ and the g values are more or less the same as what we have observed here.

As we can see, the g factors of these magnetic intercalants in dehydrated CIC are always larger than that of hydrated/rehydrated compounds (except Mn^{2+}). This can be caused by either the change of crystal field strength or the symmetry as mentioned. To address the theoretical origin of the behavior of the g factors for these cations in the gallery is quite difficult for following reasons.

First the localized wave functions of the electrons in a solid, which are the spatial Fourier transform of the Bloch's waves, are the Wannier functions which may not be the same as the atomic wave functions. They are atomic functions heavily perturbed by the crystal environment and are difficult to obtain (one common numerical method is the Hartree-Fock self-consistent method, see ref.32, p344). To first order, one can approximate these functions by atomic wave functions and apply crystal field theory to obtain the energy spectrum and other properties by using symmetry arguments³⁶. This method is quite successful to obtain the energy spectrum and explain the paramagnetic behaviors of various magnetic compounds with localized spins. Therefore, we will employ this method to analyze our data here.

Secondly, the cation locations and their local symmetry are essential to their magnetic properties and need to be understood. In this particular clay silicate, there are two situations to be addressed: with and without water in the gallery. As mentioned before, vermiculite has a stable phase with two layers of water at ambient conditions (normally referred as the 14.5Å phase). Many detailed investigations have been carried out to find out the arrangement of these interlayer water molecules and their relation to the host layers and the intercalants. The first postulation about the interlayer water arrangement in vermiculite was made by Hendricks and Jefferson³⁷ (1938) in which water molecules were thought to be in planar hexagonal rings with the oxygen of each water being tetrahedrally bonded to four neighboring oxygens through hydrogen atoms. No provisions for cation sites were made at that time. Later studies of the X-ray diffraction spectrum by Mathieson and Walker (1954)³⁸, Grudemo (1954)³⁹, and Mathieson (1958)⁴⁰ have demonstrated that the water molecules and exchangeable cations occupy definite sites in the interlayer spaces. In 1966, Shirozu and Bailey⁴¹ studied the interlayer water molecules in a Mg²⁺-ver single crystal from Llano (Texas) and confirmed the conclusions by Mathieson and Walker except for the delineation of different layer stacking sequences. Recently, de la Calle et.al. showed consistent results of the interlayer water arrangement and stacking sequences of a Mg²⁺-ver from Santa-Olalla, Spain.⁴² They have found the random b/3 shift between adjacent host layers in their hydrated sample.

The structural aspects for vermiculite are as follows. There is an a/3 shift within each layer along the X-axis parallel to the layer (see figure II.2 for the definition of the unit cell). And alternate layers

are displaced relatively to one another by $+b/3$ or $-b/3$ along the Y-axis. In the sample Shirozu and Bailey have studied, the c-axis stacking sequence is regular ($+b/3, -b/3, +b/3, -b/3, \dots$) with occasional mistakes. And in De La Calle's sample, there is no regularity for the $b/3$ shift. The stacking view of two basal oxygen layers on top of each other with a mutual $b/3$ shift has been illustrated in Figure II.3 in Chapter II. The exchangeable Mg^{2+} cations lie in a plane midway between adjacent host layers and have a plane of water molecules on each side. These cations and water molecules take the form of an incomplete octahedral sheet with only a portion of the sites occupied. Exchangeable cations lie under or above the Al^{3+}/Si^{4+} substitutional sites. Studies by Shirozu and De La Calle further showed that cations probably reside at one of the three possible sites: m_1 sites in Figure II.4. The relative positions between basal oxygens, water molecules and cations are also shown in Figure II.4. Exchangeable cations are surrounded by six water molecules and the crystal field is dominated by these water molecules.

There are no detailed studies on the stacking sequence of vermiculite after water is taken out of the gallery spaces. It is reasonable to assume that the stacking sequence is unchanged because the $b/3$ shift is energetically favorable (the basal oxygens avoid each other in this staggered stacking configuration). Therefore, one can suppose that intercalants still reside in m_1 sites as water is taken out. In this case, they are coordinated by six basal oxygens and the symmetry of the crystal field is unchanged.

Let us first discuss hydration/rehydration compounds. Bleam has shown that the static electric potential from host layers becomes

insignificant when an intercalant is more than 2 Angstrom away from the host layer.⁴³ Therefore we only have to consider the potential resulting from the water molecules themselves. The detailed arrangement of a cation and its surrounding water molecules is shown in figure IV.1. Basically there are six water molecules surrounding close to a cation to form a distorted octahedron. The symmetry of the crystal field is C_{3v} and can be approximated as an O_h field with a trigonal distortion along one of the C_3 axes which is the c-axis of the sample.

The Hamiltonian for a single ion in a solid can be written as

$$\begin{aligned}
 H &= -\frac{\hbar^2}{2m} \sum_i \nabla_i^2 - \sum_i \frac{Ze^2}{r_i} + \frac{1}{2} \sum_{i \neq j} \frac{e^2}{r_{ij}} + V_c + \lambda \vec{L} \cdot \vec{S} \\
 &= H_{ion} + V_c + \lambda \vec{L} \cdot \vec{S} \quad (IV.1)
 \end{aligned}$$

where the first term is the kinetic energy, the second term is the Coulomb potential, the third term is the electron-electron interaction term, V_c is from the crystal field, and the last term is the spin-orbit interaction (λ is the coupling constant). For the first transition group, the electron-electron interaction is normally stronger than V_c and the spin-orbit coupling is the smallest term in (IV.1) (see ref. 44, p58). Therefore, we start from the ground state of H_{ion} and treat V_c as a perturbation. The spin-orbit coupling will be treated as a further perturbation.

The detailed mathematical calculation of energy spectrum for a Ni^{2+} and a Co^{2+} ion in an O_h field with trigonal distortion is explained in Appendix I. We have chosen the c-axis, which is one of the C_3 axes of the octahedron, as the axis of quantization. The ground state of a free

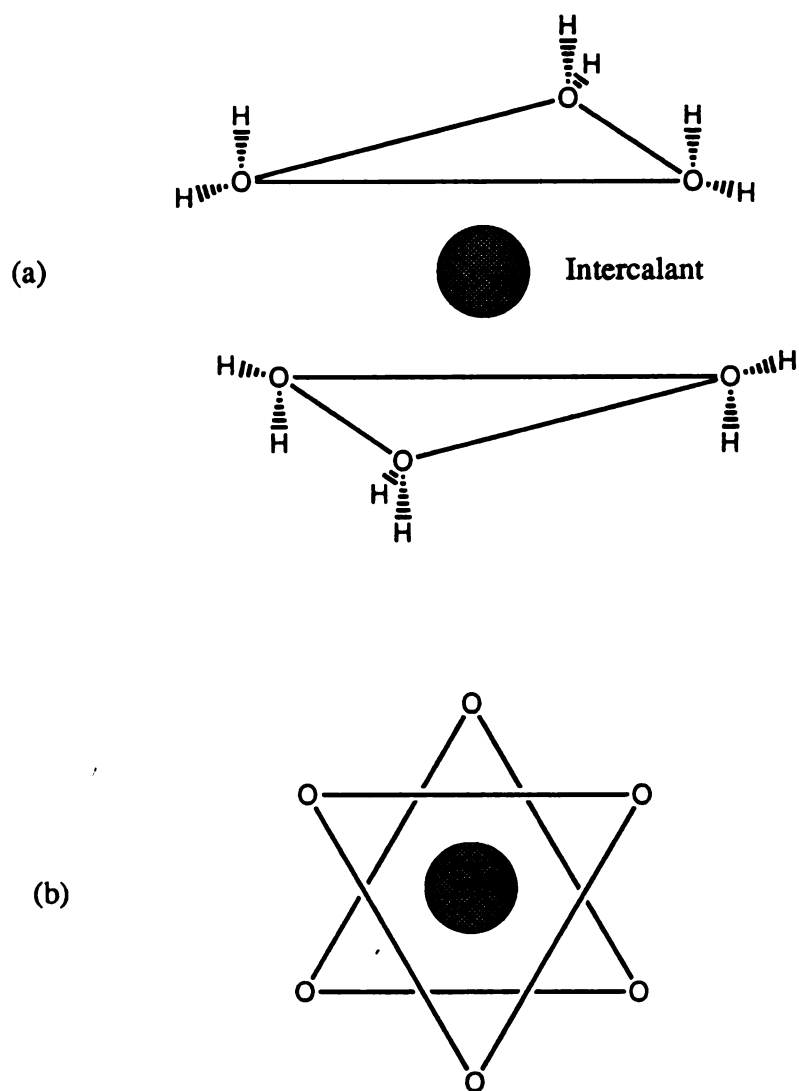


Figure IV.1 Schematic illustration of a gallery cation surrounded by six water molecules at ambient conditions. (a) side view. (b) top view.

Ni^{2+} and Co^{2+} ions is 3F and 4F , respectively. When they are put in the crystal field, they behave as a single f electron with an orbital degeneracy of 7. The corresponding atomic energy level splits into three sublevels denoted as A_{2g} , T_{2g} , and T_{1g} , which are shown in Figure AI.1. The subscript g corresponds to those irreducible representations of the O_h group which are invariant under the inversion operation. The trigonal distortion causes both the T_{2g} and T_{1g} levels to split into a singlet and a doublet. A Ni^{2+} ion has the electronic structure $3d^8$ and it can be treated as a two-hole case. On the other hand, a Co^{2+} ion has the electronic structure $3d^7$. It can be treated as a half-filled shell with two extra electrons outside. It has been shown in Appendix I that the energy spectra for a Ni^{2+} ion and a Co^{2+} ion are just off by a sign. Two important parameters are the strength of the O_h field and the trigonal distortion, Dq and Dt . They are defined as follows

$$Dq = \text{Constant} \frac{1}{7\sqrt{4\pi}} \langle r^4 \rangle \quad (\text{IV.2})$$

$$Dt = \text{constant} \langle r^2 \rangle \quad (\text{IV.3}).$$

Here $\langle r^4 \rangle$ and $\langle r^2 \rangle$ are defined as follows

$$\langle r^m \rangle = \int f_{3d}^*(r) r^m f_{3d}(r) r^2 dr, \quad m = 2, 4 \quad (\text{IV.4})$$

while $f_{3d}(r)$ is the radial part of the $3d$ wave functions.

Without the trigonal distortion, the ground state for a Co^{2+} ion is an orbital triplet (${}^4T_{1g}$, where the superscript indicates the spin degeneracy) with wave functions θ_1 , θ_2 , and θ_3 defined in equation

(AI.2) of the appendix I. It happens that the g value for this triplet is very large ($g=4.333$).⁴⁴ This is because the spin-orbit coupling causes a very small energy splitting of this level (of the order of the spin-orbit coupling strength λ_{Co} , which is about 180 cm^{-1})⁴⁴ which results in a large g factor (the Lande g factor can be far from 2 as in some compounds such as $\text{Mg}(\text{CH}_2\text{COOH})_2 \cdot 4\text{H}_2\text{O}$ with Co^{2+} where the g factor is about 2.5 along one direction and 6.0 along another.⁵²). When the trigonal perturbation is switched on, the situation changes. The triplet ground state T_{1g} then splits into a doublet and a singlet (see figure AI.1). The new ground state is the singlet with wave function

$$\theta_3 = \frac{\sqrt{10}}{6} \left(Y_3^3 - \frac{4}{\sqrt{10}} Y_3^0 - Y_3^{-3} \right) \quad (\text{IV.5}).$$

This ground state gives a g value of 2. Therefore, the trigonal distortion transforms the ground state of Co^{2+} to a singlet and reduces the g factor to 2. Our observation is that g is about 2.21. The difference comes from the mixing between ground and excited states by the spin-orbit interaction. The first excited state is the doublet from T_{1g} with wave functions θ_1 and θ_2 . And the energy difference between the ground state and first excited state is $\frac{3}{2}Dt$.

For an orbital non degenerate ground state with spin-orbit coupling, the g factor is related to a second rank tensor $\vec{\Lambda}$ (see ref.24, p122) as follows:

$$g_{ij} = 2(\delta_{ij} - \Lambda_{ij}), \quad (\text{IV.6})$$

where λ is the spin-orbit coupling strength and δ_{ij} is the Kronecker delta function. The tensor Λ is defined as:

$$\Lambda_{ij} = \sum_n \frac{\langle 0 | L_i | n \rangle \langle n | L_j | 0 \rangle}{E_n^0 - E^0} \quad (\text{IV.7})$$

where $|0\rangle$ is the ground state, $|n\rangle$ is the excited state, L_i is the angular momentum operator, E^0 is the ground state energy, and E_n^0 is the excited state energy.

To first order, we only consider the mixing between the ground state (θ_3) and first excited state (θ_1, θ_2). Other excited states are located far apart and only gives small corrections to the g value. Furthermore, we ignore the splitting of θ_1 and θ_2 caused by spin-orbit coupling by assuming that this splitting is much smaller than the splitting between the ground state and the first excited state. By using relations such as $L_x = (L_+ + L_-)/2$, $L_y = (L_+ - L_-)/2i$ and expressions of θ_1 , θ_2 , and θ_3 in Appendix I, we have obtained the $\vec{\Lambda}$ tensor as follows

$$\vec{\Lambda} = \begin{vmatrix} 9/(8\Delta E) & 0 & 0 \\ 0 & 9/(8\Delta E) & 0 \\ 0 & 0 & 0 \end{vmatrix} \quad (\text{IV.8}).$$

Therefore, the g tensor is

$$\vec{g}_{Co} = \begin{vmatrix} 2-9\lambda_{Co}/(4\Delta E) & 0 & 0 \\ 0 & 2-9\lambda_{Co}/(4\Delta E) & 0 \\ 0 & 0 & 2 \end{vmatrix} \quad (\text{IV.9}),$$

and the average g is

$$\bar{g}_{\text{Co}} = \sum_i \frac{1}{3} g_{ii} = 2 - \frac{3\lambda_{\text{Co}}}{2\Delta E} \quad (\text{IV.10})$$

where $\Delta E = \frac{3}{2} Dt$ and λ_{Co} is the spin-orbit coupling strength which has a value of -180 cm^{-1} (spin-orbit coupling constants for various transition metal ions are given in table 4.1, ref.24). Our experimental result ($g = 2.21$) for Co^{2+} reveals that $Dt = 857 \text{ cm}^{-1}$. This value is much greater than the spin-orbit coupling constant $|\lambda_{\text{Co}}|$. However, we will show shortly that it is much smaller than the O_h field strength.

For a Ni^{2+} ion, the ground state is an orbital singlet, ${}^3A_{2g}$, which does not have any orbital angular momentum (i.e., the expectation values for L_x , L_y and L_z are zero). The g value for such a state is 2. Because of spin-orbit coupling, the ground state is mixed with excited states such as T_{2g} . Using the same procedures as for Co^{2+} , we have obtained the Λ tensor as follows

$$\vec{\Lambda} = \begin{vmatrix} 4/\Delta E & 0 & 0 \\ 0 & 4/\Delta E & 0 \\ 0 & 0 & 0 \end{vmatrix} \quad (\text{IV.11})$$

where $\Delta E = 10Dq - \frac{5}{2} Dt$. Therefore, we can obtain the g tensor for Ni^{2+} as follows

$$\vec{g}_{\text{Ni}} = \begin{vmatrix} 2-8\lambda_{\text{Ni}}/\Delta E & 0 & 0 \\ 0 & 2-8\lambda_{\text{Ni}}/\Delta E & 0 \\ 0 & 0 & 2 \end{vmatrix} \quad (\text{IV.12})$$

which gives an average g

$$\bar{g}_{\text{Ni}} = \sum_i \frac{1}{3} g_{ii} = 2 - \frac{16\lambda_{\text{Ni}}}{3\Delta E} \quad (\text{IV.13}).$$

Our results for Ni^{2+} ($\bar{g}_{\text{Ni}} = 2.16$, and $\lambda_{\text{Ni}} = -324\text{cm}^{-1}$) reveals a ΔE of $10,800\text{cm}^{-1}$. Notice that ΔE contains two parameters Dq and Dt . The trigonal parameter Dt has been found to be 875cm^{-1} . Therefore, we find that the O_h field strength from water is $10Dq = 13,000\text{cm}^{-1}$ which is larger than the trigonal perturbation Dt . It is also larger but of the order of what has been found in other complexes such as $\text{Ni}^{2+}(\text{H}_2\text{O})_6$ ($10Dq$ is about $10,000\text{cm}^{-1}$).³⁴

The field strength parameters from water molecules can be further verified by the average g factor from Cu^{2+} ions in hydrated/rehydrated vermiculite. A Cu^{2+} ion has $3d^9$ structure and can be treated as one $3d$ hole case. The energy spectrum for a $3d$ hole in an octahedral field is given in the literature and wavefunctions are given in Appendix II. The ground state (2e_g) is an orbital doublet. As shown in Appendix II, the trigonal distortion down shifts the ground state energy but will not lift the double degeneracy. The spin-orbit coupling $\lambda\vec{L}\cdot\vec{S}$ does not lift that degeneracy either. The Lande g value for such a state is still 2. Our observation from susceptibility measurements for Cu^{2+} is that $g = 2.28$. Again the difference is caused by the mixing between the ground state and higher excited states. Although there is a complication arising from the fact that the ground state is a doublet, we treat each Cu^{2+} ion as if it occupies each component of the ground state with equal probability (see Ref.24, p135 for detail). By mixing one component of the ground state with the excited states, and by using the same type of calculation as for Co^{2+} and Ni^{2+} , we have obtained the g tensor as follows

$$\vec{g} = \begin{vmatrix} 2-2\lambda/(10Dq+Dt)-4\lambda/(10Dq-2Dt) & 0 & 0 \\ 0 & 2-6\lambda/(10Dq+Dt) & 0 \\ 0 & 0 & 2 \end{vmatrix} \quad (\text{IV.14}).$$

And the average g is

$$\bar{g}_{\text{Cu}} = 2 - \frac{8\lambda_{\text{Cu}}}{3(10Dq+Dt)} - \frac{4\lambda_{\text{Cu}}}{3(10Dq - 2Dt)} \quad (\text{IV.15}).$$

Using the parameters from Co^{2+} and Ni^{2+} ($Dt=850\text{cm}^{-1}$, $10Dq=13000\text{cm}^{-1}$)

and $\lambda_{\text{Cu}} = -830\text{cm}^{-1}$, we obtained $\bar{g}_{\text{Cu}} = 2.252$ which is consistent with our observation for hydrated Cu^{2+} -ver.

Table IV.2 summarizes above calculated field strengths. The experimental result for Cu^{2+} and the calculated values are also compared in that table.

At this point we conclude the following. First, the fact that the g value for Co^{2+} ions is slightly larger than 2 can be explained by a small trigonal distortion on the O_h field. Secondly, the field strength $10Dq$ is of the right order of magnitude and is further confirmed by the Cu^{2+} data. The distortion strength Dt is about 1/15 of the O_h field strength. Thirdly, marked anisotropy for Co^{2+} , Ni^{2+} , and Cu^{2+} is evident.

When water is removed from the vermiculite gallery, as we discussed before, the intercalants will most probably stay in sites m_1 (see figure II.3 in Chapter II) where they are coordinated by six oxygens from basal planes of host layers. We can still treat the local symmetry as an octahedron symmetry with distortion along one of the C_3 axes. The resultant energy spectrum is the same as with water present but with different field strength. From the g factor of Co^{2+} , we have obtained

Hydrated	Mn ²⁺	Co ²⁺	Ni ²⁺	10Dq	Dt	Cu ²⁺
Experiment	1.95	2.21	2.155			2.26
Theory	2.00	2.21	2.155	13300	857	2.252

Dehydrated	Mn ²⁺	Co ²⁺	Ni ²⁺	10Dq	Dt	Cu ²⁺
Experiment	1.98	2.48	2.29			2.48
Theory	2.00	2.48	2.29	6900	375	2.484

Table IV.2 The crystal field strength 10Dq and Dt (unit cm⁻¹) calculated from the g factors of Co²⁺ and Ni²⁺ for different hydration conditions. Furthermore, g values for Cu²⁺ ion were obtained from these parameters.

the trigonal parameter $Dt=375 \text{ cm}^{-1}$. And from Ni^{2+} , the O_h field strength $10 Dq$ has been found to be 6900 cm^{-1} which is about half of the strength from water. The g value for Cu^{2+} has also been calculated by using Dq, Dt values and is found to be 2.484 which is very consistent with what has been observed in our experiment. These parameters are also listed in Table IV.2.

As can be seen, the field strength of the O_h field and of the trigonal perturbation decreases by a factor of 2 in the dehydrated compounds. This explains why the g factors for three different intercalants in dehydrated vermiculite are larger than in the hydrated compounds. And the anisotropy increases because the effect of spin-orbit coupling becomes more significant as the crystal field decreases.

The Lande g factor for these ions in vermiculite can be further measured independently using EPR technique. This is left out as a future work.

IV.3 The exchange interaction between magnetic ions and magnetic phase transition

In these magnetic clay intercalation compounds, the Curie-Weiss temperature θ is affected by the presence of H_2O molecules in the gallery. Table IV.3 shows the Curie temperatures obtained from the previous fitting. The numbers in parenthesis are from Suzuki et.al.³⁰.

When water is present in the gallery, all compounds do not exhibit any ordering for temperatures down to 2K although there are interactions between these intercalants, qualitatively consistent with Suzuki's results.³⁰

(a)

	Mn ²⁺ -ver	Co ²⁺ -ver	Ni ²⁺ -ver	Cu ²⁺ -ver
Hydrated	0.08(-0.7)	-1.98(-1.4)	4.13(10)	-1.16(0.6)
Dehydrated	-0.80	-7.07*	-0.66*	-1.16
Rehydrated	-0.10	-1.43	1.66	-0.77

(b)

	Mn ²⁺ -ver	Co ²⁺ -ver	Ni ²⁺ -ver	Cu ²⁺ -ver
Hydrated	0.03	-1.60	6.2	-4.64
Dehydrated	-0.03	-5.70*	-1.00*	-4.64
Rehydrated	-0.03	-1.14	2.50	-3.08
Type of J _{ex}	Isotropic	Anisotropic	Anisotropic	Anisotropic
Predicted ordering (2D system)	No	Yes	Yes	Yes

Table IV.3 (a) The Curie temperatures obtained from $\chi(T)$ for the compounds studied. Numbers in parenthesis are from Suzuki et al.³⁰. The asterisk indicates antiferromagnetic ordering observed. (b) The exchange energy obtained from (a).

In the case of Mn^{2+} , θ is very close to zero. When water is removed, it is about -0.8K indicating there is a small antiferromagnetic exchange interaction between two adjacent Mn^{2+} ions. This exchange interaction is weak and can be easily affected by the presence of water. θ is $\pm 0.1\text{K}$ about zero. The basic effect is that water tends to break the antiferromagnetic interaction between Mn^{2+} ions.

For Co^{2+} ions in the dehydrated sample, the Curie-Weiss temperature is -7.07K which also suggests that the interaction between two adjacent Co^{2+} ions is antiferromagnetic. As water is present, θ is still negative but its magnitude is reduced. This also demonstrates that water weakens the exchange interaction between Co^{2+} ions.

In Ni^{2+} -ver, θ shows a robust behavior. It is about -0.7K without water, which is the same as for Mn^{2+} . And it becomes positive when water is added to the gallery suggesting that there is a relatively strong ferromagnetic interaction between Ni^{2+} ions. Water appears to be the agent responsible for the transfer of ferromagnetic interaction between Ni^{2+} ions.

For Cu^{2+} -ver, the Curie-Weiss θ is always negative and of the order of -1K regardless of whether water is present or not.

It appears that the overall effect of water is to weaken the antiferromagnetic exchange interaction and to offers a channel for a ferromagnetic interaction. A quantitative theoretical consideration must be based on the exact structure of water molecules bonded to the cations and the host layers. It is beyond the scope of this thesis.

All four magnetic vermiculite CIC's without water exhibit a common behavior. There is an antiferromagnetic exchange interaction between adjacent cations. Thus, in the exchange Hamiltonian the J_{ij} is negative

(here J_{ij} is the exchange energy defined in (I.1) and i, j correspond to cations at $i^{\text{th}}, j^{\text{th}}$ sites). This phenomenon is consistent with the fact that almost all magnetic insulators are antiferromagnetic and it can be qualitatively explained by the Kramers-Anderson's superexchange theory.²⁰⁻²²

The intercalants in CIC's are far apart in these compounds so that the direct overlap between electron wave functions at two adjacent sites is too small to be considered (the distance between two adjacent cations is about 5.28\AA). Also there are no itinerant electrons present to mediate the magnetic interaction. The antiferromagnetic exchange interaction results from virtual d-electron transfer from one intercalant to another through the bridging anions, in our case the basal oxygen atoms. The magnitude of this kind of interaction depends on the hopping energy. Quantitative calculation involves an understanding of localized wave functions for both electrons on the cations and on the anions and involves an understanding of the lattice structure of the intercalants. Numerical estimation of t and U for compounds such as MnO by using atomic wave functions as the real functions have been reported.^{45,46} In our magnetic CIC compounds, it is not feasible because the lattice structure of the intercalants is not clarified since the $\text{Si}^{4+}/\text{Al}^{3+}$ substitutional sites, where the magnetic cations reside, are random. Also multiple anions will be involved which makes the calculation even harder.

Although there is always a weak interaction between spins in all four of our compounds, they show different behaviors in terms of magnetic ordering because of anisotropy. When water is present in the gallery, all compounds do not exhibit any signature of a phase

transition from a spin disordered state to an ordered state for temperatures in the range of 2K to 300K regardless of whether the exchange is ferromagnetic or antiferromagnetic. As we have found before, the g factor for Mn^{2+} ions is close to 2 and it is an isotropic system. For a two dimensional system with Heisenberg spin-spin interactions, it has been shown rigorously by Mermin⁴⁷ that there is no phase transition corresponding to a spin ordered state for $T > 0K$. Our observation for Mn^{2+} -ver is consistent with this theoretical conclusion. For Co^{2+} -ver and Ni^{2+} -ver compounds, although they are anisotropic systems, they don't order either and need further theoretical understanding. For Cu^{2+} -ver, the failure to magnetically order may be traced back to quantum fluctuation effect of an ion with small spin moment (see p704, ref.32 and ref.53).

For dehydrated compounds, Mn^{2+} -ver and Cu^{2+} -ver do not exhibit a phase transition for temperatures from 2K to 300K. The g factor for a Mn^{2+} ion is still close to 2 and ions interact isotropically while water is present in the gallery. And the quantum fluctuation in Cu^{2+} -ver may still quench the magnetic ordering.

In contrast, there is a peak in the susceptibility curves for Co^{2+} -ver and Ni^{2+} -ver compounds indicating the possibility of a phase transition occurring. As discussed in section III.3.1, the spin-orbit coupling will cause anisotropic g factor for Co^{2+} and Ni^{2+} in a distorted octahedral field. This anisotropy will also cause the spin-spin interaction at different lattice sites to be anisotropic (Ref.24, p250). Consider a pair of magnetic ions at lattice sites a and b, the Hamiltonian is $H = H_0 + H_1$ where H_0 is the unperturbed term and H_1 is the perturbation which is defined as follows

$$H_1 = J_{ab} \vec{S}_a \cdot \vec{S}_b + \lambda_a \vec{L}_a \cdot \vec{S}_a + \lambda_b \vec{L}_b \cdot \vec{S}_b \quad (\text{IV.16})$$

where J_{ab} is the exchange interaction between two ions, λ_a and λ_b are the spin-orbit coupling strength for each ion, \vec{L} and \vec{S} are the angular and spin momentum operators. By using Brillouin-Wigner perturbation theory (Ref.24, Appendix 2), one gets the effective Hamiltonian up to second order in the spin-orbit interaction and first order in the exchange

$$H_{\text{eff}} = H_0 + J_{ab} \vec{S}_a \cdot \vec{S}_b - \lambda_a^2 \vec{S}_a \cdot \vec{\Lambda} \cdot \vec{S}_a - \lambda_b^2 \vec{S}_b \cdot \vec{\Lambda} \cdot \vec{S}_b + \vec{\eta} \cdot \vec{S}_a \times \vec{S}_b \quad (\text{IV.17})$$

where the second rank tensor $\vec{\Lambda}$ is defined in section IV.2. The last term is called antisymmetric exchange interaction with

$$\vec{\eta} = \vec{\eta}_a - \vec{\eta}_b, \text{ where } \vec{\eta}_{a,b} = -\frac{\lambda_{a,b}}{i} \sum_{n_{a,b}} \frac{\langle 0 \ 0 \ | \ \vec{L}_{a,b} \ | \ n_{a,b} \ 0 \ \rangle_{\text{ex}}}{E_n^0 - E^0} \quad (\text{IV.18})$$

where a, b stands for two different lattice sites, $|0\rangle$ is the ground state, and $|n\rangle$ is the excited state. As Moriya pointed out,²⁶ such term will vanish if there is a inversion center between two spins and will exist otherwise. This effect forces spin a and b to lie in the plane perpendicular to $\vec{\eta}$. Thus, the exchange interaction will be anisotropic and yield an X-Y system or even an Ising system.

Figure IV.2 shows the distorted Kagome lattice (only one hexagon is shown). As one can see, there is no inversion center between two cations located two adjacent m_1 sites. One thus should expect an

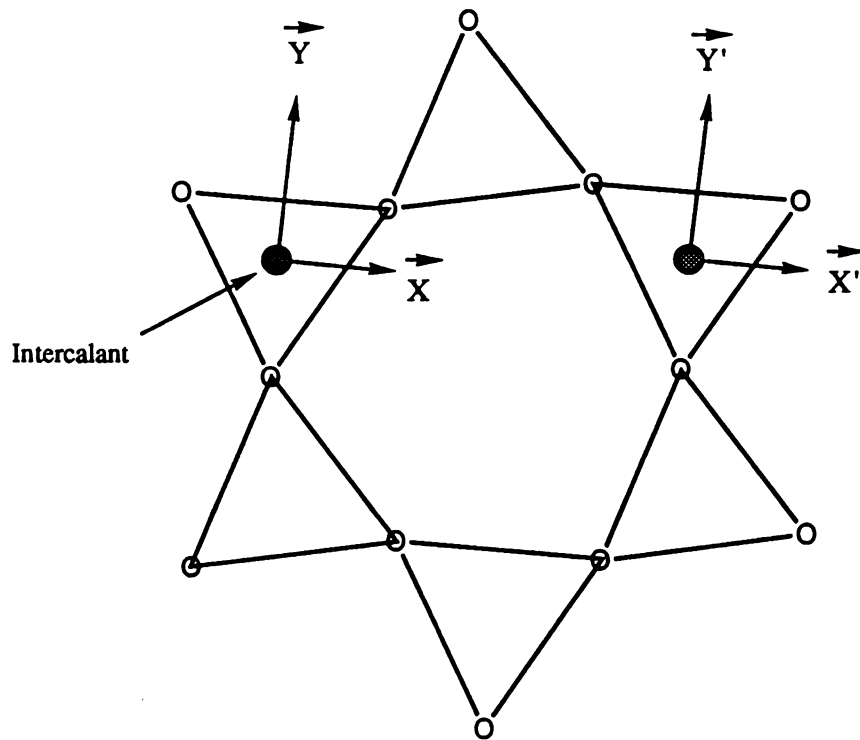


Figure IV.2 The Kagome lattice (only one hexagon is shown) with in plane distortion. Each tetrahedron is rotated 6 degrees clockwise or counterclockwise.

anisotropic exchange interaction between these two intercalants. Furthermore, the crystal field in dehydrated compounds is weaker than in hydrated/rehydrated compounds. This gives rise to additional anisotropy in the exchange interactions and may cause stronger correlations between spins in the Co^{2+} and Ni^{2+} compounds.

Finally, we consider the peak position (T_c) in χ for Co^{2+} -ver and Ni^{2+} -ver (about 5 ± 1 K and 3 ± 1 K, respectively). As we recall, Co^{2+} and Ni^{2+} ions have spins of $3/2$ and 1 , respectively. And T_c represents the transition temperature at which the magnetic ordering occurs. To gain insight into the phase transition in these two CIC compounds, we make the following assumptions. First we simplify the lattice as an two dimensional rectangular lattice, which is the possible lattice arrangement of the interlayer intercalants for the half-filled Kagome lattice³⁰ (there is one divalent ion per unit cell $\vec{a} \times \vec{b}$ in figure II.2), with anisotropic exchange interaction J_1 and J_2 along two directions (see figure IV.3). Secondly we treat the interaction to be Ising-like since the interaction between two intercalants in Co^{2+} -ver and Ni^{2+} -ver are anisotropic. These assumptions are the simplification of our systems. The Hamiltonian is

$$\begin{aligned}
 H_{\text{ex}} &= - 2J_1 \sum_{i,j} S_{z i,j} S_{z i+1,j} - 2J_2 \sum_{i,j} S_{z i,j} S_{z i,j+1} \\
 &= - 2J_1 S^2 \sum_{i,j} \sigma_{z i,j} \sigma_{z i+1,j} - 2J_2 S^2 \sum_{i,j} \sigma_{z i,j} \sigma_{z i,j+1} \quad (\text{IV.19})
 \end{aligned}$$

where i, j correspond to a cation at i^{th} row and j^{th} column.^r The 2D Ising system has a closed analytical form for the transition

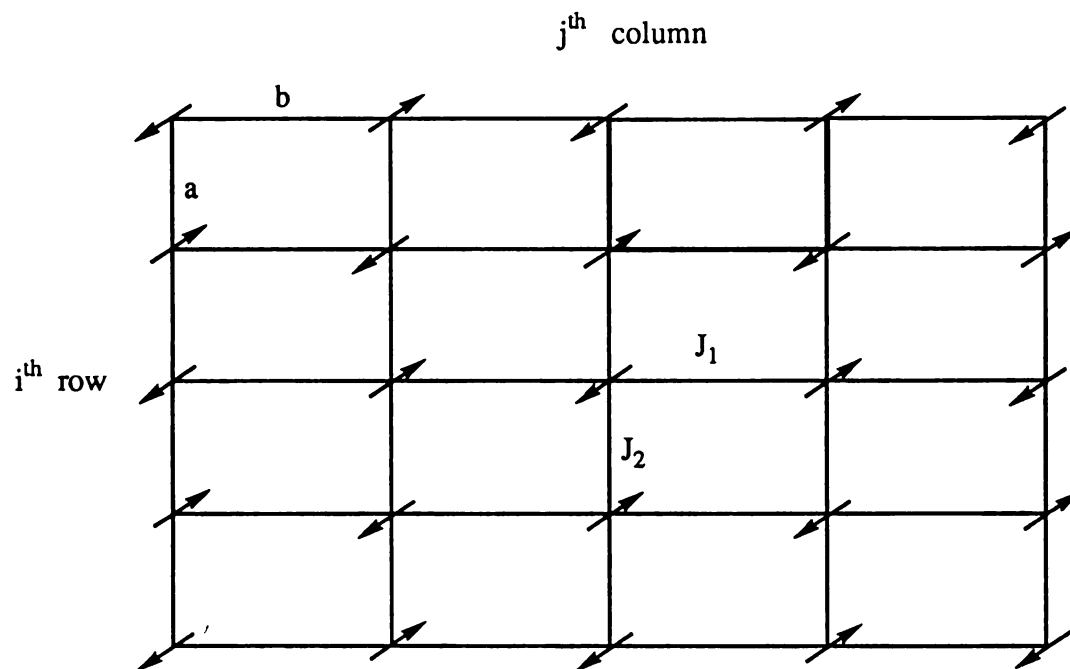


Figure IV.3 A rectangular Ising system with anisotropic interactions. J_1 is the exchange coupling along rows and J_2 is along columns

temperature^{48,49}

$$\text{Sinh}\left(\frac{2|J_1|s^2}{k_B T_c}\right) \cdot \text{Sinh}\left(\frac{2|J_2|s^2}{k_B T_c}\right) = 1 \quad (\text{IV.20})$$

J_1 and J_2 are the exchange interaction between two electrons at two lattice sites and they are the same in Co^{2+} -ver and Ni^{2+} -ver. There is an unique solution of S^2/T_c in above equation for a fixed J_1 and J_2 . Therefore, T_c should be proportional to S^2 . Thus a system with larger spin moment will have a higher transition temperature. This is consistent with our experimental observation. Furthermore, the S^2/T_c ratio for Co^{2+} and Ni^{2+} is 0.45 ± 0.1 and 0.38 ± 0.1 respectively. They are almost equal within their errors showing that our observations are consistent with the theoretical predictions.

IV.3 Concluding remarks

In this chapter, the average Lande g factors for different intercalants under different hydration conditions have been obtained and analyzed by using crystal field theory. We have estimated the crystal field strengths for hydrated/rehydrated compounds as well as for dehydrated compounds. Substantial decreases in crystal field strengths have been found when water is removed from the gallery. Furthermore we have verified the physical origin of the anisotropy and discussed the effect of spin-orbit coupling on both the paramagnetic g factors and the spin-spin exchange interactions in these compounds.

The effect of water on the magnetic interaction in these compounds has been investigated and discussed. All hydrated/rehydrated compounds do not exhibit magnetic ordering consistent with previous work³⁰. Water molecules weaken the antiferromagnetic interaction and destroy the ordering. We have observed for the first time the antiferromagnetic ordering in Co^{2+} -ver and Ni^{2+} -ver when water is removed from the gallery.

Mn^{2+} -ver is found to be a Heisenberg isotropic system under either hydrated/rehydrated or dehydrated conditions. Therefore, there is no phase transition for temperatures down to 2K. On the other hand, the exchange interactions in Co^{2+} -ver, Ni^{2+} -ver and Cu^{2+} -ver are anisotropic. Co^{2+} -ver and Ni^{2+} -ver exhibit signatures of a phase transition at very low temperature (~5K and ~3K, respectively) without water in the gallery. The spin dependence of the transition temperatures for dehydrated Co^{2+} -ver and Ni^{2+} -ver has been explained by a very simple 2D Ising model. Although Cu^{2+} -ver is an anisotropic system as are Co^{2+} -ver and Ni^{2+} -ver, it does not exhibit magnetic ordering for temperatures from 2K to 300K. This phenomenon may be related the fact that it is a quantum fluctuating system.

Chapter V
Diffusion and absorption of inert gases
in mixed ion systems

V.1 Introduction

Heteroionic clays with different cations in the gallery are particularly interesting for studying access phenomena in 2D microporous systems by probing the conduction and absorption of atomic and molecular species. In percolation experiments on real systems, the dynamic physical quantity measured is, for examples, the electrical conductivity or the mass conductivity as a function of disorder. For the systems of interest here which are ternary intercalated layered silicates $A_{1-x}B_x-Y$, where Y is the host layer, and A and B represent the cation with different physical properties such as size, the mass conductivity of a third guest species is studied. The basic picture is quite simple and can be described as follows. The third guest is denoted as C in this thesis. Suppose that the gallery structure is such that species C can easily diffuse through the $A_{1-x}B_x-Y$ system and the mass conductivity is finite when $x=0$. On the other hand the gallery space does not allow any C particles to move through for $x=1$. With increasing x there exists a critical value, which is the percolation threshold x_c , at which the mass conductivity for C is zero and remains so for $x_c < x < 1$. Therefore, by studying the permeability of the host to the guest species C, one can in principle probe interesting physical phenomena such as anomalous diffusion at the threshold concentration x_c which has attracted considerable theoretical and experimental interest in recent years.⁵⁶

In addition to diffusion studies, one can also study the access phenomena by measuring weight uptake and the absorption isotherm. The physical quantity measured here is $W^C(x)$ ($= M(x)/M_T(x)$, where $M(x)$ is the absorbed mass of C for a given x , and $M_T(x)$ is the total absorption mass that can be obtained when all available interlayer surface is occupied by C). There is an x_c above which there are no percolation channels through which C can pass to the available spaces in the gallery. The exact form of $W^C(x)$ and the value of x_c can be determined from percolation theory.

It is very important to understand the structural aspects of our ternary mixed ion system. The porosity in pillared lamellar solids such as $A_{1-x}B_x-Y$ is crucial for percolation to happen. The method used to characterize microporosity in terms of the sizes and the spatial distribution of the cations is as follows: Assume that the cation A and B and diffusing molecule C can be represented as ellipsoids of revolution with diameters $(2r_A, h_A)$, $(2r_B, h_B)$, and $(2r_C, h_C)$. The topological constraints on the access of a guest C in the gallery spaces will depend on the geometric property of the pillars and the adsorbate through the following five parameters: $\delta_{AA} = (a - 2r_A)/2r_C$, $\delta_{AB} = (a - (r_A + r_B))/2r_C$, $\delta_{BB} = (a - 2r_B)/2r_C$, $\delta_{AC} = h_A/h_C$ and $\delta_{BC} = h_B/h_C$. Here a is the distance between two gallery cations. Any given geometric condition for the diffusion of C inside $A_{1-x}B_x-Y$ is completely determined by the five member set of the above specified parameters (porosity parameters). Define the porosity parameter set S as

$$S = [s_1, s_2, s_3, s_4, s_5] = \{s_i\} \quad (V.1)$$

and assigning $s_1 = +1$ if $\delta_{AA} > 1$ and $s_1 = -1$ if $\delta_{AA} < 1$, and so on for other s_i . There are total 32 distinct porosity sets for some of which there is no conduction and for some of which the intergallery space is completely permeable for all x . They are given in table V.1. As one can see, many of them are not physically significant. Those that are significant can be selected by a judicious choice of the species A, B, and C.

The choice of the porosity parameters is limited by the available pillaring agents. Table V.2 lists dimension of some of the agents one can insert in to the gallery of a clay host. In order to perform the mass conduction measurement, the diffusing species should be such that they do not have any chemical reactions with the host or with intercalants. Inert gases are thus an ideal choice for the diffusing species.

We have chosen $[\text{Co}^{3+}(\text{en})_3]_{1-x}[\text{Cr}^{3+}(\text{en})_3]_x$ -Fluorohectorite (where en = ethylenediamine, and fluorohectorite is a layered silicate denoted as FHT) as the ternary mixed ion system and Argon as species C under the following considerations. First, pillaring agents such as $\text{Co}(\text{en})_3^{3+}$ and $\text{Cr}(\text{en})_3^{3+}$ have very large dimensions as can be seen from table V.2. They prop up the gallery to a height of 5.4 \AA which is suitable for Argon atoms (dynamical size = 4 \AA). Secondly, they are trivalent ion complexes which are far separated in the gallery so that the lateral dimensions between them are large enough for Argon to pass through (the average distance between two adjacent intercalants is about 10.22 \AA). Thirdly, there are no water molecules in the $[\text{Co}(\text{en})_3^{3+}]_x[\text{Cr}(\text{en})_3^{3+}]_{1-x}$ -FHT because three en ligands fully coordinate the Cr^{3+} and Co^{3+} ions. These structural characteristics indicate that this system should be

Porosity set	S₁	S₂	S₃	S₄	S₅	Percolation
S_I	+	+	+	+	+	Open
S_{II}	-	+	+	+	+	L-S
S_{III}	-	-	+	+	+	L-B
S_{IV}	+	+	+	-	+	V-S
S_V	-	+	+	-	+	L-S/V-S
S_{VI}	-	-	+	-	+	L-B/V-S
S_{VII}	+	+	+	+	-	V-S
S_{VIII}	-	+	+	+	-	L-S/V-S
S_{IX}	-	-	+	+	-	L-B/V-S
S_X	All remaining 23 combinations					Closed

Table V.1 Porosity sets and their corresponding behavior. L=laterally controlled, V=vertically controlled, S=site, B=bond. Open=non-percolative systems.

Ion	Diameter	Height
Me₄N⁺	4.8	4.2
Me₃NH⁺	4.0	3.2
MeNH⁺₃	3.2	2.8
NH⁺₄	2.8	1.5
Co(en)₃³⁺	5.4	5.4
Cr(en)₃³⁺	5.4	5.4

Table V.2 Dimensions of pillaring agents. Diameters and heights are in unit of Angstrom.

open to Argon atoms for all concentration x .

The most interesting and important characteristics of these two pillaring agents are as follows. $\text{Co}^{3+}(\text{en})_3$ and $\text{Cr}^{3+}(\text{en})_3$ have different responses to heat. When the sample is heated at between 100C and 150C, a $\text{Co}^{3+}(\text{en})_3$ complex will be break into $[\text{Co}^{3+}(\text{en})_2+\text{en}]$. What happens is that an en ligand is dissociated from its parent complex and this ligand remains in the vicinity of the original complex cation, while $\text{Cr}^{3+}(\text{en})_3$ cations remain unchanged. It turns out that $[\text{Co}^{3+}(\text{en})_2+\text{en}]$ has smaller vertical dimension (about 3.8 Å) and larger lateral dimension (more than 6 Å) than the parent cation. Argon atoms can not pass through the lateral space between a pair of $[\text{Co}^{3+}(\text{en})_2+\text{en}]$ and between $[\text{Co}^{3+}(\text{en})_2+\text{en}]$ and $\text{Cr}^{3+}(\text{en})_3$ (see figure V.1 for schematic view), while they still can pass between two $\text{Cr}^{3+}(\text{en})_3$ cations. Thus, the annealed system ($[\text{Co}^{3+}(\text{en})_2 + \text{en}]_x[\text{Cr}^{3+}(\text{en})_3]_{1-x}$ -FHT) has porosity parameter set { -, -, +, -, +}, which is identified as S_{VI} in table V.1. As we can see, this system should be percolative. Figure V.1 shows the inplane structure of FHT with $\text{Co}^{3+}(\text{en})_3$ and $\text{Cr}^{3+}(\text{en})_3$ as intercalants before and after annealing. The actual distance between two adjacent intercalants is larger than illustrated because the charge/unit cell for this particular FHT is $1.6e^-$ instead of $2.0e^-$.

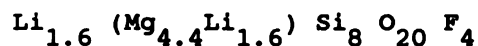
We now present our experimental results for mass absorption of Argon in $[\text{Co}(\text{en})_3]_x[\text{Cr}(\text{en})_3]_{1-x}$ -FHT bulk. It has been found that the mass uptake of Argon in the annealed $[\text{Co}(\text{en})_3]_x[\text{Cr}(\text{en})_3]_{1-x}$ -FHT shows an interesting behavior which indicates a percolative process.⁵⁴

In order to obtain direct evidence of the dynamical movement of Argon atoms in the gallery of this mixed ion clay system, we have also performed studies of mass conduction of Argon in the unannealed and

annealed $[\text{Co}(\text{en})_3]^{3+}$ -FHT films. Although Argon atoms can move in the gallery space of this particular sample before annealing, they are blocked after annealing since the gallery collapses and the gallery space is blocked by the dissociated ligands. Besides diffusing Argon, we have used Helium to prob whether the sample is complete blocked by undesired reasons such as the seal off by glue. Since the diffusion rate of Argon is expected to be very small, we have perform the diffusion studies of Argon in a thin $[\text{Co}(\text{en})_3]^{3+}$ -FHT membrane. A special experimental set up with high sensitivity and a unique technique to diffuse gases through thin membranes has been developed. We have successfully observed the complete blockage of Argon in the annealed film which gives a strong evidence for the dynamical movement of guest species in the gallery spaces between the cations.

V.2 Experiment and results

The starting material is Li^+ -Fluorohectorite⁵⁰ which is a trioctahedral 2:1 layered silicates with following unit cell stoichiometry (here Li^+ is the gallery cation):



The main structure is essentially the same as vermiculite.

Samples for mass absorption measurement were made through an ion exchange reaction by putting the parent compound to solutions with desired concentrations of $\text{Co}^{3+}(\text{en})_3$ and $\text{Cr}^{3+}(\text{en})_3$.^r Water molecules swell the gallery so that the ion exchange can take place. Once these

large complex particles enter the gallery, the compound stops swelling and reaches a state in which no water molecules are present inside the gallery. $\text{Co}^{3+}(\text{en})_3$ -FHT films for mass conduction experiment were made by immersing a self supporting Li^{2+} -FHT film into a dilute $\text{Co}^{3+}(\text{en})_3$ solution. As the ion exchange process terminates, the film stops swelling and do not ingest water even when immersed in the solution. The film thickness is about 15 μm . Annealing has been done by slowly heating samples in vacuum (starting from room temperature to 120 C with $\Delta T/\Delta t = 15$ C/hour, and remaining at 120C for another 6 hours). The in plane structure of $[\text{Co}(\text{en})_3^{3+}]_{1-x}[\text{Cr}(\text{en})_3^{3+}]_x$ -FHT before and after heating is schematically shown in figure V.1 which includes all structural aspects of the system as stated in introduction.

Figure V.2 shows the X-ray diffraction pattern of $\text{Co}^{3+}(\text{en})_3$ -FHT before and after it has been annealed. The c-axis basal spacing decreases from 14.45 \AA to 12.82 \AA . Other features in this pattern are broadening of (001) Bragg peak and the disappearance of higher Bragg peaks after the film has been annealed indicating shorter coherence length along c-axis and basal spacing fluctuation.

Figure V.3 presents the surface morphology of an oriented film sample and a bulk sample from a scanning electron microscope. As can be seen, the clay particles orient very well in the film while the bulk sample exhibits considerable amount of large voids (with dimension of order of micrometer). This is the other reason that we have chosen film sample. Even in the oriented film, there are small defects such as micro-cracks and voids which are unavoidable resulting in difficulties in the experiment.

The diffusing gas is applied perpendicularly to the surface of the

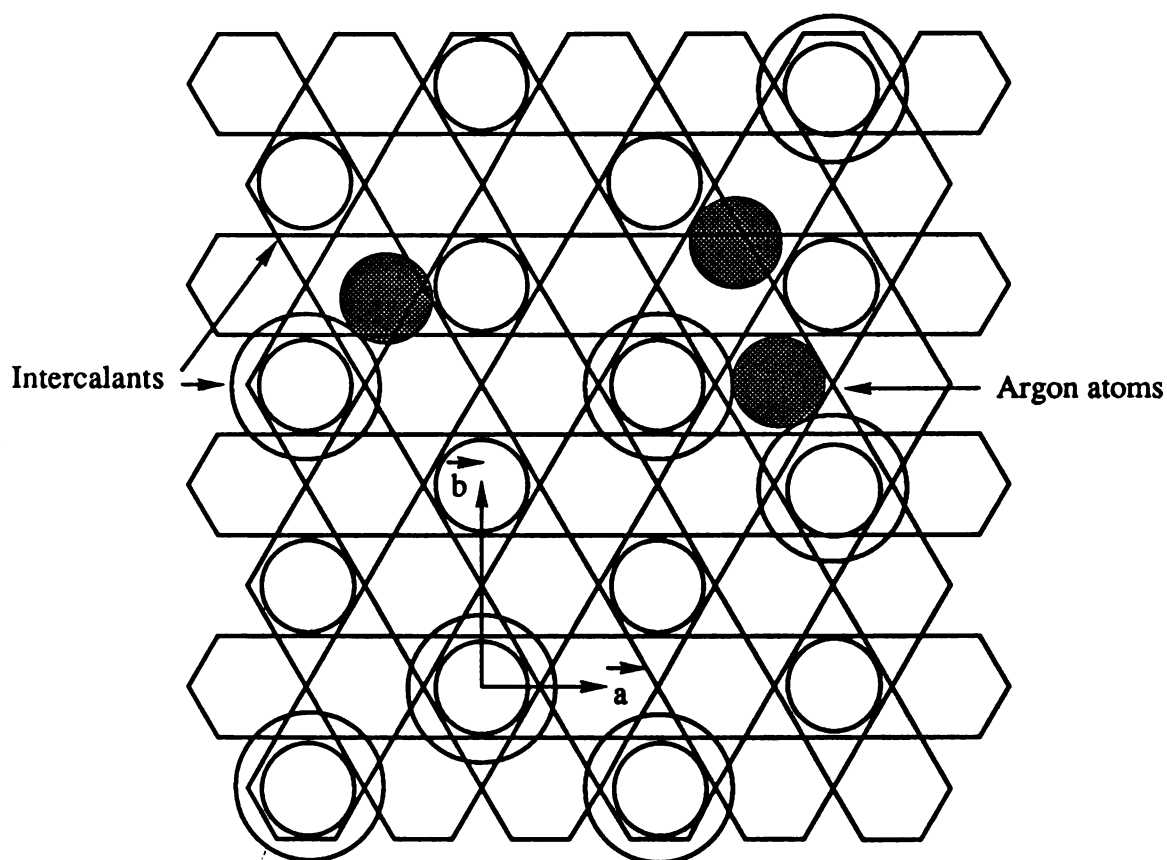


Figure V.1 The in plane structure of $[\text{Co}^{3+}(\text{en})_3]_{1-x}[\text{Cr}^{3+}(\text{en})_3]_x\text{-FHT}$. Single circles represent $\text{Cr}^{3+}(\text{en})_3$. Concentric circles present $\text{Co}^{3+}(\text{en})_3$, in which smaller circles are for before annealing and larger circles are for after annealing. $a=5.28$ angstrom, $b=9.15$ angstrom. Actual cation density is less than shown because unit cell charge is $1.6e^-$ instead of $2.0e^-$.

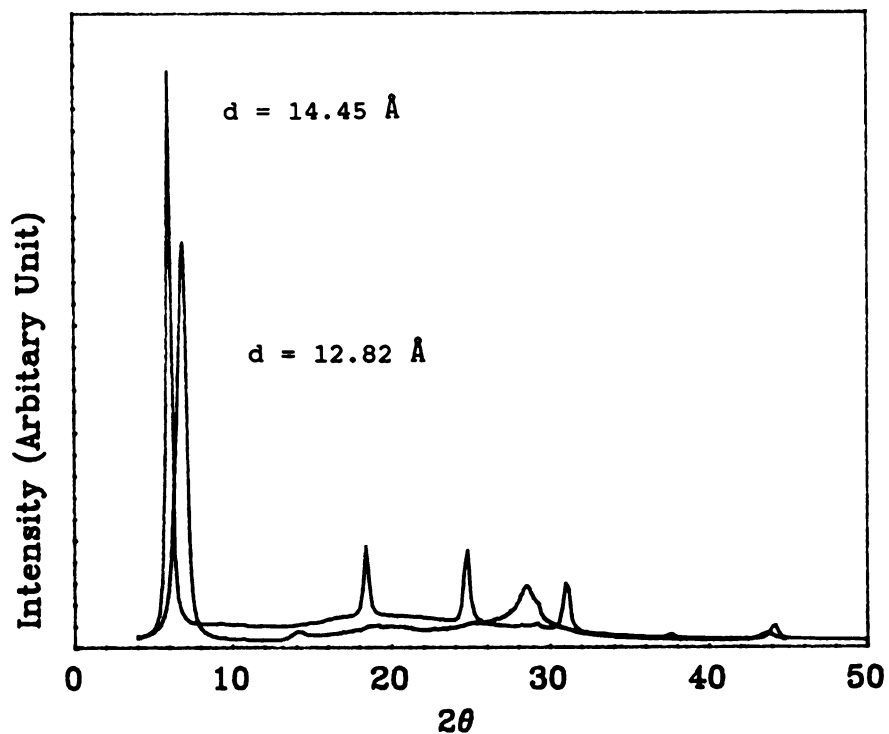
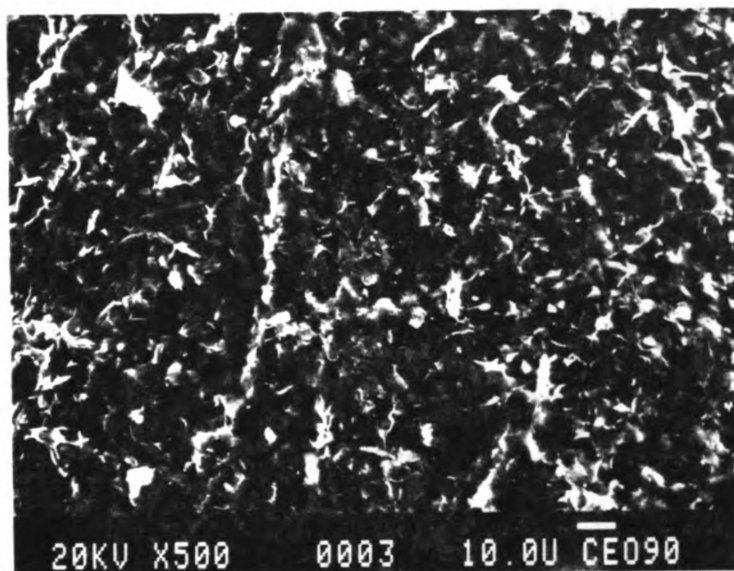
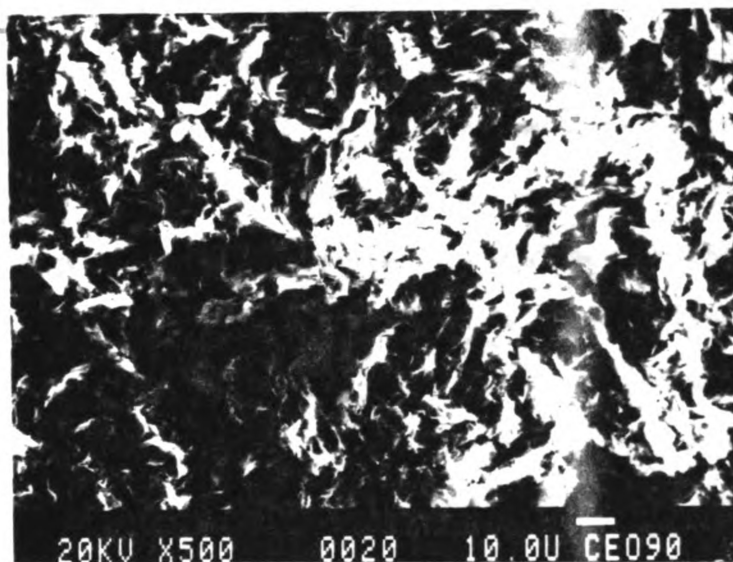


Fig. V.2 The X-ray diffraction patterns of $\text{Co}^{3+}(\text{en})_3\text{-FHT}$ before and after annealing (the c-axis basal spacings are respectively 14.45\AA and 12.82\AA). These patterns were acquired at the room temperature using Cu K_α radiation.



(a)



(b)

Fig. V.3 The surface morphology of $\text{Co}^{3+}(\text{en})_3\text{-FHT}$. Picture (a) is the surface SEM image of an oriented film and (b) is the image of a bulk sample.

oriented film. There are three possible channels for Argon to pass through in this particular geometry (illustrated in figure V.4). Path 1 can be a hole on the film or a channel of connected voids. This type of defect results in a huge background signal instantly. Path 2 is a so called void-grain boundary-void path. Diffusion through these two channels will not depend on whether or not the film is annealed. Path 3 is the void-gallery-void path. Diffusion through this channel will be different before and after the gallery is blocked as a result of annealing. The last situation is desirable and depends on the quality of the membranes.

Mass conduction measurement was carried out on an apparatus which is equipped with a residual gas analyzer and is automated by a personal computer (see figure V.5). A constant pressure of gas C is maintained in the reservoir and applied to the membrane, which is mounted on a sample holder to avoid leakage from other sources (also shown in figure V.5). The sampling chamber is always pumped to maintain a vacuum of normally 10^{-7} torr. The partial pressure of the interested gas is measured by a quadrapole residual gas analyzer and signals are sent to a IBM PC. Valves are controlled by the computer to accomplish certain specific functions at desired times. The mass absorption of Argon has also been conducted by using conventional gravimetric method.⁵⁴

Figure V.6 shows the amount of Argon absorbed for samples with different x (x is the concentration of $\text{Cr}^{3+}(\text{en})_3$) and for samples which are the direct physical mixture of two pure compounds.⁵⁴ They have been heated to the correct temperature range beforehand. As one can see, the amount of Ar absorbed in the physical mixtures shows a linear dependence on x because the amount of available gallery spaces are from $\text{Cr}^{3+}(\text{en})_3-$

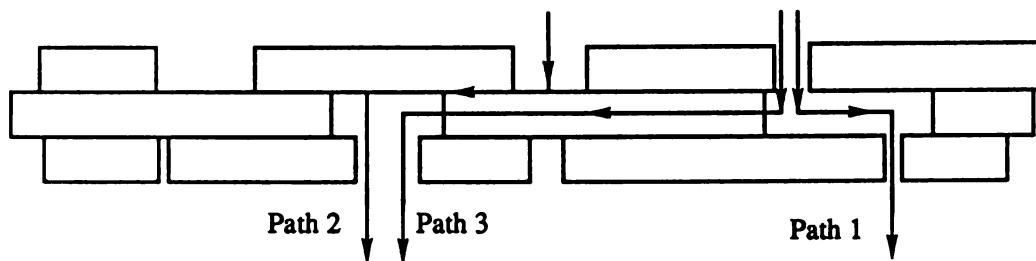


Figure V.4 Three possible path ways. Each clay particle is presented as a block.

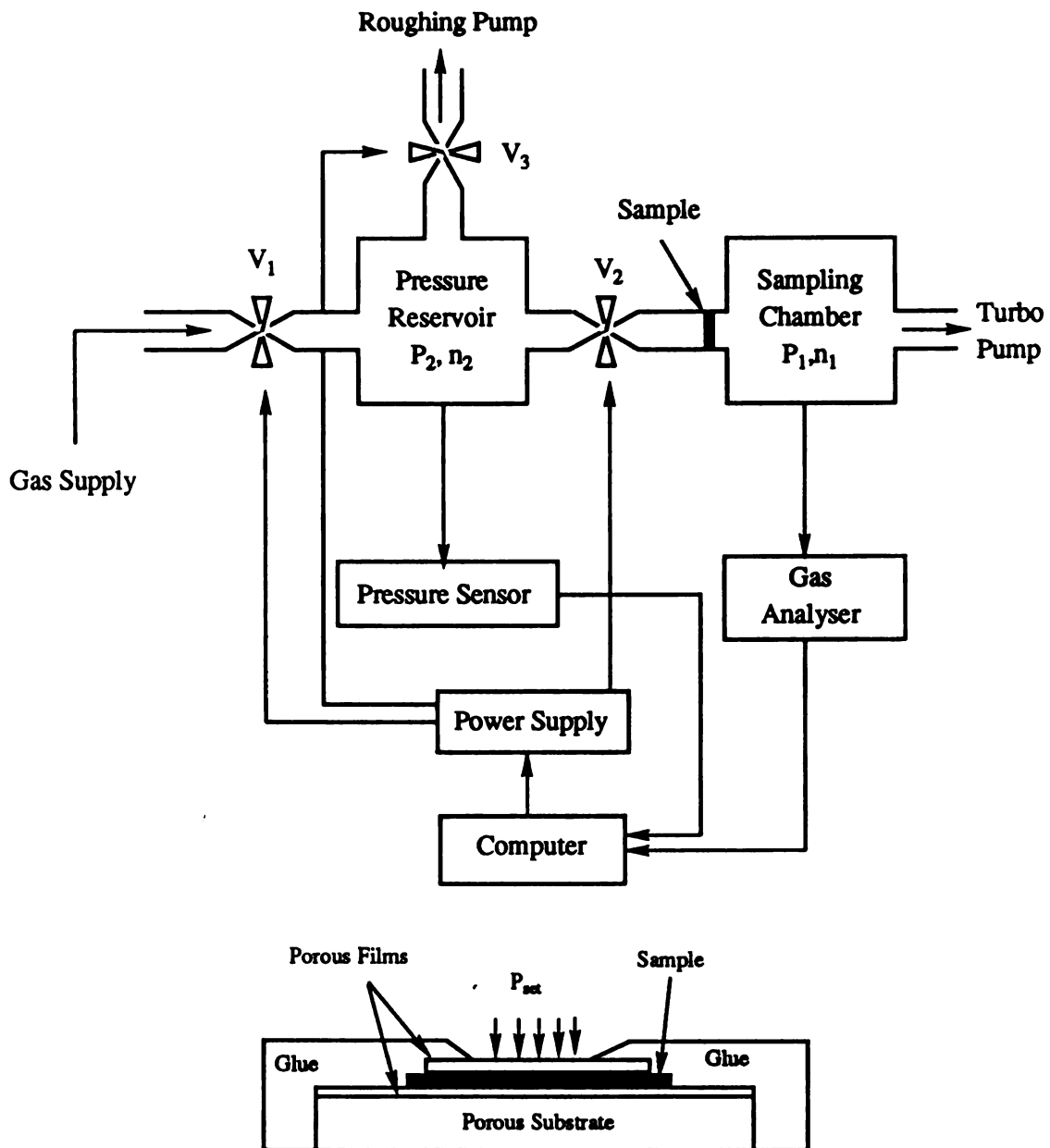


Figure V.5 Schematic illustration of experimental set up for mass conduction experiment. Sample is mounted as illustrated.

FHT and they are all accessible. When the two kinds of cations coexist in the gallery, the absorption isotherm is quite different and deviates from that of the physical mixtures. For $0 < x < 0.8$, the system does not take up Argon. As x exceeds 0.8, there is a sudden increase indicating that the system begins to open up to Argon.

In our diffusion experiment, we have found that Helium gas can quickly penetrate the unannealed $\text{Co}^{3+}(\text{en})_3\text{-FHT}$ film. The partial pressure of Helium in the sampling chamber goes to a saturation value within less than 30 seconds. As can be seen in figure V.7(a), the Helium saturation pressure show a linear dependence on the applied pressure in the reservoir. After annealing, Helium atoms still can penetrate the membrane, but with a much slower time scale (2000 seconds) and much smaller saturation pressures (see figure V.7 (b)).

Argon atoms penetrate the unannealed membrane as well. The time scale is about 2600 seconds for the partial pressure of Ar to reach a saturation value. After annealing, no Argon signals can be seen from the sampling chamber except the residual level (see figure V.8). This demonstrates that Argon atoms are totally blocked in the annealed film and the Argon signal we have seen in the unannealed membrane derives from the third possible path (void-gallery-void).

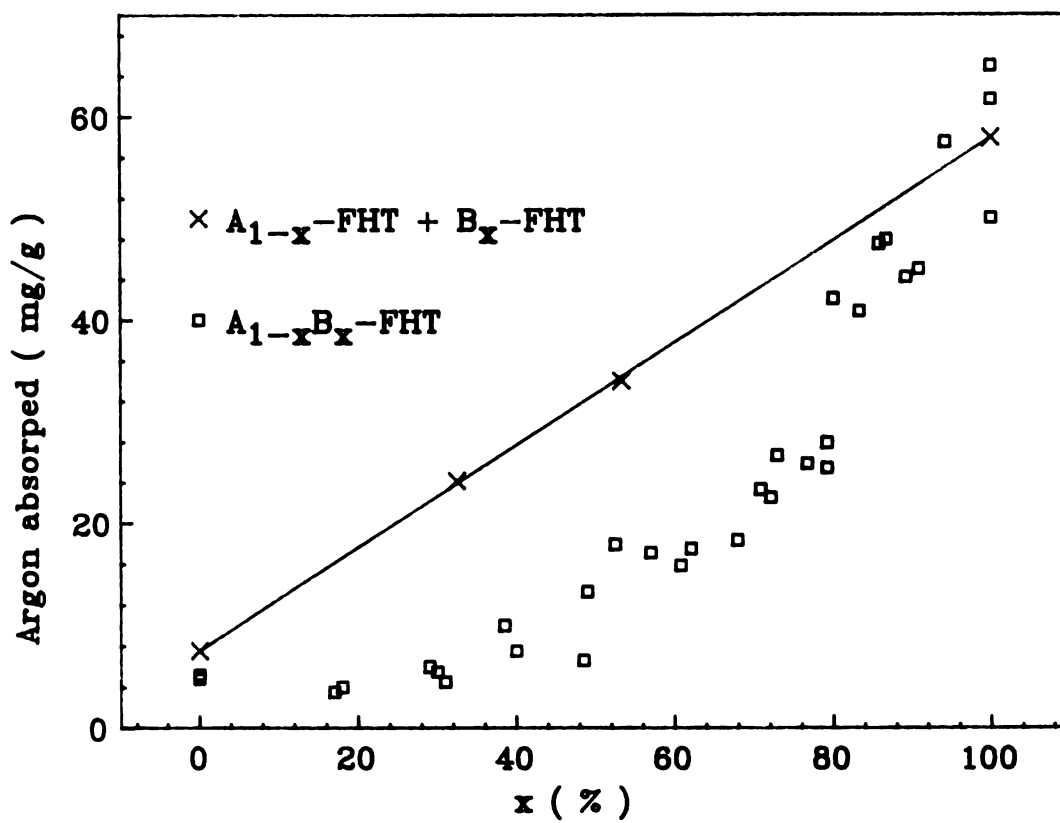
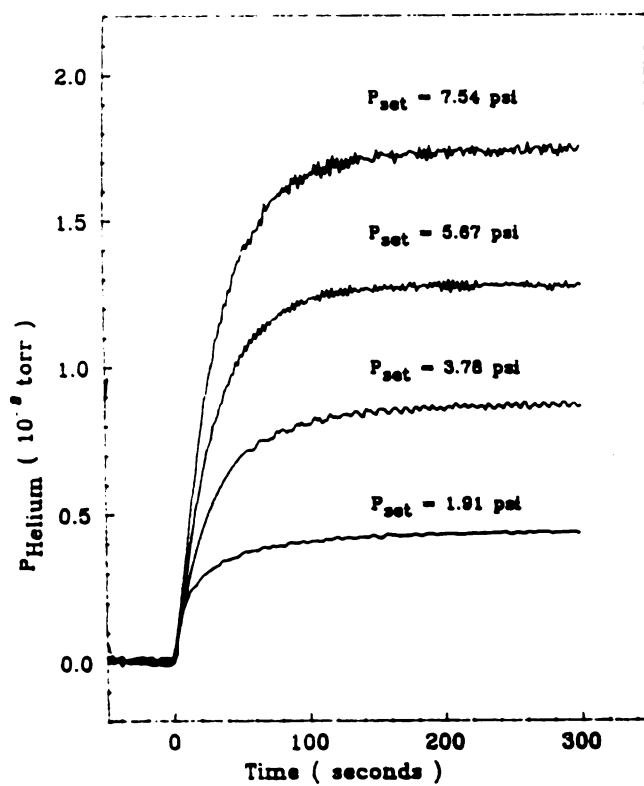
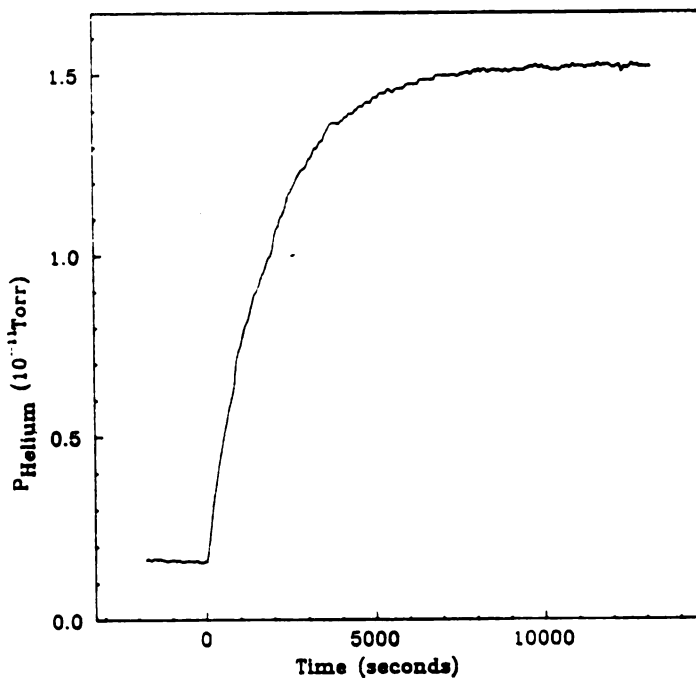


Fig. V.6 The amount of argon absorbed by $[\text{Co}^{3+}(\text{en})_3]_{1-x}[\text{Cr}^{3+}(\text{en})_3]_x\text{-FHT}$ and by the physical mixture of pure samples. (from Kim, et.al.)⁵⁴



(a)



(b)

Fig. V.7 Helium partial pressure in the sampling chamber versus time. The membrane is unannealed in the case of curve (a) and annealed in (b). P_{set} is the setting pressure in the reservoir.

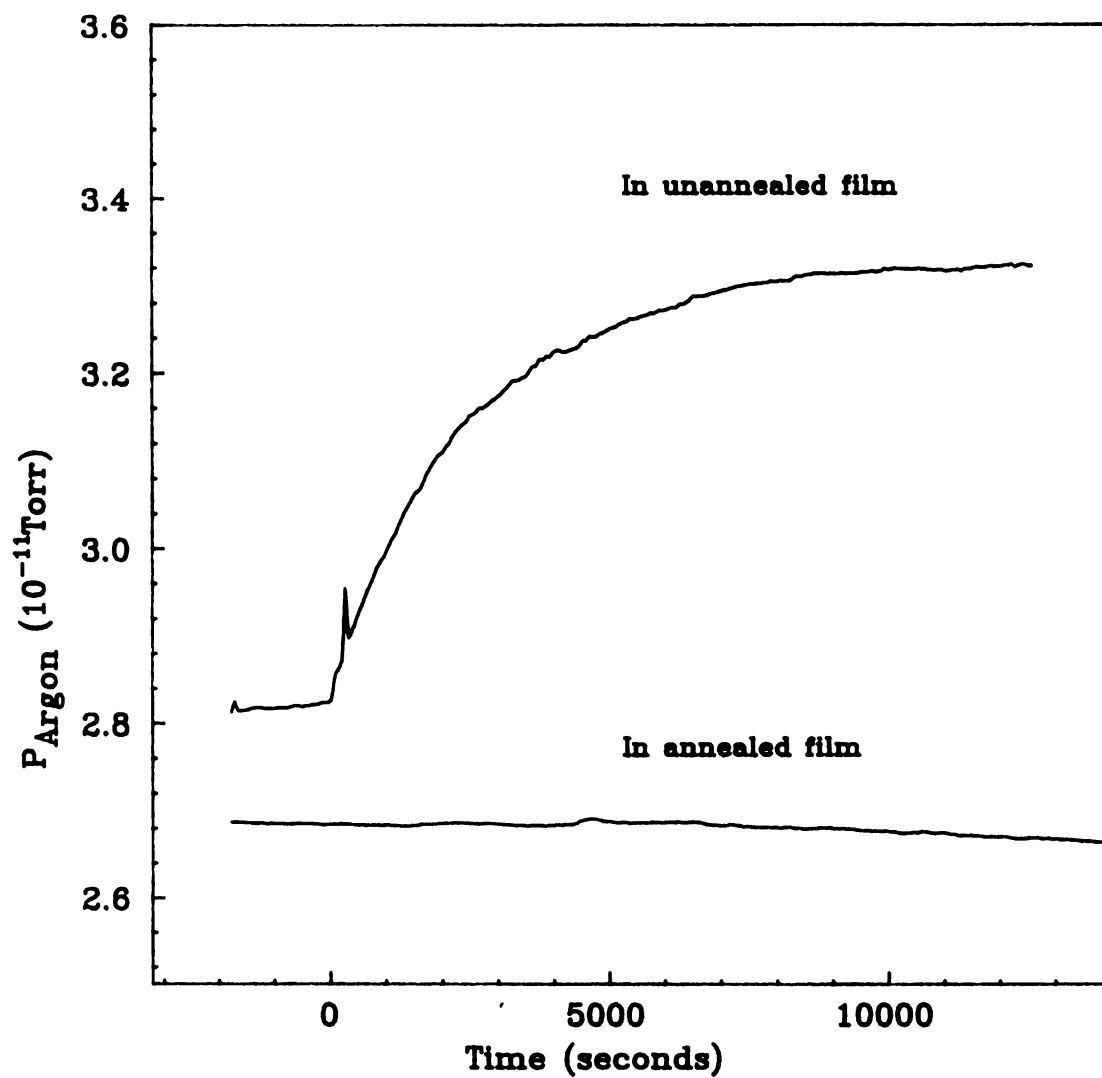


Fig. V.8 Argon partial pressure in the sampling chamber before the membrane is annealed (dashed line) and after it is annealed (solid line).

V.3 Discussions

It appears from the mass absorption data (figure V.6) that the mass uptake in annealed $[\text{Co}(\text{en})_3^{3+}]_{1-x}[\text{Cr}(\text{en})_3^{3+}]_x$ -FHT shows a percolative behavior with critical threshold $x_c \sim 0.8$. This is consistent with the results of simulation studies in which the two types of cations, $\text{Co}^{3+}(\text{en})_2+\text{en}$ and $\text{Cr}^{3+}(\text{en})_3$, are randomly distributed on a triangular lattice while only the space between two adjacent $\text{Cr}^{3+}(\text{en})_3$ intercalants is enough for the third species to pass through.⁵¹ These simulation studies reveal a percolation threshold at x_c of 0.8 in agreement with experiment. This value is relatively large and it is related to the fact that only the space between one of the three possible cation pairs (AA,AB, and BB, A = $\text{Co}^{3+}(\text{en})_2+\text{en}$, and B = $\text{Cr}^{3+}(\text{en})_3$) is large enough for Argon to pass through.

The diffusion experiment reveals some details of the dynamical movement of Argon and Helium in the $\text{Co}^{3+}(\text{en})_3$ -FHT film. To analyze our diffusion data, we have to divide them into four different situations for Helium (or Argon) in unannealed (or annealed) films and treat them separately since the dynamics will be different in each case.

V.3.1 Helium in the unannealed $\text{Co}^{3+}(\text{en})_3$ -FHT membrane

In this case the gallery is wide open to Helium atoms. Therefore, we can use the following diffusion equation to characterize the process:

$$\frac{V_1 dn_1}{dt} = D \frac{(n_2 - n_1)}{\ell} A' - S n_1 \quad (V.2)$$

where the subscripts 1 and 2 correspond respectively to the sampling chamber and the reservoir, S is the pumping speed (in unit of liters/second), D is the diffusion coefficient, n_2 is the number density in the reservoir and it is related to the applied pressure in reservoir P_{sat} through ideal gas law, and ℓ is the average distance traveled by atoms inside the membrane. A' is the effective surface area which is much smaller than the total surface area because of the specific geometry of our experimental method ($A' = \gamma A$, where A is the total surface area and γ is the reduction ratio). By solving (V.2) with initial condition $n_1(0) = 0$, one obtains

$$n_1(t) = \frac{\frac{D\gamma A}{\ell V_1} n_2}{\frac{D\gamma A}{\ell V_1} + \frac{S}{V_1}} \{1 - \exp[- (\frac{D\gamma A}{\ell V_1} + \frac{S}{V_1}) t]\} \quad (V.3).$$

Assuming $\frac{D\gamma A}{V_1 \ell} \ll \frac{S}{V_1}$ (which will be confirmed latter), we obtain the following relation

$$\begin{aligned} P_1(t) &= k_B T n_2 \frac{D\gamma A}{\ell V_1} \frac{1}{\frac{S}{V_1}} [1 - \exp (- \frac{St}{V_1})] \\ &= P_{\text{sat}} [1 - \exp(- \frac{St}{V_1})]. \end{aligned} \quad (V.4)$$

As one can see P_1 will reach the saturation pressure P_{sat} within a time scale determined by the pumping speed. The saturation pressure P_{sat} is related to other parameter as follows

$$\begin{aligned}
 P_{\text{sat}} &= k_B T n_2 \left[\frac{D\dot{Y}A}{\ell v_1} \frac{1}{\frac{S}{v_1}} \right] \\
 &= P_{\text{set}} \left[\frac{DA'}{\ell v_1} \frac{1}{\frac{S}{v_1}} \right] \quad (\text{V.5})
 \end{aligned}$$

Different applied pressures P_{set} in reservoir result in different saturation pressures in the sampling chamber and they are listed in table V.3. By using the equation (V.5) and other known parameters ($A = 8 \times 10^{-6} \text{ m}^2$ and $S/v_1 \approx 30$ seconds, $v_1 = 9.5 \times 10^{-3} \text{ m}^3$), we have determined the quantity $(D\dot{Y})/\ell$ to be $1.62 \pm 0.02 \times 10^{-9} \text{ m/sec}$. The effective surface area is unknown and has to be estimated from the Helium data in the annealed membrane. We will return to this point shortly.

V.3.2 Helium in the annealed $\text{Co}^{3+}(\text{en})_3$ -FHT membrane

When the membrane is annealed the gallery height collapses to 3.82 Å and the gallery spaces are blocked by the dissociated ligands. But since Helium atoms are very small (1.5 Å in diameter), they still access the membrane but with a slower speed and a lower diffusion rate. The saturation time is much longer than the time scale determined from S/v_1 . So the diffusion equation should be modified as follows

$$\frac{v_1 dn_1}{dt} = D [1 - \exp(-t/\tau_0)] \frac{(n_2 - n_1)}{\ell} A' - S n_1 \quad (\text{V.6})$$

where τ_0 is the time to reach a steady flow inside the gallery. The definitions for other parameters are the same as in (V.2). By solving Eq. V.6 with the initial condition $n_1(0) = 0$, we find

$P_{\text{set}}(\text{psi})$	$P_{\text{sat}}(\text{torr})$	τ (sec.)	n_2 ($1/\text{m}^3$)	$(D\gamma)/l$ (mks)
1.91	0.44×10^{-8}	30	0.342×10^{25}	1.64×10^{-9}
3.87	0.86×10^{-8}	30	0.678×10^{25}	1.62×10^{-9}
5.67	1.28×10^{-8}	30	1.016×10^{25}	1.60×10^{-9}
7.54	1.73×10^{-8}	30	1.352×10^{25}	1.63×10^{-9}

Table V.3 Parameters for Helium in unannealed $\text{Co}^{3+}(\text{en})_3\text{-FHT}$ membrane.

$$\begin{aligned}
P_1(t) = & k_B T n_2 \frac{D\bar{Y}}{\ell v_1} \exp \left[- \frac{D\bar{Y}}{\ell v_1} t - \frac{D\bar{Y}}{\ell v_1} \tau_0 \exp\left(-\frac{t}{\tau_0}\right) - \frac{S}{v_1} t \right] \\
& \times \int_0^t \left[1 - \exp\left(-\frac{t'}{\tau_0}\right) \right] \exp \left[\frac{D\bar{Y}}{\ell v_1} t' + \frac{D\bar{Y}}{\ell v_1} \tau_0 \exp\left(-\frac{t'}{\tau_0}\right) + \frac{S}{v_1} t' \right] dt'
\end{aligned}
\tag{V.7}$$

By least squares fitting Eq. (V.7) to our Helium data for different applied pressures P_{set} in the reservoir, we have found $(D\bar{Y})/\ell$ to be $5.5 \pm 0.5 \times 10^{-13}$ m/sec. Other parameters are listed in Table V.4. The fit is shown in figure V.9. The time scale τ_0 is about 1900 seconds which is related to the diffusion coefficient D and distance ℓ as follows

$$\ell^2 \sim D\tau_0 \tag{V.8}$$

We can estimate the diffusion coefficient D from τ_0 with the assumption that $\ell \sim 100 \mu\text{m}$. This is reasonable because the particle sizes are about $10\mu\text{m}$ by $1\mu\text{m}$ and the thickness of the membrane is about $15\mu\text{m}$. Therefore D is estimated to be around 10^{-8} cm^2/sec . Then the surface reduction factor \bar{Y} is estimated to be then about 10^{-5} .

We have obtained the quantity $(D\bar{Y}/\ell = 1.6 \times 10^{-7}$ $\text{cm}/\text{sec})$ for Helium in the unannealed membrane. Assuming the average distance ℓ is also about $100\mu\text{m}$, we have obtained D for helium in unannealed membrane to be $\sim 10^{-4}$ cm^2/sec .

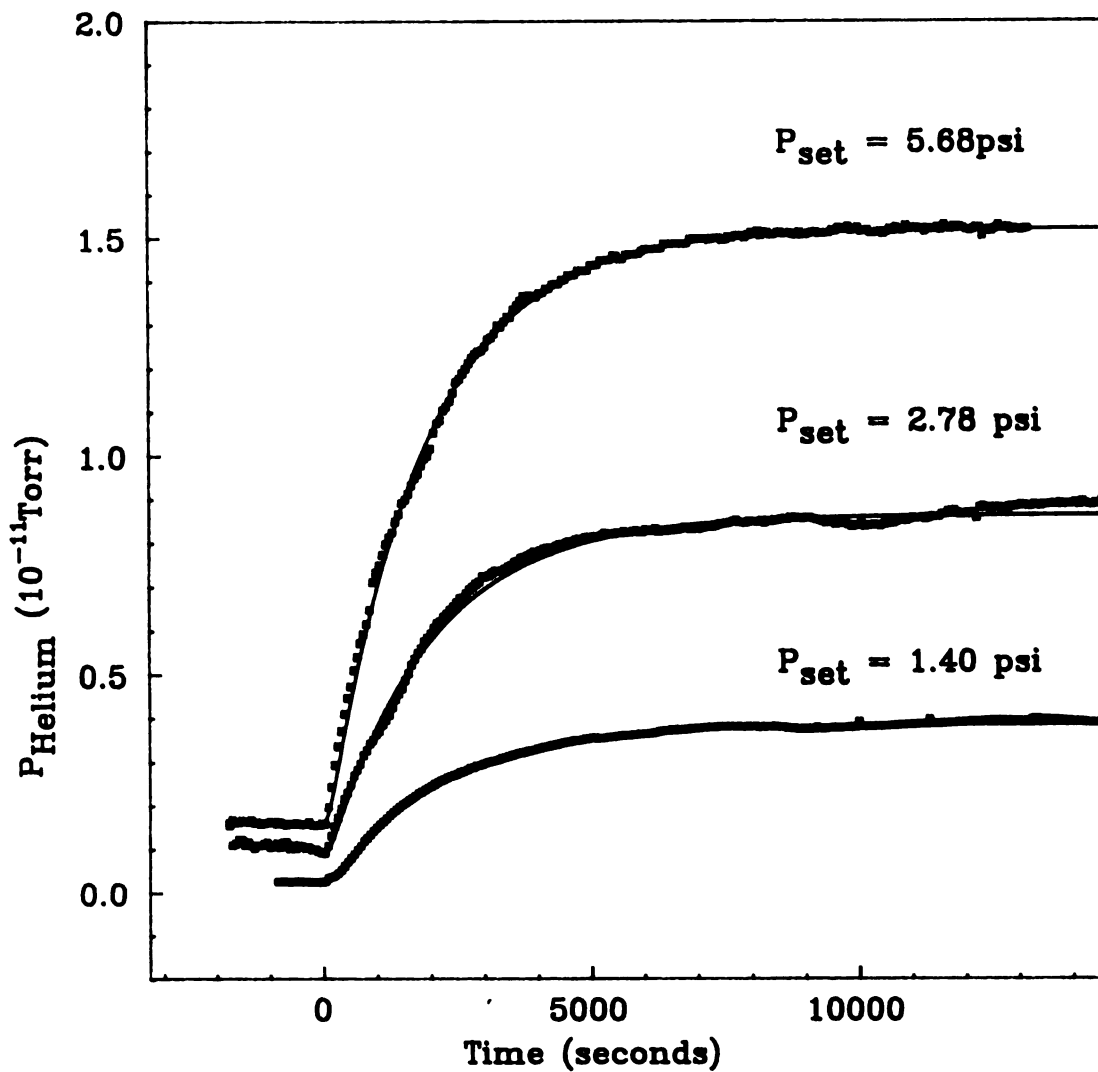


Fig. V.9 Helium partial pressure in the sampling chamber for different applied pressures (turned on at $t=0.0$) when the membrane have been annealed. Solid lines are the fit by Eq. (V.7).

$P_{\text{set}}(\text{psi})$	τ (sec.)	n_2 ($1/\text{m}^3$)	$(D\gamma)/l$ (mks)
1.40	2000	0.25×10^{25}	5.60×10^{-13}
2.78	1900	0.50×10^{25}	5.92×10^{-13}
5.68	1800	1.02×10^{25}	5.12×10^{-13}

Table V.4 Parameters for Helium in annealed $\text{Co}^{3+}(\text{en})_3\text{-FHT}$ membrane.

V.3.3 Argon in the unannealed $\text{Co}^{3+}(\text{en})_3$ -FHT membrane

Since the average dimensions of pathways in the gallery of the unannealed membrane are just slightly larger than the dynamical size of an Argon atom (4.0\AA in diameter), one should expect the same behavior as for Helium in the annealed membrane. Fitting our Argon data to the Eq. (V.7), we have obtained $(D\gamma/l)$ and other parameters for different applied pressures P_{set} in the reservoir. They are listed in Table V.5. The fit is shown in Fig. V.10. By using the same technique used in session V.3.2, we can estimate D and γ to be $10^{-8} \text{ cm}^2/\text{sec}$ and 10^{-5} , respectively.

V.3.4 Argon in the annealed $\text{Co}^{3+}(\text{en})_3$ -FHT membrane

The X-ray diffraction pattern reveals a decrease of the c-axis basal spacing from 14.45\AA to 12.82\AA yields a gallery height that is smaller than the dynamical size of an argon atom. There is no signal of Argon penetrating through the membrane indicating total blockage by the dissociated ligands and the collapsed gallery. This proves that the previous Argon signal seen in the unannealed film is from the void-gallery-void paths. Our observation demonstrates for the first time that Argon atoms actually move in the gallery spaces and can be blocked after the gallery spaces are closed. Essentially, the mass conduction of Argon in the mixed ion system with different x will also pin down the percolation threshold x_c . These have been left as the future work.

All estimated diffusion coefficients are listed in table V.6.

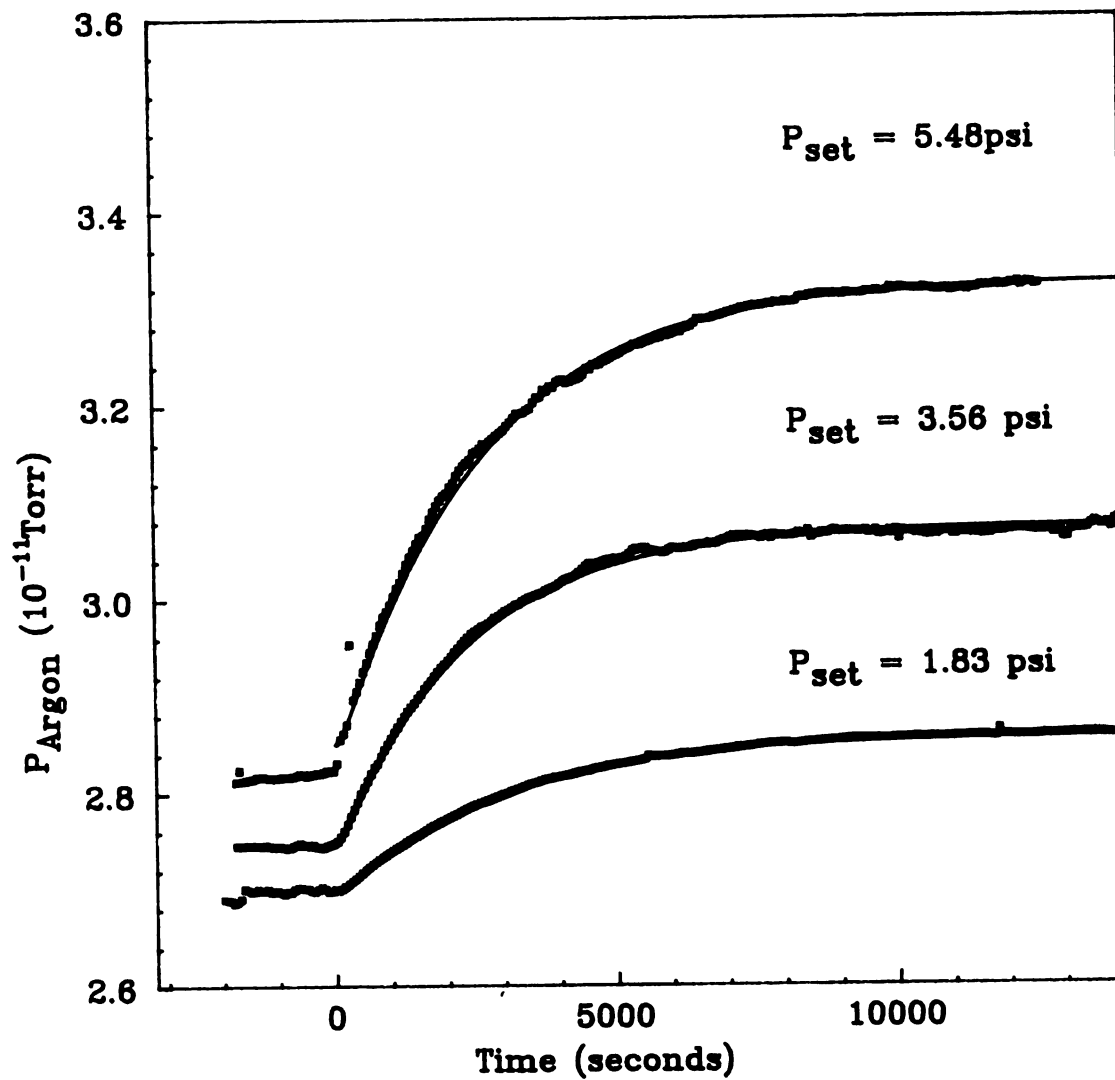


Fig. V.10 Argon partial pressure in the sampling chamber for different applied pressures (turned on at $t=0.0$) before the membrane has been annealed. Solid lines are the fit by Eq. (V.7).

$P_{\text{set}}(\text{psi})$	τ (sec.)	n_2 ($1/\text{m}^3$)	$(D\gamma)/l$ (mks)
1.83	2800	0.326×10^{25}	1.85×10^{-13}
3.65	2300	0.653×10^{25}	1.90×10^{-13}
5.48	2600	0.980×10^{25}	1.86×10^{-13}

Table V.5 Parameters for Argon in unannealed $\text{Co}^{3+}(\text{en})_3\text{-FHT}$ membrane.

	Sample conditions	D (cm²/s)
Helium	Unannealed	10⁻⁴
	Annealed	10⁻⁸
Argon	Unannealed	10⁻⁸
	Annealed	Blocked

**Table V.6 Diffusion coefficients for Helium and Argon
Co³⁺(en)₃-FHT membrane.**

V.4 Concluding Remarks

We have measured the mass conductivity of Helium and Argon in a $\text{Co}^{3+}(\text{en})_3\text{-FHT}$ membrane to demonstrate the dynamical movement of guest species inside the gallery. The annealed film became less permeable to Helium, for which the diffusion coefficient D decreases from $10^{-4} \text{ cm}^2/\text{sec}$ to $10^{-8} \text{ cm}^2/\text{sec}$. Moreover, whereas Argon readily diffuses through the virgin film with D of the order of $10^{-8} \text{ cm}^2/\text{sec}$, the annealed film was impenetrable to Argon atoms. Therefore, We have proved that the observed permeability changes are due to a blockage of pathways by the dissociated ligand and collapsing of the gallery. This constitutes offers the first direct evidence of the movement of Argon and Helium in the gallery spaces for the first time. In absorption measurements, the sudden increase of Argon mass uptake by the ternary intercalated compounds at $x=0.8$ indicating a possible percolation threshold which is consistent with the theoretical simulation⁵¹ based on the physical model of a two dimensional ternary mixed ion system.

Appendix I Divalent Co and Ni ions in an octahedral field
with trigonal distortion

Although the detailed calculation of the energy spectrum of 3d divalent ions in a crystal field with O_h symmetry is available in the literature,⁴⁴ the quantization axis is normally chosen to be along the C_4 axis of the O_h field. However, in our case the trigonal distortion is along the C_3 axis. So it is convenient to choose the distortion direction as the quantization axis. A comprehensive description of the energy spectrum and eigen functions resulting from the O_h field with a distortion along one of its C_3 axis (which is chosen as the quantization direction) is unavailable in the literature. Thus, we have derived all eigenstates and energy spectra by using symmetry arguments and perturbation theory.

Free Co^{2+} and Ni^{2+} ions have ground states of 4F and 3F respectively which have orbital degeneracy of 7. When they are in a crystal field, the Hamiltonian is written as

$$H = -\frac{\hbar^2}{2m} \sum_i \nabla_i^2 - \sum_i \frac{Ze^2}{r_i} + \frac{1}{2} \sum_{i \neq j} \frac{e^2}{r_{ij}} + V_c + \lambda \vec{L} \cdot \vec{S} = H_0 + V_c + \lambda \vec{L} \cdot \vec{S}. \quad (AI.1)$$

H_0 is responsible for the atomic energy spectrum and V_c is the crystal field potential. For first iron series transition metal ions, we treat V_c as a perturbation and spin-orbit coupling as a further perturbation. The Co^{2+} and Ni^{2+} ions will behave as an f electron and the seven degenerate wave functions are Y_3^m , $m=-3, -2, \dots, +3$. In an Octahedral

field they form a reducible representation Γ consisting of several irreducible representations (IR) of O_h . By applying the symmetry operations of O_h group we can obtain the traces of these operations on Γ using the relation $\chi(\Phi) = [\sin(\ell+1/2)\Phi]/\sin(\Phi/2)$, here Φ is the rotation angle of each operation and ℓ is the orbit quantum number ($\ell = 3$). Thus we have

O_h	E	$8C_3$	$3C_2$	$6C_4$	$6C'_2$
$\chi(\Phi)$	7	1	-1	-1	-1

To obtain the IRs of O_h appearing in Γ , we use the relation $n^{(i)} = 1/h \sum_k \chi_k^{(i)} \cdot \chi_k$ where h is the order of the group, i stands for the i^{th} IR, k stands for the k^{th} operation, $\chi_k^{(i)}$ is the character of k operation for i^{th} IR, and χ_k is from the above table. It turns out $\Gamma = T_{1g} + T_{2g} + A_{2g}'$ where T_{1g} and T_{2g} are the two three-dimensional IR of O_h and A_{2g}' is a one-dimensional IR. Furthermore one can obtain the basis functions from Y_3^m for these IRs as follows (Note: the z-axis is along the C_3 axis of the O_h)

$$\begin{aligned}
 T_{1g}: \quad \theta_1 &= \sqrt{5/6} Y_3^2 - \sqrt{1/6} Y_3^{-1} \\
 \theta_2 &= \sqrt{1/6} Y_3^{-1} + \sqrt{5/6} Y_3^{-2}, \\
 \theta_3 &= \sqrt{10}/6 (Y_3^3 - 4/\sqrt{10} Y_3^0 - Y_3^{-3})
 \end{aligned}$$

$$\begin{aligned}
 T_{2g}: \quad \phi_1 &= \sqrt{1/6} Y_3^2 + \sqrt{5/6} Y_3^{-1} \\
 \phi_2 &= -\sqrt{5/6} Y_3^1 + \sqrt{1/6} Y_3^{-2} \\
 \phi_3 &= \sqrt{1/2} (Y_3^3 + Y_3^{-3})
 \end{aligned}$$

$$A_{2g}: \sqrt{2/3} (Y_3^3 + 5/\sqrt{10} Y_3^0 - Y_3^{-3}) \quad (\text{AI.2}).$$

The crystal field V_c can be expanded in terms of spherical harmonics

$$V_c = \sum_{\ell, m} A_{\ell, m} r^\ell Y_\ell^m(\theta, \phi). \quad (\text{AI.3})$$

Since V_c is an even function under the inversion operation, ℓ only equals 0, 2, 4, 6, ... Again by applying the operations of O_h one can obtain the leading terms for the octahedral field

$$V_{O_h} \sim Y_4^0 + \sqrt{10/7} (Y_4^3 - Y_4^{-3}) \quad (\text{AI.4})$$

For holes the crystal field potential is off by just a sign.

We treat a $Ni^{2+} (3d^8)$ ion as a two-hole case and the wave functions in (AI.2) are composed of two individual holes wave functions as follows

$$\begin{aligned} Y_3^3 &= |2^+, 1^+| \\ Y_3^2 &= |2^+, 0^+| \\ Y_3^1 &= \sqrt{3/5} |2^+, -1^+| + \sqrt{2/5} |1^+, 0^+| \\ \text{For } Ni^{2+}: Y_3^0 &= \sqrt{1/5} |2^+, -2^+| + \sqrt{4/5} |1^+, -1^+| \\ Y_3^{-1} &= \sqrt{3/5} |1^+, -2^+| + \sqrt{2/5} |0^+, -1^+| \\ Y_3^{-2} &= |0^+, -2^+| \\ Y_3^{-3} &= |-1^+, -2^+| \end{aligned} \quad (\text{AI.5})$$

where say 2^+ stands for a wave function d_2 with spin up, and $|a^+, b^+|$ stands for the Slater's determinant for two electrons or holes with all spin up. Further operating with S_{\pm} ($S_{\pm} = S_x \pm iS_y$) can reveal all 7X3 wave functions.

We treat a Co^{2+} ($3d^9$) ion as a three-hole case and the wave functions in (A1.2) are composed of three individual hole wave functions as follows

$$\begin{aligned}
 Y_3^3 &= |2^+, 1^+, 0^+| \\
 Y_3^2 &= |2^+, 1^+, -1^+| \\
 Y_3^1 &= \sqrt{2/5}|2^+, 1^+, -2^+| + \sqrt{3/5}|2^+, 0^+, -1^+| \\
 Co^{2+}: Y_3^0 &= \sqrt{4/5}|2^+, 0^+, -2^+| + \sqrt{1/5}|1^+, 0^+, -1^+| \quad (A1.6) \\
 Y_3^{-1} &= \sqrt{2/5}|2^+, -1^+, -2^+| + \sqrt{3/5}|1^+, 0^+, -2^+| \\
 Y_3^{-2} &= |1^+, -1^+, -2^+| \\
 Y_3^{-3} &= |0^+, -1^+, -2^+|.
 \end{aligned}$$

Further operating with S_{\pm} can reveal all 7X4 wave functions.

The matrix elements between two 3d states can be calculated from the C-G coefficients⁵⁵ and it is straight forward

$$\begin{aligned}
 \langle \pm 2 | v_{O_h} | \pm 2 \rangle &= -2/3 Dq \\
 \langle \pm 1 | v_{O_h} | \pm 1 \rangle &= 8/3 Dq \\
 \langle 0 | v_{O_h} | 0 \rangle &= -4 Dq \\
 \langle \pm 2 | v_{O_h} | \mp 2 \rangle &= \langle \mp 2 | v_{O_h} | \pm 2 \rangle = \pm 10/3 \sqrt{2} Dq \quad (A1.7)
 \end{aligned}$$

where Dq is normally defined as $Dq = \text{constant} \frac{1}{7\sqrt{4\pi}} \langle r^4 \rangle$.

Evaluation for the energy levels for Co^{2+} and Ni^{2+} can be carried out by using (AI.2), (AI.5), (AI.6) and (AI.7). The procedure is lengthy but straight forward and the results are as follows

$$\begin{aligned} \text{Ni}^{2+}: & \quad E({}^3A_{2g}) = -12 Dq; \quad E({}^3T_{2g}) = -2 Dq; \quad E({}^3T_{1g}) = +6 Dq \\ \text{Co}^{2+}: & \quad E({}^4T_{1g}) = -6 Dq; \quad E({}^4T_{2g}) = +2 Dq; \quad E({}^4A_{2g}) = +12 Dq. \end{aligned}$$

As we can see the ground state for Ni^{2+} in an O_h field is an orbital singlet (A_{2g}) and the ground state for Co^{2+} is an orbital triplet (T_{1g}). And the energy spectra for Co^{2+} and Ni^{2+} are off by a sign.

When the trigonal distortion along the C_3 axis (z-axis) is turned on, the crystal field becomes $V_c = V_{O_h} + V_\tau$ where $V_\tau = a r^2 Y_2^0$ to first order. Two triplets both break into a doublet and a singlet. To first order, we only need the matrix elements as follows

$$\begin{aligned} \text{Ni}^{2+}: & \quad \begin{aligned} \langle Y_3^{\pm 3} | V_\tau | Y_3^{\pm 3} \rangle &= 5Dt \\ \langle Y_3^{\pm 2} | V_\tau | Y_3^{\pm 2} \rangle &= 0 \\ \langle Y_3^{\pm 1} | V_\tau | Y_3^{\pm 1} \rangle &= -3Dt \\ \langle Y_3^0 | V_\tau | Y_3^0 \rangle &= -4Dt \end{aligned} ; \\ & \quad \text{(AI.8)} \\ \text{Co}^{2+}: & \quad \begin{aligned} \langle Y_3^{\pm 3} | V_\tau | Y_3^{\pm 3} \rangle &= -5Dt \\ \langle Y_3^{\pm 2} | V_\tau | Y_3^{\pm 2} \rangle &= 0 \\ \langle Y_3^{\pm 1} | V_\tau | Y_3^{\pm 1} \rangle &= 3Dt \\ \langle Y_3^0 | V_\tau | Y_3^0 \rangle &= 4Dt \end{aligned} \end{aligned}$$

which can be obtained by using (AI.5), (AI.6), and the proper C-G coefficients. Dt is defined as $Dt = \text{constant} \langle r^2 \rangle$. The energy

splitting can be evaluated by calculating the expectation value of $ar^2 Y_2^0$ and results are as follows:

$$\text{Ni}^{2+}: \quad T_{1g} \begin{vmatrix} 6Dq + Dt & (1) \\ 6Dq - 1/2 Dt & (2) \end{vmatrix}; \quad T_{2g} \begin{vmatrix} -2Dq + 5Dt & (1) \\ -2Dq - 5/2Dt & (2) \end{vmatrix}; \quad A_{2g} \quad -12Dq \quad (1)$$

$$\text{Co}^{2+}: \quad A_{2g} \quad 12Dq \quad (1); \quad T_{2g} \begin{vmatrix} 2Dq + 5/2 Dt & (2) \\ 2Dq - 5 Dt & (1) \end{vmatrix}; \quad T_{1g} \begin{vmatrix} 6Dq + 1/2 Dt & (2) \\ 6Dq - Dt & (1) \end{vmatrix}$$

where the numbers in parenthesis indicate the degeneracy. The energy spectrum is shown in Fig. AI.1. The corresponding wave functions are still the functions in (AI.1). θ_1 and θ_2 are for the doublet of T_{1g} and θ_3 is the singlet. ϕ_1 and ϕ_2 are for the doublet of T_{2g} and ϕ_3 is the singlet. As can be seen, the ground state of a Co^{2+} ion is an orbital singlet (θ_3) when the trigonal distortion is turned on.

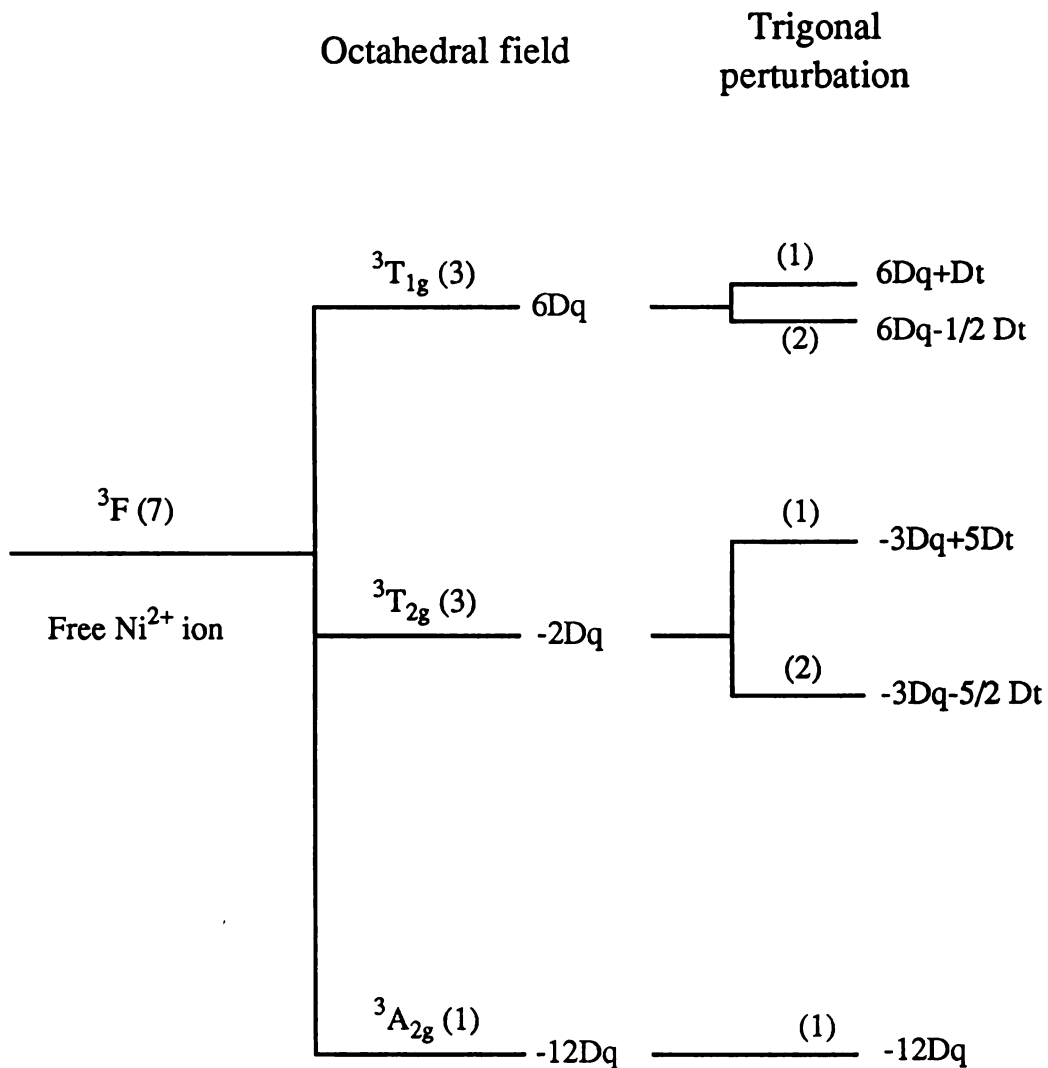


Figure AI.1 Energy splitting of a Ni^{2+} ion in an octahedral field with a trigonal perturbation. Numbers in parenthesis present orbital degeneracy. For a Co^{2+} ion, the spectrum is off by a sign and the spin degeneracy becomes 4.

Appendix II Divalent Cu in an octahedral field
with trigonal distortion

A free Cu^{2+} ion has electronic structure of $3d^9$ and a ground state of 2D which has an orbital degeneracy of 5. It behaves as a d hole and the five degenerate wave functions are Y_2^m , $m=-2, \dots, +2$ (normally denoted as d_m). In an O_h field these wave functions form a reducible representation Γ consisting several irreducible representations of O_h . The energy splitting for a d hole in an O_h field is the most common example given in crystal field theory literatures.⁴⁴ Γ splits into a doublet called e_g and a triplet called t_{2g} . Here we use lower case since we deal with a single hole. The energies for each levels are: $E(e_g) = -6Dq$; $E(t_{2g}) = 4Dq$, here Dq is defined exactly the same as in Appendix I. And the basis wave functions are as follows (assigning the C_3 axis as the z-axis)

$$\begin{aligned}
 t_{2g}^+ &= \sqrt{2/3} d(x^2-y^2) - \sqrt{1/3} d(xz) \\
 t_{2g}^- &= \sqrt{2/3} d(xy) + \sqrt{1/3} d(yz) \quad ; \\
 t_{2g}^0 &= d(z^2)
 \end{aligned}
 \tag{AII.1}$$

$$\begin{aligned}
 e_g^+ &= \sqrt{1/3} d(x^2-y^2) + \sqrt{2/3} d(xz) \\
 e_g^- &= \sqrt{2/3} d(xy) + \sqrt{1/3} d(yz)
 \end{aligned}$$

where $d(x^2-y^2) = 1/\sqrt{2} (d_2+d_{-2})$, $d(z^2) = d_0$, $d(xy) = 1/(i\sqrt{2}) (d_2-d_{-2})$, $d(xz) = -1/\sqrt{2} (d_1-d_{-1})$, and $d(yz) = -1/(i\sqrt{2}) (d_1+d_{-1})$.

The ground state of a Cu^{2+} is an orbital doublet (e_g). When there is a trigonal distortion along the C_3 axis, the crystal field is changed by a term V_τ ($V_\tau = -ar^2Y_2^0$). Useful matrix elements are

$$\begin{aligned} \langle t_{2g}^\pm | V_\tau | t_{2g}^\pm \rangle &= Dt \\ \langle t_{2g}^0 | V_\tau | t_{2g}^0 \rangle &= -2Dt \\ \langle e_g^\pm | V_\tau | e_g^\pm \rangle &= 0 \\ \langle t_{2g}^\pm | V_\tau | e_g^\pm \rangle &= \sqrt{2} Dt \end{aligned} \quad (\text{AII.2})$$

As we can see, the trigonal perturbation mixes t_{2g}^\pm and e_g^\pm . By solving the 5X5 secular equation, one can obtain the new energy eigenvalues and eigenstates (in parenthesis)

$$E(t_{2g}) = \begin{cases} 4Dq + Dt + 2Dt^2/(5Dq); & (A t_{2g}^\pm + B e_g^\pm) \\ 4Dq - 2Dt; & (t_{2g}^0) \end{cases} \quad (\text{AII.3})$$

$$E(e_g) = -6Dq - 2Dt^2/(5Dq); \quad (-B t_{2g}^\pm + A e_g^\pm)$$

where $A \approx 1 - Dt^2/(100Dq^2)$, $B \approx \sqrt{2} Dt/(10Dq)$. The perturbed levels are plotted in Fig. AII.1. The most important feature is that the ground state energy is down shifted but its orbital degeneracy is not removed.

Spin degeneracy can be added to the wave function sets by multiplying the spin eigen functions α and β , where α is for spin up and β is for spin down. So the total degeneracy of the ground state is four and we can rewrite it as

$$c_1 d(x^2 - y^2)\alpha + c_2 d(xz)\alpha$$

$$\begin{aligned}
 c_1 d(x^2-y^2)B + c_2 d(xz)B & \quad \text{(AII.4)} \\
 c_1 d(xy)A - c_2 d(yz)A \\
 c_1 d(xy)B - c_2 d(yz)B
 \end{aligned}$$

where $c_1 = \sqrt{1/3} A - \sqrt{2/3} B$, and $c_2 = \sqrt{2/3} A + \sqrt{1/3} B$. By evaluating the matrix elements for $\lambda \vec{l} \cdot \vec{s}$, one can easily show that all matrix elements are equal to zero (see appendix II in chapter 6 of ref.44). Therefore, the spin-orbit coupling can not lift the degeneracy of the ground state.

It is straight forward to evaluate to expectation value of the g factor operator $(\vec{l} + 2\vec{s})$ and obtain the g factor to be exactly 2 for the degenerate ground state.

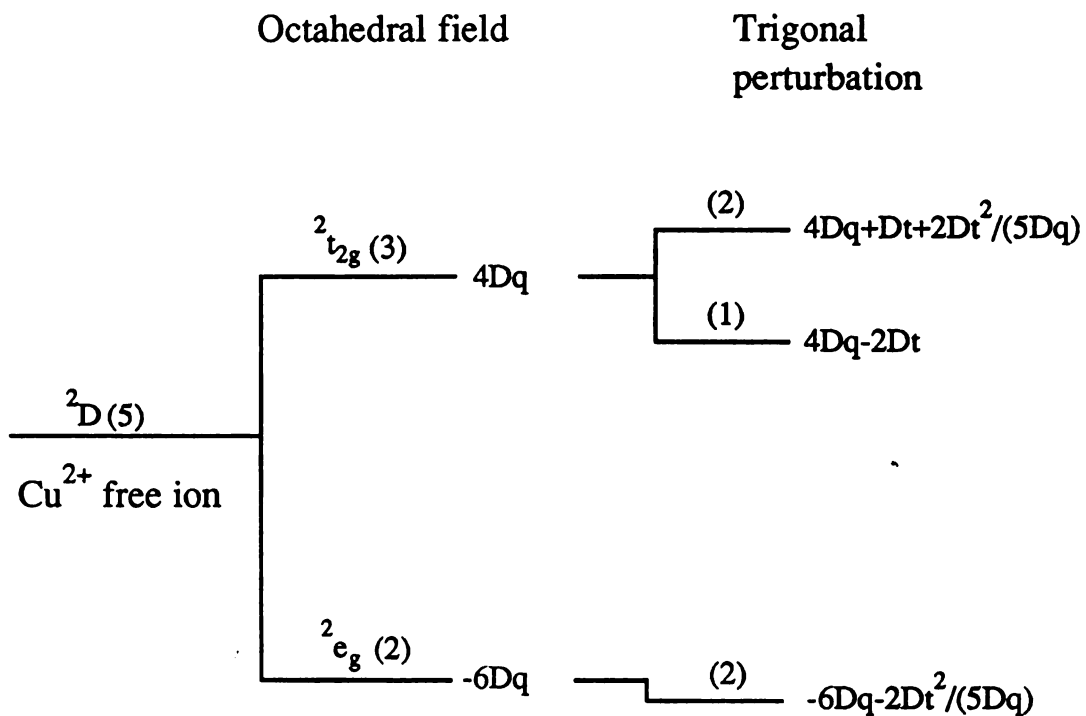


Figure AII.1 Energy splitting of a Cu^{2+} ion in an octahedral field with trigonal perturbation. Numerals in parenthesis present the orbital degeneracy of each state.

REFERENCE

1. M.S. Whittingham, Intercalation Chemistry (Academic Press, NY 1982), p1.
2. K. Watanake, et.al., Proc.R.Soc.Lond., A333, 51
3. See Solid State Batteries, ed. by A.C. Sequeira and A. Hooper (Marinas Nighoff Publishes, Dordrecht, 1985)
4. P.B. Weisz, Science, 179, 433 (1973)
5. D. Gelbin, AIChE J, 25, 358 (1979)
6. S. Lee, X-ray studies of layered rigidity and c-axis expansion in clay intercalated layered compounds, Ph.D thesis, p2
7. K. Norrish, Trans. Faraday Soc. 18, 120 (1954)
8. S.A. Solin, Adv.Chem.Phys., 455, (1982)
9. M. Suzuki, H. Ikeda, J.Phys.C, Solid State Phys., 14, L923 (1981)
10. J.T. Nicholls, G. Dresslhaus, Synthetic Metals., 34, 519 (1989)
11. D.G. Wiesler, H. Zabel, Synthetic Metals, 34, 505 (1989)
12. J. Rogerie, et.al., Synthetic Metals, 34, 513 (1989)
13. M. Suzuki, N. Wada, D.R. Hines, M.S. Whittingham, Phys.Rev. B36, 2844 (1987)
14. H. van Olphen, J. Colloid Sci., 20, 822 (1965)
15. See Magnetism, ed. by G.T. Rado and H. Suhl, vol IV, (Academic Press Inc., NY 1965), p1
16. D.H. Martin, Magnetism in Solids, (The MIT Press, 1967), p238
17. C. Zener, Phys. Rev. 81, 440 (1951); *ibid.* 82, 403 (1951); *ibid.* 83, 299 (1951)
18. T. Kasuya, Progr. Theoret. Phys. (Kyoto) 16, 45 (1965); *ibid.* 16, 58 (1956)
19. T. Kasuya, J. Res. Develop. (IBM), 214, May 1970

20. H.A. Kramers, *Physica*, 1, 182 (1934)
21. P.W. Anderson, *Phys. Rev.* 79, 150 (1950)
22. P.W. Anderson, *Phys. Rev.* 115, 2 (1959)
23. J.M.Kosterlitz, D.j. Thouless, *J.Phys.C, Solid State Phys.* 6, 1181 (1973)
24. H.J. Zeiger, G.W. Pratt, *Magnetic intercalations in solids* (Clarendon Press, Oxford 1973), p138
25. I.J.Dzyaloshinski, *J. Phys.Chem.Solids*, 4, 241 (1958)
26. T. Moriya, *Phys. Rev.*, 120, 91 (1960)
27. See *Clay Mineralogy*, 2nd ed., R.E. Grim (McGraw-Hill Book, 1968)
28. S.W. Bailey, *Am. Miner.* 60, 175 (1975)
29. See *Crystal structures of clay minerals and their x-ray identification* by G.W. Brindley and G. Brown (Mineralogical Society, London 1980), p98
30. M. Suzuki, et.al., *Phys. Rev. B* 40, 11229, (1989). Note: The ac susceptibility of Ni-ver also shows a shoulder at 2.2K and a sharp peak at 2.9K indicating possible magnetic phase transitions at these temperatures. See N. Wada et al., *J. Mater. Science*, 2, 864, (1987).
31. J.A. Rausell-Colom, et.al., *Clay Miner.*, 15, 37 (1980)
32. N.W. Ashcroft, N.D. Mermin, *Solid states Phys.* (Saunders College, Philadelphia 1976), p56
33. W. Low, *Paramagnetic rasonance in solids* (Academic Press Inc., NY 1960), p113
34. C.K. Jorgensen, *Inst. Intern. Chim, Solvay, Conseil Chim.*, Brussels, 1956
35. B. Bleaney, K.D. Bowers, *Proc. Phys. Soc. (London)*, A65, 667 (1952)

36. J.H. Van Vleck, *J.Chem, Phys*, 3, 807 (1935)
37. S.B. Hendricks, M.E. Jefferson, *Am. Miner.* 23, 851 (1938)
38. A.M. Mathieson, G.F. Walker, *Am. Miner.*, 39, 231 (1954)
39. A. Grudemo, *Handl. Svensk. Forskn. Inst. Cement.*, 22, (1954)
40. A.M. Mathieson, *Am. Miner.*, 43, 216 (1958)
41. H. Shirozu, S.W. Bailey, *Am. Miner.*, 51, 1124 (1966)
42. de la Calle, et.al., *Clays and Clay Miner.*, 36, 481 (1988)
43. W.F. Bleam, *Clays and Clay Miner.*, 38, 527 (1990)
44. Ballhausen, *Introduction to ligand field theory* (McGraw-Hill Inc., NY 1960), Chapter 4
45. J. Yamashita, *J. Phys. Soc. Japan*, 9, 339 (1954)
46. J. Yamashita, *Progr. Theort. Phys. (Kyoto)*, 12, 808 (1954)
47. N.D. Mermin, H. Wagner, *Phys. Rev. Lett.*, 17, 1133 (1966)
48. L. Onsager, *Phys. Rev.* 65, 117 (1944)
49. B. Kanfmann, *Phys. Rev.* 76, 1132 (1949)
50. R.M. Barrer, D.L. Jones, *J. Chem. Soc. (A), Inorg. therot*, 1531 (1970)
51. Z.X. Cai, S.D. Mahanti (unpublised).
52. J.A. Cowen, G.T. Johnson, *J. Chem Phys.*, 44, 2217 (1966)
53. H.A. Bethe, *Z. Physik*, 71, 205 (1931)
54. R.Kim, T.J.Pinnavia, to be published.
55. Bivins, et.al., *The 3-j and 6-j symbols*, MIT Press.
56. P.G. de Gennes, *La Recherche*, 7, 919, (1976).

LIST OF PUBLICATIONS

Dynamics of exciton transfer between the bound and the continuum states in GaAs-Al_xGa_{1-x}As multiple quantum wells

H. X. Jiang, E. X. Ping, P. Zhou,* and J. Y. Lin

Department of Physics, Cardwell Hall, Kansas State University, Manhattan, Kansas 66506-2601

(Received 2 January 1990; revised manuscript received 21 May 1990)

Experimentally observed two-exponential decay of excitonic transitions in GaAs-Al_xGa_{1-x}As multiple quantum wells has been successfully interpreted in terms of the exciton transfer between the continuum (free carriers) and the bound states. The calculation results obtained from this exciton-transfer model are in excellent agreement with experimental observations. The rates of the exciton transfer and the free-carrier recombination have been obtained. We have demonstrated that the emission-energy dependence of the decay time constant of the slower decay component is caused by the variation in exciton binding energy induced by interface roughness in the quantum wells.

Optical properties of semiconductor quantum wells (QW's) and superlattices (SL's) have been intensively investigated during the past few years because of their novel properties.¹⁻³ The decay of excitonic transitions in QW's was found to show exactly two-exponential behavior.⁴⁻⁶ Nevertheless, the physical origin of this two-exponential decay and the dynamic processes of excitons in QW's are not yet well understood. In this paper, the origin of the two-exponential decay of excitonic transition in a QW has been studied by using time-resolved photoluminescence. We demonstrate that the origin of the two-exponential decay of excitonic transitions in QW's is caused by exciton transfer between the bound and the continuum states (free carriers) via acoustic phonon-exciton (phonon-free carriers) interaction.

The sample used for this study was a GaAs-Al_{0.5}Ga_{0.5}As MQW which was grown by molecular-beam epitaxy on a GaAs(100) substrate without growth interruption. It consists of alternate 250-Å well layers and 278-Å Al_{0.5}Ga_{0.5}As barrier layers with a total of ten periods. Experimental details have been described previously.⁶

Figure 1 shows a semilogarithmic plot of temporal responses of photoluminescence of a GaAs-Al_{0.5}Ga_{0.5}As MQW measured at three representative emission energies around the heavy-hole exciton transition peak. The inset shows the time-integrated emission spectrum with heavy-hole and light-hole exciton luminescence peaks at 1.5253 and 1.5297 eV, respectively. These values are consistent with those calculated by using the transfer-matrix method with the conduction-band offset parameter being 0.65 and the binding energies of heavy- and light-hole excitons being 5.8 and 6.2 meV, respectively.⁷ The shoulder at about 1 meV below the heavy-hole exciton peak is due to either impurity-bound exciton or biexciton transitions.^{8,9} It is known that the exciton emission linewidth is predominantly caused by interface roughness.¹⁰ Therefore, luminescence signals measured in the vicinity of the exciton transition peak correspond to exciton recombination occurring in different QW domains.^{4,10} In Fig. 1, the nonexponential decay of photoluminescence is clearly observed with

different decay rates occurring at different emission energies.

Figure 2 plots the luminescence as a function of delay time t_d measured at the heavy-hole exciton transition peak. The rise part of the luminescence is not shown here and $t_d=0$ has been chosen at the peak position in the luminescence temporal responses of Fig. 1. Crosses show the measured values while the dashed and solid lines are fittings using one- and two-exponential decay, respectively. From Fig. 2, it is clear that the decay of the heavy-hole excitons cannot be described by a single-exponential

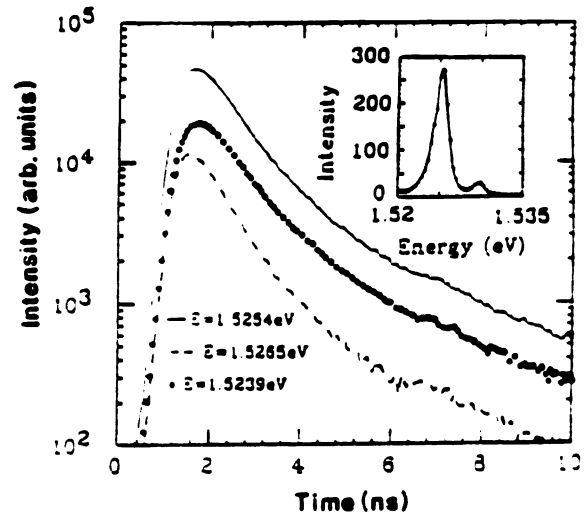


FIG. 1. Semilogarithmic plot of photoluminescence intensity vs delay time for three representative emission energies around the heavy-hole exciton transition peak of a GaAs-Ga_{0.5}Al_{0.5}As multiple quantum well. Well and barrier thicknesses are 250 and 278 Å, respectively. The excitation energy was 2.125 eV with an average power density of 0.2 W/cm². The inset shows the low-temperature (8.5 K) time-integrated photoluminescence emission spectrum showing the heavy- and light-hole exciton emission bands.

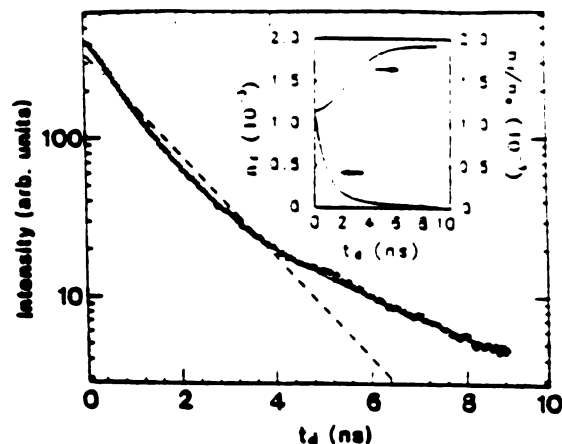


FIG. 2. Luminescence as a function of delay time t_d measured at the heavy-hole exciton transition peak. Crosses show the measured values while the dashed and solid lines are fittings using one- and two-exponential decay, respectively. $t_d=0$ has been chosen at the peak position in the luminescence temporal response of Fig. 1. The inset shows the relative free carrier population n_f and the ratio of n_f to the exciton population n_e as functions of delay time t_d . n_f+n_e has been normalized to unity at $t_d=0$.

form. However, the two-exponential decay fits perfectly with the experimental data. Therefore, in general, the decay of the heavy-hole exciton transition in QW can be written as

$$I(t) = A \exp(-t/\tau_1) + B \exp(-t/\tau_2), \quad (1)$$

where τ_1 and τ_2 are the two decay time constants representing faster and slower decay components and are about 0.9 and 4.2 ns measured at the heavy-hole exciton transition peak, respectively. Furthermore, decays of the exciton recombination in entire heavy- and light-hole exciton emission bands are also exactly two exponential. We have obtained the two decay time constants as functions of emission energies in the heavy-hole exciton emission band shown in Fig. 3. We see that τ_1 to be shown mainly due to the radiative decay of excitons depends only weakly on the emission energies. In contrast, τ_2 depends strongly on the emission energies and decreases monotonically with increase of emission energy from 6.4 ns at 1.5232 eV to about 2.2 ns at an energy of 1.5268 eV. We want to indicate here that the time constants of the slow decay component at the lower-energy side are even larger than the exciton lifetime in the bulk GaAs (3.3 ns).¹¹

It is known that at room temperatures, optical nonlinearities in absorption spectra of GaAs-Al_xGa_{1-x}As multiple and single quantum well structure under high laser excitation intensity is due to the ionization of excitons after their creation,^{12,13} and the transfer between the bound and the continuum states becomes important.¹⁴ The excited states of excitons (including the continuum states corresponding to the ionization threshold of excitons) in QW's have also been observed at low temperatures under low laser intensity excitation.^{13,16} In this Rapid Communication, we interpret that even at low tem-

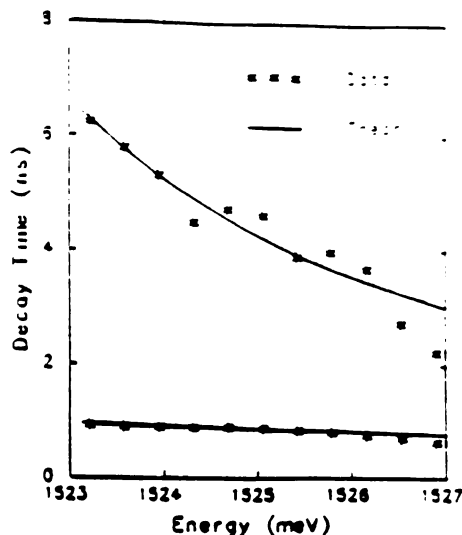


FIG. 3. Decay time constants of photoluminescence vs emission energies in the emission band of the heavy-hole exciton luminescence. The asterisks represent the experimental measured τ_1 (lower values) and τ_2 (higher values). The solid line of τ_1 is a least-squares fitting (see text). The solid line for τ_2 is the calculation results.

peratures excitons are not only occupying the bound states of lowest energies, but also higher dissociated states (ionized excitons or free carriers) due to thermal ionization. Here, we concentrate on the behavior of the free exciton decay after $t_d=0$, which is about 500 ps after laser excitation. It is known that hot carriers initially generated by above band-gap excitation relax to the bottom of the sub-band and thermally distributed to generate excitons within about 200 ps at 1.8 K,¹⁷ and thus our system is in thermal equilibrium at $t_d=0$. Under the above consideration, the rate equations for the exciton populations in the bound and the continuum states at delay time $t_d > 0$ can be written as

$$\frac{dn_e}{dt} = -\gamma_e n_e - U n_e + D n_f, \quad (2)$$

$$\frac{dn_f}{dt} = -\gamma_f n_f - D n_f + U n_e,$$

where n_e and n_f denote, respectively, the exciton population in the bound state (1S ground state) and the free-carrier population in the conduction band. γ_e and γ_f are the recombination rates of excitons and free carriers. $U(D)$ is the rate of exciton transfer from the bound (continuum) to the continuum (bound) states. In writing Eq. (2), we have included all other excited states into continuum states since experimentally observed transition from excited 2S exciton state is corresponding to the continuum edge and the transfer time of the continuum to excited states is expected to be negligible. Effect due to impurity-bound excitons or biexcitons have been neglected since their populations are very small in our case. The solution of Eq. (2) is an exact two-exponential form of Eq.

(1) with

$$\tau_{1,2}^{-1} = \frac{1}{2} \{ \gamma_e + \gamma_f + D + U \pm [(\gamma_e + U - \gamma_f - D)^2 + 4DU]^{1/2} \}. \quad (3)$$

In order to compare with experimental results, we need to know two more quantities among four unknowns, γ_e , γ_f , U , and D . Exciton transfer rates U and D can be calculated by using quantum theory and consider that the exciton transfer process is assisted by emission or absorption of acoustic phonons. D and U thus can be written as

$$D = (2\pi/\hbar) \sum_{k_1} \sum_{k_2} \sum_q |M|^2 f(k_1) [n(q) + 1] \times \delta(k_1 - k_2 - q) \delta(E_1 - E_2 - \hbar\omega), \quad (4)$$

$$U = (2\pi/\hbar) \sum_{k_1} \sum_{k_2} \sum_q |M|^2 f(k_2) n(q) \times \delta(k_2 - k_1 + q) \delta(E_2 - E_1 + \hbar\omega).$$

Here M is the matrix element depending on the interaction, $n(q) = \{\exp(\hbar\omega(q)/kT - 1)\}^{-1}$ is the probability of finding an acoustic phonon of wave vector q at temperature T , and $f(k_i)$ the probability of the initial exciton state being occupied has been assumed to be a Boltzmann distribution. E_1 and E_2 are the exciton energy and k_1 and k_2 are the two-dimensional wave vectors of excitons in the plane perpendicular to the growth x axis in the initial and final states, respectively. Here the bound state presents initial (final) state for $U(D)$. The detailed calculation procedure will be published in a forthcoming paper.¹⁸ However, an important result obtained is that D and U are related by the following expression:

$$D = U \exp(\Delta E/kT), \quad (5)$$

where ΔE is the energy difference between the continuum and the bound states, which is the binding energy of exciton E_b . With an approximation of the matrix element M being a constant and independent of k_i ($i=1,2$), from Eqs. (3)–(5), we can calculate τ_1 and τ_2 .

The key factor which causes τ_2 to be strongly dependent on emission energy is the emission-energy dependence of the exciton binding energy $\Delta E (=E_b)$ as a result of interface roughness. The observed exciton emission linewidth corresponds to a well width fluctuation of about 20 Å at 250 Å, we therefore use an approximation of a linear relation for E_b as a function of well thickness L , $E_b(L) = E_b(L_0) - \alpha(L - L_0)$, where $L_0 = 250$ Å is the average well thickness and α is about 0.012 meV/Å in this region of L .¹⁹ We also use an expression, $\tau_1 = \tau_0 - \beta(L - L_0)$, to account for the changing of the radiative recombination rate with L , where $\beta = 3.08 \times 10^{-3}$ ns/Å and $\tau_0 = 0.85$ ns, which are consistent with those deduced from the exciton transition peak position shift with delay time.⁹ However, taking τ_1 as a constant will not alter the behavior of τ_2 . Strong dependence of τ_2 on emission energies is a direct consequence that the transfer rates D and

U are functions of exciton binding energies, E_b , which depend on emission energies as a result of interface roughness. The recombination rate of free carriers (exciton in the continuum states) γ_f is assumed to be independent of well thickness in this region. τ_2 as a function of emission energy has been calculated and the result is plotted as a solid line in Fig. 3, which is in good agreement with experimental data. The best fitting between experimental data and calculation yields $\gamma_f^{-1} = 20$ ns consistent with the value obtained previously²⁰ and the matrix element $M = 1.39 \times 10^{-9}$ meV. Based on these results, the physical origin of the two exponential decays have been completely resolved. The fast decay rate is mainly due to the radiative recombination of excitons. The slow decay component is determined by the recombination rate of free carriers and the rates of exciton transfer between the bound and the continuum states.

At $L = 250$ Å, the transfer rates U and D are 7.52×10^4 and 2.06×10^8 s⁻¹, respectively. Although the transfer rate of D is 3 orders of magnitude larger than that of U , the absolute numbers of excitons transferred between the bound (continuum) and the continuum (bound) states are compatible, since the population of excitons in the bound state (n_b) is about 3 orders of magnitude larger than those in the continuum state (n_f) in our case, as shown in the inset of Fig. 2. In the inset of Fig. 2, we plot the variations of n_f and n_f/n_b as functions of delay time t_d . Here, $n_b + n_f$ has been normalized to unity at $t_d = 0$. We see that the relative population of excitons in the continuum state (free carriers) increases with the increase of t_d . This is caused by the fact that the transfer rates U and D , as well as the free-carrier recombination rate, are much smaller than the exciton radiative recombination rate in the bound state, which also leaves τ_1 being hardly affected by the exciton transfer between the bound and the continuum states. Another point we want to indicate is that the population of excitons in the bound and the continuum states are in thermal equilibrium only at $t_d = 0$ due to the transfer rate being smaller than the radiative decay rate in the bound state. The discrepancy between the calculated and experimental results of τ_2 in the high-energy side of Fig. 3 is caused by the luminescence intensity overlap between the heavy- and light-hole exciton transitions. The absence of the transition line from the free carriers, especially at high temperatures, may be due to the free carrier recombination rate being much smaller than the transfer rate D , yet remains to be investigated.

In conclusion, the origin of two-exponential decay of excitonic transition in GaAs-Al_{0.2}Ga_{0.8}As MQW's has been investigated. Our results demonstrate that the two-exponential decay of exciton transition is a direct consequence of the exciton transfer between the bound and continuum states (free carriers) via acoustic phonon-exciton (phonon-free carriers) interaction. The recombination rate of free carriers as well as exciton transfer rates are obtained.

- *Present address: Department of Physics and Astronomy and Center for Fundamental Materials Research, Michigan State University, East Lansing, MI 48824-1116.
- ¹L. Esaki, *J. Phys. (Paris) Colloq.* **48**, C5-1 (1987).
 - ²R. C. Miller, D. A. Kleinman, W. A. Nordland, and A. C. Gosard, *Phys. Rev. B* **22**, 868 (1980).
 - ³J. Feldman, G. Peter, E. O. Gobel, P. Dawson, K. Moore, C. Foxon, and R. J. Elliott, *Phys. Rev. Lett.* **59**, 2337 (1987).
 - ⁴J. Christen, D. Bimberg, A. Steckenborn, and G. Weimann, *Appl. Phys. Lett.* **44**, 84 (1984).
 - ⁵M. Kohl, D. Heitmann, S. Tarucha, K. Lee, and K. Ploog, *Phys. Rev. B* **39**, 7736 (1989).
 - ⁶P. Zhou, H. X. Jiang, R. Banwart, S. A. Solin, and G. Bai, *Phys. Rev. B* **40**, 11862 (1989).
 - ⁷H. X. Jiang and J. Y. Lin, *J. Appl. Phys.* **61**, 624 (1987).
 - ⁸R. C. Miller, D. A. Kleinman, A. C. Gosard, and O. Mustmann, *Phys. Rev. B* **25**, 6545 (1982).
 - ⁹S. Charbonneau, T. Steiner, M. L. W. Thewalt, E. S. Doteles, J. Y. Chi, and B. Elman, *Phys. Rev. B* **38**, 3583 (1988).
 - ¹⁰C. Weinbuch, R. Dingle, A. C. Gosard, and W. Wiegman, *Solid State Commun.* **38**, 709 (1981).
 - ¹¹G. W. Hooft, W. A. J. A. Van der Poel, L. W. Molenkamp, and C. T. Foxon, *Phys. Rev. B* **35**, 8281 (1987).
 - ¹²W. H. Knox, R. L. Fork, M. C. Downer, D. A. B. Miller, D. S. Chemla, C. V. Shank, A. C. Gosard, and W. Wiegman, *Phys. Rev. Lett.* **54**, 1306 (1985).
 - ¹³D. A. B. Miller, D. S. Chemla, D. J. Eilenberger, P. W. Smith, A. C. Gosard, and W. T. Tsang, *Appl. Phys. Lett.* **41**, 679 (1982).
 - ¹⁴W. Pickin and J. P. R. David, *Appl. Phys. Lett.* **56**, 368 (1990).
 - ¹⁵R. C. Miller, D. A. Kleinman, W. T. Tsang, and A. C. Gosard, *Phys. Rev. B* **24**, 1134 (1981).
 - ¹⁶P. Dawson, K. J. Moore, G. Duggan, H. I. Ralph, and C. T. B. Foxon, *Phys. Rev. B* **34**, 6007 (1986).
 - ¹⁷J. Kasano, Y. Segawa, Y. Aoyagi, and S. Namba, *Phys. Rev. B* **40**, 1685 (1989).
 - ¹⁸E. X. Ping and H. X. Jiang (unpublished).
 - ¹⁹T. F. Jiang, *Solid State Commun.* **98**, 589 (1984).
 - ²⁰S. Schmitt-Rink, D. S. Chemla, and D. A. Miller, *Phys. Rev. B* **32**, 6601 (1985).

Excitonic transitions in GaAs-Al_xGa_{1-x}As multiple quantum wells affected by interface roughness

P. Zhou

Center for Fundamental Materials Research and Department of Physics and Astronomy, Michigan State University, East Lansing, Michigan 48824-1115

H. X. Jiang

*Department of Physics, Cardwell Hall, Kansas State University, Manhattan, Kansas 66506
and Center for Fundamental Materials Research, Michigan State University, East Lansing, Michigan 48824-1116*

R. Bannwart* and S. A. Solin

Center for Fundamental Materials Research and Department of Physics and Astronomy, Michigan State University, East Lansing, Michigan 48824-1116

G. Bai

Division of Engineering and Applied Science, California Institute of Technology, Pasadena, California 91125

(Received 19 April 1989; revised manuscript received 31 July 1989)

Time-resolved photoluminescence has been used to study the effects of interface roughness on excitonic transitions in GaAs-Al_xGa_{1-x}As multiple quantum wells. In addition to the luminescence linewidth broadening and Stokes red shift, the interface roughness also strongly affects the dynamic process of optical transitions so that the excitonic transition peak shifts with delay time. However, the heavy-hole exciton transition has red shifts at short delay times and exhibits a turnover at longer delay times. A maximum shift of about 0.1 meV at a delay time of 4 ns was obtained. We have demonstrated that the peak shift is caused by interface roughness in the quantum wells. Furthermore, the decay of the excitonic transition is found to fit a two-exponential form. Based on a model involving interface roughness and two-exponential decay, we calculated the position of the excitonic transition peak as a function of delay time. Our calculations are consistent with experimental results.

I. INTRODUCTION

Recently, quantum-well (QW) and superlattice (SL) structures have attracted a great deal of attention because of their novel properties.¹⁻⁴ Since the proposal of these exciting new structures,^{5,6} they have been studied extensively, and thus many important features have been discovered. For fundamental physics, quantum-well and superlattice structures have been used to explore the physical properties of a whole new field of low-dimensional systems and quantum effects. Many novel phenomena in the quantum regime have been discovered, such as resonant tunneling of double-barrier quantum wells with negative differential resistance.^{7,8} By separating the impurities with charge carriers by modulation doping, a significant mobility enhancement in GaAs-Al_xGa_{1-x}As quantum wells has been achieved.^{9,10} Applications of these quantum wells and superlattices include high-speed electronics, optoelectronics and photonic devices, such as quantum-well lasers,^{11,12} modulation-doped field-effect transistors¹³ (MODFET), photodetectors,¹⁴ etc.

Although much work has been done in this field, there are only a few investigations that concentrate on the dy-

namic processes of excitonic transitions in QW and SL. The lifetimes of excitons in GaAs-Al_xGa_{1-x}As quantum wells were first reported by Christea *et al.*¹⁵ An increase of almost one order of magnitude in the transition rate of excitonic recombination in GaAs quantum wells with a well width of 52 Å compared with bulk GaAs has been observed. They also found that the decay of the excitonic recombination is nonexponential.

Molecular beam epitaxy (MBE) techniques can be used to grow QW and SL with very high quality but roughness at the interfaces of two materials of QW and SL can still not be completely eliminated. It is of interest and importance to know how this roughness affects the optical processes in QW's. The interface roughness (or interface defects) in QW's has been studied previously by low-temperature continuous-wave (cw) photoluminescence and by photoluminescence excitation spectroscopy.^{16,17} The main effects so far observed due to the interface roughness were exciton linewidth broadening and the red shift (Stokes shift) of the emission: the emission of the lowest heavy-hole exciton generally is slightly shifted to low energy (typically a few meV) with respect to the absorption or excitation spectrum maximum. This was attributed to localization of excitons within potential fluctu-

tuations due to interface roughness. The cw luminescence and photoluminescence excitation spectroscopy used to date to study the interface roughness of the QW yields very little understanding about the role of the interface roughness in the dynamic process of optical transitions.

In this paper we investigate the effects of interface roughness on the dynamic process of optical transitions. Low-temperature time-resolved photoluminescence of GaAs-Al_xGa_{1-x}As multiple QW's has been studied. The peak positions of heavy-hole exciton luminescence shifting with delay time has been observed. The shift is accounted for by interface roughness. A calculation based on interface roughness and a two-exponential decay forms fits the experimental results very well.

II. EXPERIMENT

The sample used for this study was a GaAs-Al_xGa_{1-x}As multiple quantum well (MQW) which was grown by molecular beam epitaxy on a GaAs(100) substrate without growth interruption. It consists of alternate 278-Å Al_xGa_{1-x}As barrier layers and 250-Å well layers with a total of ten periods. The x-ray diffraction data indicate a period length of 525 Å, which is in good agreement with the design parameters.

Excitation pulses of about 7 ps in duration at a repetition rate of 1 MHz were provided by a cavity-dumped ultrafast dye laser (Coherent 702-2CD) with an average power of 10 mW, which was pumped by a yttrium aluminum garnet (YAG) laser (Quantronix 416) with a frequency doubler. The pulse duration was continually monitored by using a rapid-scan autocorrelator.¹⁸ The lasing photon energy was 2.125 eV with a spectral width of 2 meV. A time-correlated single-photon counting system with a double monochromator (Jarell Ash 25-100) and a computer were used for the measurements. The effective time resolution of the system is about 0.2 ns. The sample was mounted strain free inside a closed-cycle He refrigerator and maintained at a temperature of 8.5 K.

III. RESULTS AND DISCUSSION

Experimental results of low-temperature (8.5-K) time-resolved photoluminescence at three different delay times for a GaAs-Al_xGa_{1-x}As MQW are plotted in Fig. 1. The exciting photon energy was 2.125 eV at an average power density of ~50 mW/cm². The luminescence at different delay times has been rescaled for presentation. The peaks at 1.5252 and 1.5295 eV are ascribed, respectively, to transitions of 1s heavy-hole ($n=1$, e-HH) and light-hole ($n=1$, e-LH) excitons, which are composed of an electron and a heavy (light) hole belonging to the lowest state ($n=1$) in the QW. These values are consistent with those calculated by using the transfer-matrix method^{19,20} with the conduction-band offset parameter being 0.65 and the binding energies of heavy- and light-hole excitons being 6.0 and 6.2 meV, respectively. The observed spectral width (about 1.78 meV) is attributed to the interface roughness of the QW.^{16,17} In Fig. 1 there is a shoulder at about 1 meV below the heavy-hole exciton

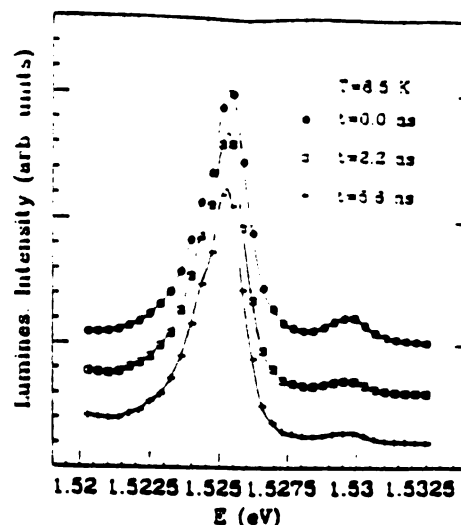


FIG. 1. Low-temperature (8.5 K) time-resolved photoluminescence at three different delay times for GaAs-Al_xGa_{1-x}As multiple quantum wells with thicknesses of the well and barrier being 250 and 278 Å, respectively. The excitation energy was 2.125 eV with an average power density about 50 mW/cm².

peak which has also been reported by Miller and co-workers.^{21,22} Based on the excitation intensity, temperature, and polarization dependencies of this low-energy peak (shoulder here), they concluded that it was due to a biexciton transition with a binding energy of about 1 meV. By using excitation-intensity-dependent luminescence and time-resolved spectroscopy, Charbonneau and co-workers²³ recently showed that the lower-energy components of heavy-hole excitonic transitions have different origins in different samples and can be attributed either to biexcitons or to impurity-bound excitons.

One important feature depicted in Fig. 1 is that the exciton transition peak shifts toward lower energy as the delay time increases. This is manifested as the intensity ratio of two data points at the exciton luminescence maximum changing with increasing delay time. Here, delay times were measured from the end of the excitation pulses. The origin of this shift cannot be correlated with the filling state phenomena^{24,25} because of the temporal behavior as will be discussed later.

In order to fully explore the fact that the exciton transition peak shifts with delay times, we have performed a high spectral resolution experiment around the peak position of the heavy-hole exciton transition. The results are shown in Fig. 2, where all the parameters and experimental conditions are the same as those in Fig. 1. The solid lines in Figs. 1 and 2 are a guide to the eye. Figure 2 clearly demonstrates that the peak position of the heavy-hole exciton transition shifts toward lower energy with increasing delay times. We have used a least-squares fit for the experimental data to find the peak positions at different delay times. The effect of the lower energy

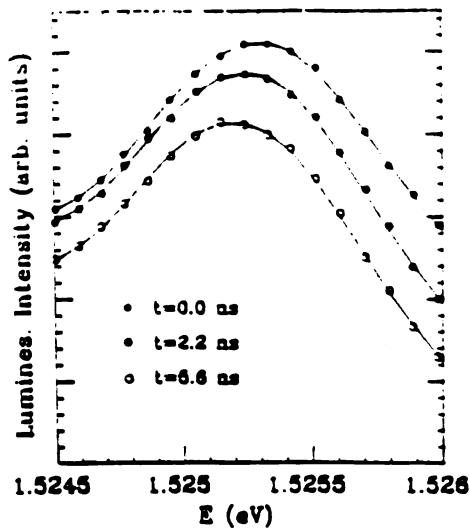


FIG. 2. High resolution time-resolved photoluminescence spectra around the peak position of the heavy-hole exciton transition at three different delay times. The spectral slit width and step width were, respectively, 0.4 and 0.5 Å. Other parameters and experimental conditions are the same as those in Fig. 1.

shoulder on the peak position of the heavy-hole exciton transition have been eliminated by deconvolution. This effect is shown to be negligible. Only a few data points around the maximum intensity of the excitonic transition were sufficient to obtain the peak position at different delay times. The results for the heavy-hole exciton peak position at different delay times are shown in Fig. 3 (circles). From Fig. 3 we see that the maximum shift is only about 0.1 meV at about 4 ns. Another feature is that the

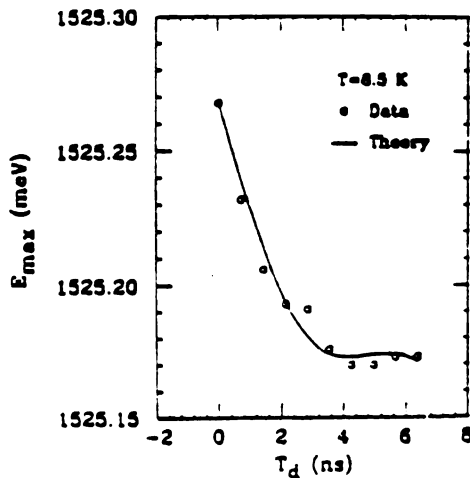


FIG. 3. Energy position of the emission intensity maximum of heavy-hole exciton as a function of delay time for GaAs- $\text{Al}_{0.3}\text{Ga}_{0.7}\text{As}$ multiple quantum wells. The quantum well parameters are the same as those in Fig. 1.

peak positions shows a red shift at the short delay time (0 ns), and then turns over beyond 4 ns. One notices that the shift at short delay times is almost linear. The amount of shift is small; nevertheless, it contains very important information. The experimental results shown in Fig. 3 can be interpreted in terms of the interface roughness in QW's and a two-exponential decay of the excitonic transition.

Figure 4 presents a schematic diagram of the interface roughness in a QW along the growth axis (a), and the concomitant effect on the photoluminescence linewidth broadening (b) and exciton lifetimes (c). The fluctuation in well (barrier) thickness can only be integral multiples of one monolayer. In the quantum-well layer plane, there are domains formed by the different well thicknesses with sizes varying from a few hundred angstroms to a few micrometers. Different emission energies around the principle excitonic peak correspond to excitons recombined in different spatial domains. As we have shown in Fig. 4, line A represents the lower photon energy which corresponds to excitons recombined at the location of a wider quantum well while line B represents the higher photon energy which corresponds to the excitons recombined at the location of a narrower quantum well. In Fig. 4(b) FWHM indicates the full linewidth at the half maximum. There was no investigation carried out previously ad-

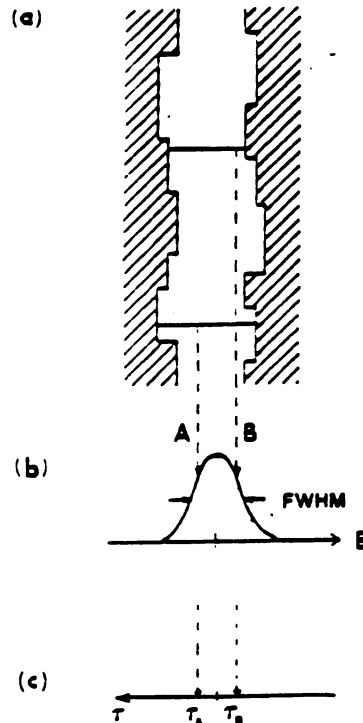


FIG. 4. A schematic diagram of the interface roughness in a quantum well shown along the growth axis (a). (b) and (c) show effects of roughness on the linewidth broadening and exciton lifetimes.

addressing the fact that excitons recombined at line A will also have a larger lifetime than those recombined at line B. Thus near the excitonic transition intensity maximum, the lifetime of the exciton, τ , will have a dependence on emission energy E , which can be written as $\tau(E)$. Because the well fluctuation normally is within a few monolayers the change in lifetime of excitons around the peak position is small. This is probably the reason that this effect has been previously neglected. However, the change of exciton lifetime with respect to the emission energy E , $d\tau/dE$, can provide very important physical information, since the recombination rate of the exciton depends on the QW thickness.^{26,27} The larger the quantum well width, the longer the exciton lifetime, as indicated in Fig. 4(c).

First, let us prove that energy-dependent exciton lifetimes can cause the transition peak to shift with the delay time. Because the total amount of peak shift is very small (0.1 meV) we can write τ as a function of E , near the energy of maximum intensity E_0 , as

$$\tau(E) = \tau(E_0) + (E - E_0)\alpha; \quad (1)$$

here $\tau(E_0)$ is the lifetime of excitons measured at the energy of maximum intensity of delay time $t_d = 0$ and α is the lifetime change rate with respect to energy, $d\tau/dE|_{E_0}$. Assuming the line-shape intensity distribution around the peak is a Gaussian with a single exponential decay, the luminescence of the excitonic transition can be written as a function of delay time t_d and energy E as

$$I(E, t_d) = I_0 \exp \left[-\frac{(E - E_0)^2}{\sigma^2} - \frac{t_d}{\tau(E)} \right]. \quad (2)$$

Here I_0 and E_0 are the maximum intensity of the excitonic transition and the energy position of the intensity peak at delay time $t_d = 0$, respectively, while σ defines the linewidth which correlates the QW thickness fluctuation parameter.²³ In Eq. (2), $I_0 \exp[-(E - E_0)^2/\sigma^2]$ represents the Gaussian intensity distribution at $t_d = 0$, and $\exp[-t_d/\tau(E)]$ is the decay factor which depends on energy. The peak positions at different delay times can be obtained by setting

$$\frac{dI(E, t_d)}{dE} = 0, \quad (3)$$

which gives

$$E_{\max}(t_d) = E_0 + \frac{\sigma^2}{2[\tau(E)]^2} \frac{d\tau}{dE} t_d. \quad (4)$$

Here we have assumed that the linewidth of the excitonic transition is independent of the delay time, which is consistent with the experimental results shown in Fig. 1. Because the second term in Eq. (1) is much smaller than the first, we obtain from Eq. (4)

$$E_{\max}(t_d) = E_0 + \frac{\sigma^2}{2} \frac{\sum_{i=1}^2 [C_i \alpha_i t_d / \tau_i^2(E_0)] \exp[-t_d / \tau_i(E_0)]}{\sum_{i=1}^2 C_i \exp[-t_d / \tau_i(E_0)]}. \quad (9)$$

$$E_{\max}(t_d) = E_0 - \frac{\tau^2}{2(E - E_0)^2} \alpha t_d. \quad (5)$$

Equation (5) indicates that the peak position of the excitonic transition will shift linearly to lower energies as the delay time increases, since $\alpha = d\tau/dE = d\tau/dL / (dE/dL) < 0$, i.e., $d\tau/dL > 0$ and $dE/dL < 0$. Here L is the average thickness of the QW's.

The above calculation shows that the peak position of the excitonic transition will shift as the delay time increases because of the presence of interface roughness in the QW's. However, Eq. (5) only gives a linear red shift of peak position with the delay time, which is inconsistent with experimental observation depicted in Fig. 3. The experimental results are more complicated and cannot be fully described by Eq. (5). As we will see, by using the above treatment with the assumption of a two-exponential decay for luminescence, the experimental results can be well accounted for. This is obtained by rewriting the luminescence intensity as a function of emission energy E and delay times t_d , around the peak position, as

$$I(E, t_d) = \exp[-(E - E_0)^2/\sigma^2] \times \{ A \exp[-t_d/\tau_1(E)] + B \exp[-t_d/\tau_2(E)] \}, \quad (6)$$

where A and B are constants. Here τ_1 and τ_2 are time constants which are both functions of energy E . From Eq. (3) we get

$$E_{\max}(t_d) = E_0 - \frac{\sigma^2 f(E, t_d)}{2 g(E, t_d)}, \quad (7)$$

with

$$f(E, t_d) = \sum_{i=1}^2 \frac{C_i t_d}{\tau_i(E)} \left[\frac{d\tau_i}{dE} \right] \exp \left[-\frac{t_d}{\tau_i(E)} \right] \quad (7a)$$

and

$$g(E, t_d) = \sum_{i=1}^2 C_i \exp \left[-\frac{t_d}{\tau_i(E)} \right], \quad (7b)$$

where

$$C_i = \begin{cases} 1 & (i=1) \\ B/A & (i=2) \end{cases}. \quad (7c)$$

One notices that $C_2 = B/A$ is the ratio of two luminescence components at $t_d = 0$. For energies near that of the excitonic transition peak, we can write

$$\tau_i(E) = \tau_i(E_0) - (E - E_0)\alpha_i \quad (i=1, 2). \quad (8)$$

By using Eqs. (7), (7a), (7b), and (8) we obtain

Parameters σ , τ_1 , τ_2 , and C_2 can be deduced from experimental measurements. One sees that σ is related to the FWHM by $\text{FWHM} = 2(\ln 2)^{1/2} \sigma$. The value of FWHM obtained from Fig. 1 is about 1.78 meV, which gives $\sigma = 1.07$ meV. $\tau_1(E_0)$ (-0.9 ns) is the time constant of the fast decay component of exciton luminescence measured at the energy of the intensity maximum occurring at $t_d = 0$, which corresponds to the exciton lifetime of radiative recombination. $\tau_2(E_0)$ is the time constant of the slow decay component, which is measured to be 4.2 ns. One notices that this time constant does not represent the lifetime of exciton recombination since it is even larger than the exciton lifetime in bulk GaAs (3.3 ns).²⁹ (The physical origin for this two-exponential decay is under investigation.) Now C_2 is measured to be 0.07. We insert these values into Eq. (9) and adjust α_1 and α_2 to obtain the least-square fit with experimental data. We find that, with $\alpha_1 = -0.06$ ns/meV and $\alpha_2 = -0.42$ ns/meV, the plot of Eq. (9) shown as the solid line in Fig. 3 is in excellent agreement with experimental results (circles). Here α_1 represents the change rate of exciton lifetime with respect to emission energy, and thus the fitting value (-0.06 ns/meV) gives a total lifetime change of the fast decay component of about $0.06 \times 1.3 = 0.1$ (ns) within the FWHM. However, as we will show later, one does not need to measure the exciton lifetime of QW's with different thicknesses in order to obtain the change rate of exciton lifetime with respect to well thickness, $d\tau/dL$. A much easier way to obtain $d\tau/dL$ is to measure the peak position shift as a function of delay time.

We studied the temporal response of the luminescence at the excitonic transition peak as shown in Fig. 5. The circles are the experimental values which have been deconvoluted to account for the temporal response of the

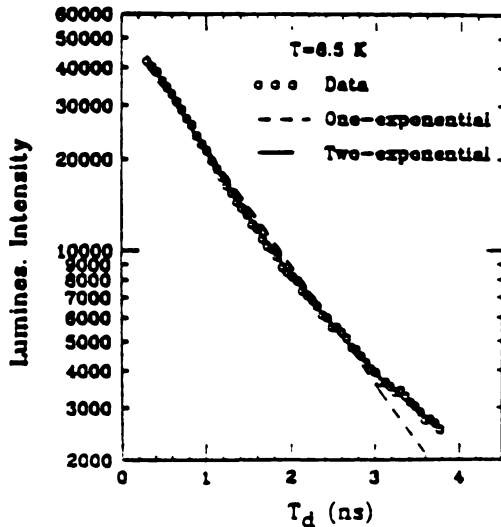


FIG. 5. Luminescence of heavy-hole exciton as a function of delay time. The circles show the measured values while the dashed and solid lines are fit using one- and two-exponential decay models, respectively (see text).

detection system. The rising part of the luminescence is not shown here. The dashed and solid lines are the theoretical fit obtained using one- and two-exponential decay models, respectively. From Fig. 5 it is clear that the decay of heavy-hole excitons cannot be described by a single exponential form. The two-exponential decay fits the experimental results very well. The decay time constants obtained from Fig. 5 are 0.9 and 4.2 ns, respectively, for the fast and slow components. This two-exponential decay behavior has been observed recently by other groups.³⁰⁻³²

Following the discussions presented above, $d\tau/dE$, the time-constant change rate with respect to emission energies E obtained from the peak shift, can be used to deduce the lifetime of the exciton in QW's of different well thickness, since we knew from previous work that the lifetime of the exciton increases almost linearly with well thickness.^{16,27} From $\alpha = d\tau/dE = (d\tau/dL)/(dE/dL)$, we have

$$\frac{d\tau}{dL} = \alpha \frac{dE}{dL}. \quad (10)$$

Here

$$E = E_g(\text{GaAs}) + E_e + E_h - E_{\text{bind}}, \quad (11)$$

with $E_g(\text{GaAs})$ being the energy gap of GaAs material. E_e (E_h) is the confinement energy of the electron (hole) in the QW which is measured from the bottom of the conduction (top of the valence) band. E_{bind} is the binding energy of the exciton. By noting that the change in the binding energy of the exciton with respect to well thickness L , dE_{bind}/dL , is much smaller than the change in confinement energy of the electron or hole, we can neglect dE_{bind}/dL . In addition, the confinement energies of the ground-state electron and hole (of the order of 10 meV for our sample) are much less than those of the conduction and valence potential barriers (a few hundred meV here). Thus we can estimate E_e and E_h by treating electrons and holes as particles bound inside an infinitely deep QW. Therefore we have

$$E_e + E_h = \frac{\hbar^2 \pi^2}{2m_e^* L^2} + \frac{\hbar^2 \pi^2}{2m_h^* L^2} = \frac{\hbar^2 \pi^2}{2\mu^* L^2}. \quad (12)$$

Here L is the average well thickness and $\mu^* = m_e^* m_h^* / (m_e^* + m_h^*)$ is the effective reduced mass of the exciton. From Eqs. (10)-(12) we obtain

$$\frac{d\tau}{dL} = - \frac{\hbar^2 \pi^2}{2\mu^* L^3} \alpha. \quad (13)$$

We used $m_e^* = 0.067m_0$ and $m_h^* = 0.45m_0$ for the electron and hole effective masses inside the QW,^{33,34} where m_0 is the effective mass of electron in the free space. With well thickness parameters of $L = 250$ Å and $\alpha_1 = -0.06$ ns/meV obtained in the above we find

$$\frac{d\tau}{dL} = 2.6 \times 10^{-3} \text{ ns/Å}.$$

This value is in good agreement with those extrapolated from the experimental results of Ref. 26, i.e., -2.5×10^{-3} ns/Å. Here we want to indicate that in Ref.

26 the authors defined the time at which the intensity has dropped to 1/2 of its maximum value, $\tau_{1/2}$, as the lifetime of the exciton. The real lifetime of the exciton radiative recombination will be different from this value. Nevertheless, $d\tau/dL$ deduced from their experimental results will be very close to the real value. Since exciton lifetime is approximately proportional to well thickness, one can deduce the exciton lifetime for different well thicknesses by measuring τ and $d\tau/dL$ for one quantum-well thickness.

IV. CONCLUSIONS

We have studied the effect of interface roughness on the time-resolved photoluminescence of the excitonic transition of GaAs-Al_xGa_{1-x}As multiple QW's. We found that the energy position of intensity maximum of the excitonic transition shifted as the delay time increased. Based on a model involved interface roughness in the QW's and the form of a two-exponential decay for luminescence, we calculated the peak position as a function of delay times. The calculated results are in good agreement with experimental observations. From these measurements, we obtained the change rate in exciton lifetime with respect to the well thickness L . We showed that this is a very effective method to measure $d\tau/dL$ compared with the usual procedure of measuring exciton

lifetimes at different well thicknesses directly. From the above discussions we see that besides the linewidth broadening and Stokes red shift, the interface roughness also strongly affects the dynamic process of the optical transition. The results obtained here are very important for fundamental research and also very useful for practical applications, such as narrowing the spectral and time pulse widths of QW lasers.

Obviously, the effect of QW thickness fluctuations on the dynamic process of optical transitions is very important. There are still many important questions to be answered. One of the most important questions here is why the decay of the exciton transition is composed of a two-exponential form. In future work, we will study the dynamic process of the optical transition by using QW's with different well thicknesses and at different temperatures. We hope that these studies will provide more understanding of the complicated effects of interface roughness.

ACKNOWLEDGMENTS

The research reported here was supported by the Michigan State University Center for Fundamental Materials Research. H.X.J. would like to acknowledge useful discussions with J. Y. Lin.

*Present address: Solid State Laboratories, New York University, 4 Washington Place, Room 314, New York, NY 10003.

¹L. Esaki, *J. Phys. (Paris) Colloq.* **48**, C5-1 (1987).

²L. Esaki, *IEEE J. Quantum Electron.* **QE-22**, 1611 (1986).

³R. C. Miller, D. A. Kleinman, W. A. Nordland, and A. C. Gossard, *Phys. Rev. B* **22**, 863 (1980).

⁴J. Feldmann, G. Peter, E. O. Gobel, P. Dawson, K. Moore, C. Foxon, and R. J. Elliott, *Phys. Rev. Lett.* **59**, 2337 (1987).

⁵L. Esaki and R. Tsu, IBM Research Note No. RC-2418, 1969 (unpublished).

⁶L. Esaki and R. Tsu, *IBM J. Res. Dev.* **14**, 61 (1970).

⁷R. Tsu and L. Esaki, *Appl. Phys. Lett.* **22**, 562 (1973).

⁸C. L. G. Solner, W. D. Goodhue, P. E. Tannenwald, D. Parker, and D. D. Peck, *Appl. Phys. Lett.* **43**, 588 (1983).

⁹J. C. M. Hwang, A. Kastalsky, H. L. Stormer, and V. G. Keramida, *Appl. Phys. Lett.* **44**, 802 (1984).

¹⁰M. Heiblum, E. E. Mendez, and F. Stern, *Appl. Phys. Lett.* **44**, 1064 (1984).

¹¹Y. Arakawa and A. Yariv, *IEEE J. Quantum Electron.* **QE-22**, 1887 (1986).

¹²M. Asada, Y. Miyamoto, and Y. Suematssu, *IEEE J. Quantum Electron.* **QE-22**, 1915 (1986).

¹³H. L. Stormer, K. Baldwin, A. C. Gossard, and W. Wiegmann, *Phys. Rev. Lett.* **44**, 1062 (1984).

¹⁴S. Luryi, A. Kastalsky, and J. C. Bean, *IEEE Trans. Electron Devices* **ED-31**, 1135 (1984).

¹⁵J. Christen, D. Bimberg, A. Steckenborn, and G. Weimann, *Appl. Phys. Lett.* **44**, 84 (1983).

¹⁶C. Weisbuch, R. Dingle, A. C. Gossard, and W. Wiegmann, *Solid State Commun.* **38**, 709 (1981).

¹⁷C. Weisbuch, R. Dingle, A. C. Gossard, and W. Wiegmann, *J. Vac. Sci. Technol.* **17**, 1123 (1980).

¹⁸Y. Ishida, T. Yajima, and Y. Tanaka, *Jpn. J. Appl. Phys.* **19**, L239 (1980).

¹⁹E. Merzbacher, *Quantum Mechanics*, 2nd ed. (Wiley, New York, 1970), pp. 73-105.

²⁰H. X. Jiang and J. Y. Lin, *J. Appl. Phys.* **61**, 624 (1987).

²¹R. C. Miller, D. A. Kleinman, A. C. Gossard, and O. Munteanu, *Phys. Rev. B* **25**, 6545 (1982).

²²R. C. Miller and D. A. Kleinman, *J. Lumin.* **30**, 520 (1985).

²³S. Charbonneau, T. Steiner, M. L. W. Thewalt, E. S. Soteles, J. Y. Chi, and B. Elman, *Phys. Rev. B* **38**, 3583 (1988).

²⁴Y. Masumoto, S. Tarucha, and H. J. Okamoto, *Phys. Soc. Jpn.* **55**, 57 (1986).

²⁵H. Weinert, F. Henneberg, V. Woggen, I. N. Uraltsev, and H. G. Brahl, *Phys. Scr.* **35**, 76 (1987).

²⁶R. Hoger, E. O. Gobel, J. Kuhl, K. Ploog, and G. Weimann, in *Proceedings of the Seventeenth International Conference on the Physics of Semiconductors, San Francisco, 1984*, edited by J. D. Chadi and W. A. Harrison (Springer-Verlag, New York, 1985), p. 575.

²⁷J. Feldmann, G. Peter, E. O. Gobel, P. Dawson, K. Moore, C. Foxon, and R. J. Elliott, *Phys. Rev. Lett.* **59**, 2337 (1987).

²⁸H. X. Jiang and J. Y. Lin, *J. Appl. Phys.* **63**, 1984 (1988).

²⁹G. W. Hooft, W. A. J. A. van der Poel, L. W. Molenkamp, and C. T. Foxon, *Phys. Rev. B* **35**, 8231 (1987).

³⁰J. Christen, D. Bimberg, A. Steckenborn, and G. Weimann, *Appl. Phys. Lett.* **44**, 34 (1984).

³¹P. Dawson, G. Duggan, H. I. Ralph, and K. Woodbridge, in *Proceedings of the Seventeenth International Conference on Semiconductors, San Francisco, 1984*, edited by J. D. Chadi and W. A. Harrison (Springer, New York, 1985), p. 551.

³²M. Kohl, D. Heitmann, S. Tarucha, K. Leo, and K. Ploog, *Phys. Rev. B* **39**, 7736 (1989).

³³C. Mailhot, Y. C. Chang, and T. C. McGill, *Phys. Rev. B* **26**, 4449 (1982).

³⁴C. Priester, G. Allan, and M. Lannoo, *Phys. Rev. B* **30**, 7302 (1984).

Interfacial effects and superconductivity in high- T_c materials

S. Vieira,* P. Zhou, and S. A. Solin

Center for Fundamental Materials Research, Department of Physics and Astronomy,
Michigan State University, East Lansing, Michigan 48824

N. Garcia, M. Hortal, and A. Aguiló

Departamento Física Materia Condensada, Universidad Autónoma Madrid, Madrid 28049 Spain

(Received 2 March 1988; revised manuscript received 20 July 1988)

A series of quasihomogeneous superconducting powders of $\text{YBa}_2\text{Cu}_3\text{O}_{7-x}$ have been prepared by sieving and characterized by electron microscopy and x-ray diffraction. Quantitative size-dependent and temperature-dependent magnetic levitation and susceptibility measurements of random powders and of field-oriented (at $T < T_c = 92$ K) small grains ($< 20 \mu\text{m}$) confirm previously observed symmetry-breaking effects associated with the twin boundary planes and suggest that the bulk anisotropic superconductivity is measurably perturbed by interfacial effects. Current models of interfacial superconductivity in high- T_c materials are evaluated in light of these and other results and are found to be lacking.

It is commonly assumed that $\text{YBa}_2\text{Cu}_3\text{O}_{7-x}$ is a *pure* bulk anisotropic superconductor^{1,2} (BAS) whose properties are influenced by the (110) twin boundary planes (TP's) which are a natural consequence of its orthorhombic structure³ and act as "weak links" between BAS regions. But the only theoretical model to date which quantitatively relates the bulk superconductivity to TP's is the superconducting glass model.² This model is controversial and the subject of serious challenge.⁴

Recently, Garcia *et al.*⁵ suggested that the superconductivity in $\text{YBa}_2\text{Cu}_3\text{O}_{7-x}$ is a nonbulk TP effect. On the basis of scanning tunneling microscopy (STM), ac susceptibility, and qualitative levitation measurements they identified the TP's as "strong links" and attributed the superconductivity to a *purely interfacial* Allender-Bray-Bardeen (ABB) excitonic mechanism⁶ which would function for all temperatures below T_c . While x-ray studies of oriented small-grained powders⁷ showed symmetry-breaking supercurrent paths parallel to the TP's in addition to those parallel to the basal (*ab* CuO) planes, these studies were compatible with either a weak-link or strong-link origin. Subsequently, TP supercurrents have been associated with the hybrid phenomenon of twin-plane superconductivity⁷ (TPS) and with oxygen vacancy ordering⁸ (OVO) both of which are activated at a temperature $T_c' < T_c$ below which the BAS mechanism obtains. (Note that BAS is the underpinning of TPS and OVO neither of which can exist in pure form and both of which are strong-link models.) To date the TPS model has been employed to quantitatively account for the temperature dependence of the upper critical fields⁹ and of the specific heat¹⁰ of $\text{YBa}_2\text{Cu}_3\text{O}_{7-x}$. While the evidence for interfacial effects in the superconductivity of $\text{YBa}_2\text{Cu}_3\text{O}_{7-x}$ is suggestive it is not conclusive. Accordingly, we present in this article the first quantitative studies of the magnetic levitation and susceptibility of oriented powders of $\text{YBa}_2\text{Cu}_3\text{O}_{7-x}$. These studies are apparently incompatible with the assumption of *pure* BAS but support a hybrid mechanism which partially localizes the supercurrents to

the neighborhood of the TP's.

Quasihomogeneous powders of $\text{YBa}_2\text{Cu}_3\text{O}_{7-x}$, $x \sim 0$, were synthesized by the usual method¹¹ and sieved into the following size distributions: $d < 20 \mu\text{m}$; $\delta - \epsilon < d < \delta + \epsilon$, $\epsilon = 5$, $\delta = 25, 35, 45 \mu\text{m}$; $\epsilon = 12.5 \mu\text{m}$, $\delta = 62.5, 87.5 \mu\text{m}$. Powder x-ray diffraction studies of these $\text{YBa}_2\text{Cu}_3\text{O}_{7-x}$ specimens revealed only those structural features associated with the 1:2:3 superconducting phase. We focus here on specimens with $d < 20 \mu\text{m}$ the typical grains of which are shown in the scanning electron micrographs of Fig. 1. As can be seen from that figure, the typical grain is a disklike platelet with a basal (*ab*) surface and an aspect ratio [= (diameter)/(thickness)] of ~ 1.5 . It is known¹² that for small grains of this type the TP's exhibit a unidirectional or at most bidirectional domain structure, the former of which is illustrated in Fig. 2.

Levitation studies were carried out using the apparatus¹³ depicted in Fig. 2, with a transverse permanent magnet having $(H_z)_{\text{max}} \approx 5000$ G. The field $H_z(z)$, which was measured with a spatial resolution of 0.5 mm using a Hall probe, is shown in Fig. 3 together with a seven-parameter polynomial least-squares fit from which the gradient (also shown in Fig. 3) was obtained. Susceptibility studies and field-induced alignments were performed with a SHE variable-temperature susceptometer while x-ray studies were performed with a conventional Siemens powder diffractometer using a Cu $K\alpha$ source and a spinning sample holder.

When powders with $d < 20 \mu\text{m}$ are dropped from a height z at which $H_z(z) = 0$ through liquid nitrogen (LN) into the inhomogeneous field of the magnet shown in Fig. 2, the monodispersed single-domain grains do not levitate but instead collect at the bottom of the confinement tube. If the temperature is reduced, these grains first levitate at 74 ± 2 K at $z = 4$ mm and continue to do so with decreasing temperature and/or increasing z until $z = 14$ mm for liquid-helium (LH) immersion. When small grains which are nonlevitating in LN are lightly compacted (without sintering or chemical alteration) into a pellet, that pellet



FIG. 1. Scanning electron micrographs of the $d < 20 \mu\text{m}$ powders of $\text{YBa}_2\text{Cu}_3\text{O}_{7-x}$, taken at magnifications of 1000 (lower panel) and 2000 (upper panel). The large flat faces of grains such as that centered in the upper panel are basal (ab) surfaces.

levitates in LN (LH) at $z = 8 \text{ mm}$ (17 mm). Grains with $d > 20 \mu\text{m}$ also levitate in both LN and LH at these same heights. All of the loose and compact random powders are superconducting with typical Meissner fractions (measured according to methods established by Krusin-Elbaum, Maiozemoif, and Yeshurun¹⁴) in excess of 50% as shown by the data of Fig. 4. The random powder data of Fig. 4 are typical of pure phase 1:2:3 material and show none of the features, e.g., kinks at $T < T_c$ which are normally associated with impurity phases and/or reduced oxygenation.¹⁵

Assume for the sake of analytic solutions that the $\text{YBa}_2\text{Cu}_3\text{O}_{7-x}$ particles are magnetically anisotropic pure BAS ellipsoids whose susceptibility and demagnetization tensors have coincident principal axes. A particle of volume V in an applied magnetic field H_0 will adopt a configuration which minimizes U (Ref. 16) where

$$U = -\frac{1}{2} \int_V \mathbf{M} \cdot \mathbf{H}_0 dV = -\frac{1}{2} \int_V \sum_j \frac{\chi_j}{1+N_j \chi_j} H_0^2 dV. \quad (1)$$

Here, \mathbf{M} is the magnetization of the particle; N_j , χ_j , and H_0 are the demagnetizing factor, susceptibility, and projection of the field along the j th principal axis, respectively; and $\sum_j N_j = 4\pi$. The torque and force on the particle can be obtained from U , e.g., $\tau_\theta = \partial U / \partial \theta$, $F_z = \partial U / \partial z$, etc.

Equation (1) can be used to establish the z dependence of the levitation force when the free particle has oriented

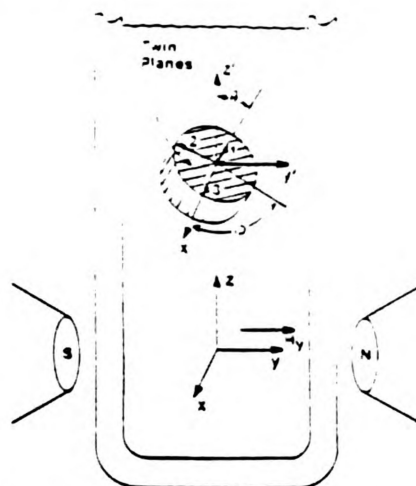


FIG. 2. A schematic diagram of the levitation experiment with axes and angles labeled for reference in the text. The principal axes of the demagnetization tensor are labeled 1, 2, 3 and are parallel, respectively, to the crystallographic axes c , a (or b), b (or a).

itself to minimize U . Suppose a particle has descended into a region where its local field is less than the lowest critical field H_{c1}^{\parallel} ($\parallel - H_0 \parallel ab$ planes). Then $\chi_j = -1/4\pi$, $j=1,2,3$, and the term in Eq. (1) with minimum N_j minimizes U . The particle will align with its longest principal axis (axis 2 in Fig. 2) $\parallel H_0$. If $N_2 \ll 4\pi$ or $H_0 \gg H_{c1}^{\parallel}$, the levitation condition is

$$F_z(z) = \frac{1}{2} V M_y (\partial H_y(z) / \partial z) = (\rho - \rho_{LN}) g V, \quad (2)$$

where $M_y = H_y / 4\pi$, $\rho = 6.38 \text{ g/cm}^3$ is the mass density of $\text{YBa}_2\text{Cu}_3\text{O}_{7-x}$, $\rho_{LN} = 0.6 \text{ g/cm}^3$ is the density of liquid nitrogen, and g is the gravitational acceleration.

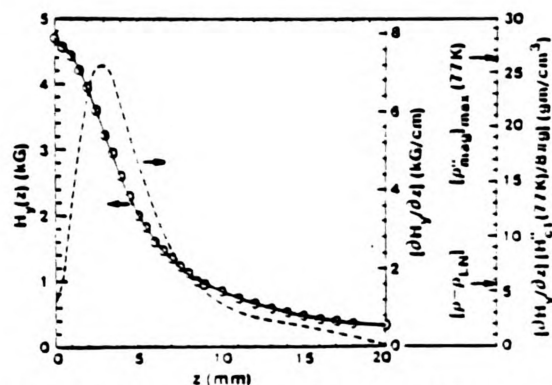


FIG. 3. The measured transverse field (circles) and a seven-parameter polynomial fit (solid line) (see text). The gradient (dashed line) was obtained analytically from the polynomial fit. The additional ordinate scale on the far right renormalizes the gradient to $\rho_{LN}^{\text{max}}(z)$ (77 K) the maximum value of which is indicated along with $\rho - \rho_{LN}$, the buoyancy-corrected gravitational mass density of $\text{YBa}_2\text{Cu}_3\text{O}_{7-x}$.

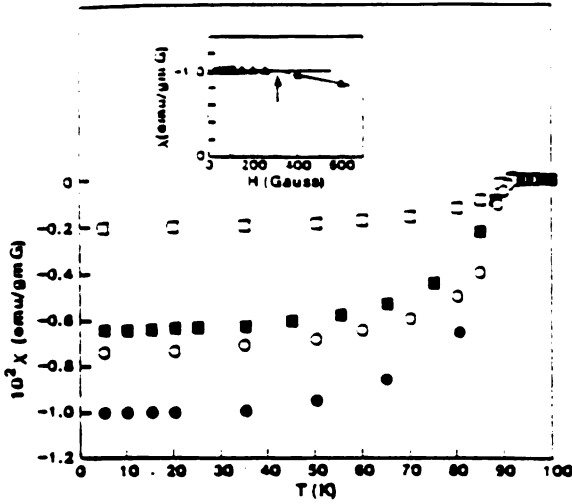


FIG. 4. The temperature dependence of the mass susceptibility of $\text{YBa}_2\text{Cu}_3\text{O}_{7-x}$ powder ($d < 20 \mu\text{m}$) in a random configuration (circles) and field-oriented (see text) configuration (squares). Open (solid) symbols represent field cooling at 18 G (zero-field cooling followed by field heating at 25 G). Inset: the field dependence of the 5-K susceptibility of random powder (Δ) showing the extrapolated critical field $H_{c1}^a(5 \text{ K}) = 300 \pm 25 \text{ G}$ (vertical arrow).

Equivalently, if we define $\rho_{\text{mag}}(z) = F_z(z)/Vg$ to be the magnetic mass density, the particle will levitate if $[\rho_{\text{mag}}(z)]_{\text{max}} \geq \rho - \rho_{\text{LN}}$.

When the local field exceeds the lower critical field H_{c1}^a , along one or more of the principal axes of the particle, it enters the vortex state. For $\text{YBa}_2\text{Cu}_3\text{O}_{7-x}$,

$$H_{c2}^b = H_{c2}^c = H_{c2}^a \gg H_{c1}^a, \quad H_{c2}^b = H_{c2}^c \gg H_{c1}^b$$

and

$$H_{c1}^a < H_{c1}^b < H_{c1}^c < H_{c2}^a.$$

(Magnetic anisotropy in the ab plane, although expected,³ has been observed⁷ but not yet measured.) In the range

$H_{c1}^a < H_z \ll H_{c2}^a$, M is approximately linear in H in which case

$$\chi_z = -(1/4\pi)(H_{c1}^a/H_z), \quad (3)$$

$$H_z = H_0 + (N_z/4\pi)H_{c1}^a, \quad (4)$$

$$\chi_z/(1 + N_z\chi_z) = -(1/4\pi)(H_{c1}^a/H_z) \quad (5)$$

Then the levitation condition is given by Eq. (2) but with the term $H_z(z)$ replaced by H_{c1}^a . For $H_0 \gg H_{c1}^a$, demagnetizing effects are negligible and the particle will align in a direction which minimizes flux expulsion, i.e., along the axis with the minimum value of H_{c1}^a . In the language of anisotropic Ginzburg-Landau theory¹⁷ this is the direction corresponding to the smallest effective mass and thus the highest H_{c2}^a . But the product of H_{c1}^a and H_{c2}^a is roughly constant, i.e., $(H_{c1}^a H_{c2}^a)^{1/2} \approx H_c$ where H_c is the thermodynamic critical field. So the direction with maximal H_{c2}^a also has minimal H_{c1}^a as asserted above.

We have used Eqs. (1)-(5) to determine the levitation force on and preferred orientation of a BAS particle. The results are summarized in Table I. The values of $(\rho_{\text{mag}}^1)_{\text{max}}$ cited in that table were deduced from Fig. 2 using $H_{c1}^a(77 \text{ K}) = 90 \pm 8 \text{ G}$. The latter was computed¹⁸ from the lower critical field, $H_{c1}^a(5 \text{ K}) = 300 \pm 25 \text{ G}$, at which $\chi(H, T = 5 \text{ K})$ of a random powder linearly departs from constancy (see inset, Fig. 4). This departure commences when $H_0 \approx H_{c1}^a$ for particles in the powder which happen to be aligned with their ab planes $\parallel H_0$. Although the departure is in principle quadratic in applied field for single-crystal specimens or fully aligned widely spaced grains, its analytic form, which depends strongly on uncalculable local-field corrections, is not known for powder specimens. The assumption of a linear departure which we used to compute $H_{c1}^a(5 \text{ K})$ from the inset data of Fig. 4 is thus reasonable and uncertainties which this assumption introduce are reflected in the large error bars on our measured value of H_{c1}^a . Moreover, the above specified value of $H_{c1}^a(5 \text{ K})$ is consistent with our measurements of oriented powders and lies at the low end of the range of reported values^{11,19} for that parameter.

Notice from Table I that a pure BAS analysis predicts that the particle will not levitate in the Meissner state because field limitations constrain ρ_{mag}^1 to values $\ll \rho$. How-

TABLE I. Orientation and levitation of a bulk anisotropic superconducting particle in a transverse field, $H_z(z)$ at 77 K. The symbols m , v , and n denote the Meissner, vortex, and normal states, respectively, and $S = \frac{1}{V} M_z V(\partial H_z(z)/\partial z)$, where V is the particle volume and M_z is the induced moment. Axis labels refer to Fig. 2.

State	Applied field	Axis orientation	F_z (dyn)	$(\rho_{\text{mag}}^1)_{\text{max}}$ g/cm ³
m	$H_z < H_{c1}^a \left[1 - \frac{N_z}{4\pi} \right]$	(2) $\parallel H_z$	$S H_z(z)$	0.73 ≈ 0.05
v	$H_{c1}^a \left[1 - \frac{N_z}{4\pi} \right] < H_z < H_{c2}^a$	(2) $\parallel H_z$	$S H_{c1}^a$	26.3 ≈ 3.5
n	$H_z > H_{c2}^a$	(1) $\parallel H_z$	0	0
n	$H_z > H_{c2}^b$	None	0	0

ever, the particle *should* levitate in the vortex state for which $(\rho_{\text{mag}}^1)_{\text{max}} > 4(\rho - \rho_{\text{LN}})$. If flux is more effectively expelled from the TP's (of width t with spacing L) than from the intervening regions (of width $L - t$) as would be the case in a strong-link hybrid model, $(\rho_{\text{mag}}^1)_{\text{max}}$ will be reduced by approximately t/L . Then under the condition $t/L < (\rho - \rho_{\text{LN}})/(\rho_{\text{mag}}^1)_{\text{max}} = 0.22$ small particles will not levitate at 77 K, as is observed. Nonlevitation is thus likely since the spread in reported values of t (Refs. 4 and 20) and L (Ref. 21) limit their ratio to $\frac{1}{100} < t/L < \frac{1}{50}$. If T_L is the temperature at which small particles just begin to levitate at maximum gradient,

$$[(1/8\pi g)(t/L)H_{c1}^1(T_L)\{\partial H_z(z)/\partial z\}_{\text{max}} = \rho - \rho_{\text{LN}},$$

where

$$H_{c1}^1(T_L) \approx H_{c1}^1(5 \text{ K})[1 - (T_L/92)^2],$$

an empirical relation¹⁸ which yields the expected linear variation^{1,8} near $T_c = 92$ K. Using the fact that for $T_L = 74 \pm 2$ K small particles just levitate at $z = 3.5 \pm 0.5$ mm, the height of maximum gradient (see Fig. 3), we find $t/L = 0.19 \pm 0.04$. For the case of $t \sim 80$ Å (Ref. 4) [5 Å (Ref. 20)], $L = 400 \pm 100$ Å (25 ± 6 Å), well within (outside) the accepted range.²¹

The TP correction factor does not apply to random powders, multigrained particles, or to large particles with multidirectional TP domains. These morphologies cannot uniquely align and the tilted (nonaligned) TP's screen flux from the intervening regions. It is impossible to analytically calculate the levitation force for such agglomerates because the nonlinear susceptibility in the vortex state leads to nonuniform local-field corrections. However, if we treat a compacted pellet empirically as a disk with an isotropic χ , the levitation force it will experience is given by the force expression for the vortex state (row 2, column 4 of Table I). Using our measured value of $H_{c1}^1(77 \text{ K})$ we find that the pellet should levitate when $\partial H_z(z)/\partial z = 2242 \pm 187$ G/cm. This value obtains at $z = 7.5 \pm 0.8$ mm (see Fig. 3). A corresponding analysis for $T = 5$ K yields a levitation height of 13 ± 2 mm. Both of these results agree well with observation.

We now address our susceptibility measurements of random and oriented powders of small $\text{YBa}_2\text{Cu}_3\text{O}_{7-x}$ particles. Figure 4 shows $\chi(T)$ for random $d \approx 20$ μm powder (solid and open circles) and of the same powder after orientation in a field of 5 kG at $t = 5$ K (solid and open squares). These data have been used to compute¹⁸ Meissner fractions, F , of 54% and 22% at 5 K, respectively. The applied fields were well below the lowest critical field of $\text{YBa}_2\text{Cu}_3\text{O}_{7-x}$, and in the same direction as the orienting field.

The dramatic drop in the Meissner fraction of the oriented specimen is not likely to be due to flux penetration since $\lambda(5 \text{ K}) \leq 0.8$ μm (Refs. 1 and 19) which is considerably less than the ~ 10 μm thickness of a typical aligned particle (see further discussion below). Moreover, this drop does not derive from field-induced decoupling of weak links since such links between loosely packed single grains will be too weak to sustain supercurrents in either random or oriented powders. The drop in F could result

from anisotropic flux trapping in pure BAS particles.⁴ Alternatively, if the supercurrents are partially localized in the TP's that align with the orienting field, flux could penetrate between these planes resulting in a drop in F . Our levitation results point towards the latter explanation.

Implicit in the above analyses of levitation and susceptibility is our assertion that the effects which we have observed are not merely a manifestation of ordinary flux penetration which would reduce both of these observables. To further explore this point we note that for a thin slab aligned with its face parallel to the applied field, the susceptibility and the levitation force should both be multiplied by the factor $k = \{1 - [\tanh(a/\lambda)]/(a/\lambda)\}$ where λ is the penetration depth and $2a$ is the width of the slab.²² If we attribute nonlevitation to this factor then $k = (\rho - \rho_{\text{LN}})/(\rho_{\text{mag}}^1)_{\text{max}} = 0.22$ and $a/\lambda = 0.94$. If we use the empirical relation

$$\lambda(T) = \lambda(T_0)[1 - (T/T_c)^4]/[1 - (T/T_c)^4]$$

with $T_0 = 5$ K and $\lambda(5 \text{ K}) = 0.8$ μm ,¹⁹ the maximum reported value, then $\lambda(77 \text{ K}) = 1.92$ μm and $a/\lambda \geq 5.2$. This value is more than a factor of 5 larger than the value required for nonlevitation. Furthermore, if we make the conservative but clearly unfounded assumption that the oriented powder used for the susceptibility measurements was fully aligned, a reduction factor of only 0.22 cannot account for the approximate factor of 2 drop in the Meissner fraction evidenced in Fig. 4. Thus flux penetration cannot rescue the pure BAS model.

Although we have demonstrated certain deficiencies in pure BAS models of $\text{YBa}_2\text{Cu}_3\text{O}_{7-x}$, we cannot identify which, if any, of the currently proposed TP perturbative mechanisms is applicable. The ABB model^{3,6} and other purely interfacial models of this type such as those based on surface plasmons require metal-semimetal/semiconductor interfaces and consequently significant volume fractions of bulk semimetal/semiconductor interfaces. Surface-sensitive STM experiments⁴ show large regions of semiconductor but bulk NMR measurements²³ do not. The TPS hybrid model^{8,24} produces measurable effects only when the TP spacing is less than the Ginzburg-Landau correlation length of ~ 34 Å. There is no evidence to date of such small TP spacings in $\text{YBa}_2\text{Cu}_3\text{O}_{7-x}$. Indeed, spacings of this magnitude would result in a large volume fraction of TP's ($t/L \approx 1$). This situation is not supported by our levitation results. Finally, the OVO (Ref. 9) hybrid model predicts the onset of BAS at the unreasonably low temperatures of $T_c' = 40$ K, a condition that is, to our knowledge unsupported by any measurement to date.

While it is clear that TP's modify the superconducting nature of $\text{YBa}_2\text{Cu}_3\text{O}_{7-x}$, the detailed mechanism which induces this modification remains to be identified and/or confirmed. In particular, although our own data and those cited in Refs. 9 and 10 favor the strong-link hypothesis we recognize that there are also many measurements which favor the weak-link picture. A definitive answer to this dilemma may lie with experiments on vortex decoration in the region of the TP's. Vortices should be attracted to (repelled from) the TP boundaries if the TP's are weak (sufficiently strong) links.

We are grateful to M. F. Thorpe, M. Dubson, S. D. Mahanti, R. Viilar, and J. Clem for helpful discussions and to M. Pasos and J. Egiin for technical assistance. This work was supported by the Michigan State University Center for Fundamental Materials Research and by the U.S. National Science Foundation and NASA.

- *Permanent address: Departamento de Física de la Materia Condensada, Universidad Autónoma de Madrid, E-28049 Madrid, Spain.
- ¹T. K. Worthington, W. J. Gallagher, and T. R. Dinger, *Phys. Rev. Lett.* **59**, 1160 (1987).
- ²K. A. Müller *et al.*, *Physica B* (to be published).
- ³I. K. Schuller *et al.*, *Solid State Commun.* **63**, 385 (1987).
- ⁴Y. Yeshurun and A. P. Malozemoff, *Phys. Rev. Lett.* **60**, 2202 (1988).
- ⁵N. Garcia *et al.*, *Z. Phys. B* **70**, 9 (1988).
- ⁶D. Allender, J. Bray, and J. Bardeen, *Phys. Rev. B* **7**, 1020 (1973).
- ⁷S. A. Solin *et al.*, *Phys. Rev. Lett.* **60**, 744 (1988).
- ⁸A. Robledo and C. Varea, *Phys. Rev. B* **37**, 631 (1988).
- ⁹M. M. Faag *et al.*, *Phys. Rev. B* **37**, 2334 (1988), and references therein.
- ¹⁰A. A. Sobyasin and A. A. Stratonnikov (unpublished).
- ¹¹M. K. Wu *et al.*, *Phys. Rev. Lett.* **58**, 908 (1987).
- ¹²J. D. Livingston, A. R. Gaddipati, and R. H. Arendt, in *High-Temperature Superconductors*, edited by M. B. Brodsky, R. C. Dynes, K. Kitazawa, and H. L. Tuller, Materials Research Society Symposia Series Vol. 99 (Materials Research Society, Pittsburgh, 1988).
- ¹³S. Vieira *et al.*, *J. Phys. E* **20**, 1292 (1987).
- ¹⁴L. Krusin-Elbaum, A. P. Malozemoff, and Y. Yeshurun, in *High-Temperature Superconductors*, edited by M. B. Brodsky, R. C. Dynes, K. Kitazawa, and H. L. Tuller, Materials Research Society Symposia Series Vol. 99 (Materials Research Society, Pittsburgh, 1988).
- ¹⁵Shiou-Jyh *et al.*, *Phys. Rev. B* **35**, 7119 (1987).
- ¹⁶J. A. Stratton, *Electromagnetic Theory* (McGraw-Hill, New York, 1941), p. 112.
- ¹⁷R. A. Klemm and J. R. Clem, *Phys. Rev. B* **21**, 1868 (1980).
- ¹⁸P. G. De Gennes, *Superconductivity of Metals and Alloys*, translated by P. A. Pincus (Benjamin, New York, 1966).
- ¹⁹A. Umezawa *et al.* (unpublished).
- ²⁰G. Van Tendeloo, H. W. Zandbergen, and S. Amelinckx, *Solid State Commun.* **63**, 389 (1987).
- ²¹C. H. Chen *et al.*, *Phys. Rev. B* **35**, 8767 (1987).
- ²²A. C. Rose-Innes and E. H. Rhoderick, *Introduction to Superconductivity* (Pergamon, London, 1969), pp. 93-95.
- ²³W. W. Warren *et al.*, *Phys. Rev. Lett.* **59**, 1860 (1987).
- ²⁴I. N. Khlyustikov and A. I. Buzdin, *Adv. Phys.* **36**, 271 (1987).

Layer Rigidity and Collective Effects in Pillared Lamellar Solids

H. Kim,^(a) W. Jin,^(b) S. Lee,^(b) P. Zhou,^(b) T. J. Pinnavaia,^(a) S. D. Mahanti,^(b) and S. A. Solin^(b)

Center for Fundamental Materials Research, Michigan State University, East Lansing, Michigan 48824

(Received 18 November 1987)

The x dependence of the normalized basal spacing, $d_n(x)$, of pillared vermiculite (Vm) has been measured for the mixed-layer system $[(\text{CH}_3)_4\text{N}^+]_x[(\text{CH}_3)_3\text{NH}^+]_{1-x}\text{-Vm}$ and compared with that of $\text{Cs}_x\text{Rb}_{1-x}\text{-Vm}$. Both systems exhibit a nonlinear $d_n(x)$ with approximate thresholds of $x \approx 0.2$ and 0.5 , respectively. A model which related $d_n(x)$ to layer rigidity and the binding energies of gallery and defect sites yields excellent fits to the basal spacing data and to monolayer simulations if collective effects are included. This model should be applicable to other types of lamellar solids.

PACS numbers: 68.65.+g

Lamellar solids constitute a class of materials which exhibit a variety of specific properties. These properties are in large part determined by the host-layer transverse rigidity which characterizes its response to out-of-plane distortions.¹ For example, graphite, whose monatomic amphoteric layers are "floppy" and thus collapse around intercalated guest species, does not sustain a microporous structure with large internal surface area. In contrast, layered aluminosilicate "clays," whose multiautomic fixed-charge layers are "rigid," are unique among lamellar solids in their ability to be pillared² by robust intercalated guest ions which occupy specific lattice sites in the interlayer galleries.³ The resultant pillared clay is characterized by widely spaced host layers that are propped apart by sparsely distributed guest species whose intralayer separation can be many times their diameter. The enormous free volume of accessible interior space that is derived from such an open structure has significant practical implications in the fields of catalysis and selective adsorption (sieving).

Although it is obvious that layer rigidity and pillaring, which is a special example of the more general phenomenon of intercalation, are interrelated, the pillaring mechanism has, to date, been poorly understood. For instance, none of the available elastic models account quantitatively for the full composition dependence of the the c -axis repeat distance of any intercalated layered solid.⁴⁻⁶ It is not surprising that the rigid-layer versions of such models fail when applied to floppy or moderately rigid hosts such as graphite⁷ and layer dichalcogenides.⁸ But they are qualitatively inconsistent with data derived from clay hosts to which rigid-layer models should be most applicable. Accordingly, we report in this paper the first successful attempt to quantify and parametrize the relation between pillaring and layer rigidity. To accomplish this we have carried out x-ray and simulation studies of the x dependence of the basal spacing, $d(x)$, of mixed-layer vermiculite (Vm) clays $A_xB_{1-x}\text{-Vm}$, $0 \leq x \leq 1$, where A and B are cations (assume that A is larger than B) that are judiciously chosen to elucidate the physics of pillaring. In a previous study⁶ we exam-

ined the $\text{Cs}_x\text{Rb}_{1-x}\text{-Vm}$ system for which the alkali intercalate species are best characterized as "puny" pillars since their ionic diameters are only 3.34 and 2.92 Å, respectively. Here we focus on the more robust mixed pillar system tetramethyl ammonium-trimethyl ammonium-vermiculite with effective diameters of 4.8 and 4.0 Å, respectively. We find that the pillaring process is a collective phenomenon which introduces an intrinsic nonlinearity in $d(x)$. While our results are deduced for clay intercalation compounds (CIC's) they should also be applicable to other lamellar solids.

Vermiculite is a trioctahedral 2:1 layered silicate. Its layers are formed from a sheet of edge-connected octahedra ($M^{\text{VI}} = \text{Mg, Al, Fe}$) which is bound to two sheets of corner-connected tetrahedra ($M^{\text{IV}} = \text{Si, Al}$) as shown in the inset of Fig. 1. The layers of oxygen atoms which terminate the clay layers are arranged in a kagomé lattice whose hexagonal pockets form a triangular lattice of gallery sites which here are constrained by the requirement of overall charge neutrality to be occupied by the gallery exchange cation. This occupation imposes a lateral registration of adjacent clay layers as indicated in the inset of Fig. 1. To synthesize the specimens studied here, the Mg^{2+} gallery cations which link the layers of natural Llano vermiculite were exchanged for $(\text{CH}_3)_3\text{NH}^+$ ions with ethylenediaminetetraacetate as a complexant. Subsequent exposure of pure $[(\text{CH}_3)_3\text{NH}^+]\text{-Vm}$ to the proper amount of $(\text{CH}_3)_4\text{N}^+$ yielded a solid-solution pillared CIC



Self-supporting sedimented films exhibited a mosaic spread of $\approx 5^\circ$ with the layers parallel to the substrate.

The x dependence of the (001) x-ray diffraction patterns of $[(\text{CH}_3)_4\text{N}^+]_x[(\text{CH}_3)_3\text{NH}^+]_{1-x}\text{-Vm}$ is shown in Fig. 1. The starred reflections in that figure are from a small concentration of an impurity phase whose 14.477-Å basal spacing is x independent as evidenced by the vertical line in Fig. 1. The patterns in Fig. 1 can be well accounted for by a structure-factor calculation for a 25-layer stack.⁷ We have also attempted to fit the pat-

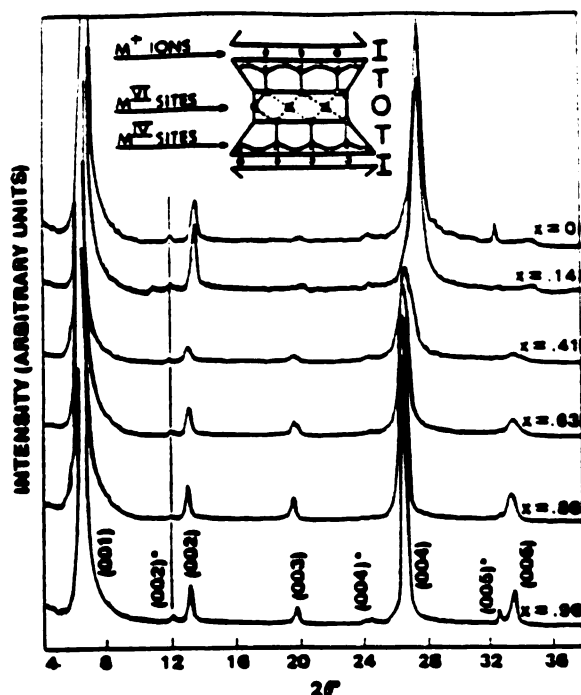


FIG. 1. Room-temperature x-ray diffraction patterns of $[(\text{CH}_3)_4\text{N}^+]_x[(\text{CH}_3)_3\text{NH}^+]_{1-x}\text{-Vm}$ excited by $\text{Cu K}\alpha$ radiation (filled circles). Starred reflections are from an impurity phase. The solid vertical line shows the constant position of the $(002)^\circ$ reflection; Inset: Schematic structure of a 2:1 layered aluminosilicate clay with the tetrahedral (T) and octahedral (O) sheets which bound intercalated ions (I) (see text).

terms of Fig. 1 using a Hendricks-Teller (HT) model⁶ for an interstratified structure.⁷ The HT calculations yielded results which were clearly inferior to those based on a solid-solution arrangement in which all galleries have the same height. Moreover, a one-dimensional Patterson synthesis⁸ from the measured peak intensities did not show any sign of interstratification.

From the data of Fig. 1, we have determined the x dependence of the normalized basal spacing,⁶ $d_n(x)$ (or normalized c -axis repeat distance), of $[(\text{CH}_3)_4\text{N}^+]_x[(\text{CH}_3)_3\text{NH}^+]_{1-x}\text{-Vm}$ which is shown in Fig. 2 as filled squares. Here $d_n(x) = [d(x) - d(0)] / [d(1) - d(0)]$ where $d(x)$ is the observed basal spacing. Also shown in Fig. 2 for comparison are corresponding results for $\text{Cs}_x\text{Rb}_{1-x}\text{-Vm}$ (Ref. 6) (open squares). Both the Cs-Rb and $(\text{CH}_3)_4\text{N}^+-(\text{CH}_3)_3\text{NH}^+$ systems exhibit a non-Vegard's-law (nonlinear) rapid rise in $d_n(x)$ with increasing x at "threshold" values of $x_c = 0.5$ and 0.2 , respectively.

To understand the physical origin of the observed $d_n(x)$, we have simulated a model monolayer system with finite transverse layer rigidity. For simplicity we assumed that the intercalate ions are hard spheres.

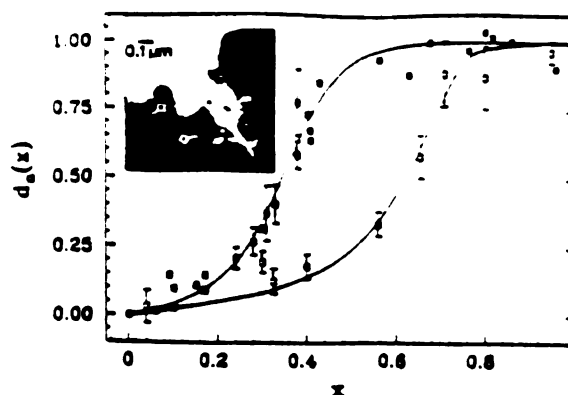


FIG. 2. The composition dependence of the normalized basal spacing of $[(\text{CH}_3)_4\text{N}^+]_x[(\text{CH}_3)_3\text{NH}^+]_{1-x}\text{-Vm}$ (filled squares) and $\text{Cs}_x\text{Rb}_{1-x}\text{-Vm}$ (open squares). The solid lines are least-squares fits to the data with Eq. (4) of the text. Inset: Bright-field scanning-tunneling micrograph of $(\text{CH}_3)_3\text{NH}^+\text{-Vm}$ acquired at $T = -135^\circ\text{C}$ with the electron beam normal to the layers. Note the free surface between layer edge dislocations (outline-headed arrows), the folded region (lozenges), and the microcrack (open-headed arrows). The small dotted grids are an instrumental artifact.

Starting from a two-dimensional triangular lattice of lattice constant a_0 representing a single gallery with each lattice site occupied by a B ion of height d_B , we randomly replace the B ions with A ions of height $d_A > d_B$. The height of a cell within a healing length λ of the A ion is also increased to d_A . A second A ion in this region does not affect already expanded cells but expands unexpanded cells within λ of its location. The process of random replacement of the B ions continues to saturation. If we define $a(x)$ as the fraction of cells with height d_A , then $d_n(x) = a(x)$. The simulation results for $d_n(x)$ are shown in Fig. 3 for several different healing lengths. Clearly, in the floppy-layer limit $\lambda = 0$, a Vegard's-law behavior obtains whereas the initial slope $[d_n(x)]_{x=0} \rightarrow \infty$ as $\lambda \rightarrow \infty$. As can be seen from Fig. 3, there is no percolation threshold even for finite λ because $d_n(x)$ depends upon all of the large ions, not only on those belonging to the infinite percolation cluster. Note that the nonlinearity in $d_n(x)$ for $\lambda > 0$ is a collective effect associated with the individual interaction between the larger ions through their distortion fields.

The sublinear x dependence and the rapid rise in $d_n(x)$ near x_c is outside the monolayer model. Several mechanisms including the relative magnitudes of host-guest and host-host interactions, interlayer correlations, and the presence of defect (d) sites can produce sublinear behavior in $d_n(x)$ but only the latter two can generate threshold effects. Since the ions of interest here are relatively incompressible we treat the guest species as hard spheres as noted above. The interlayer correlation mechanism is one in which large guest ions locally pack-

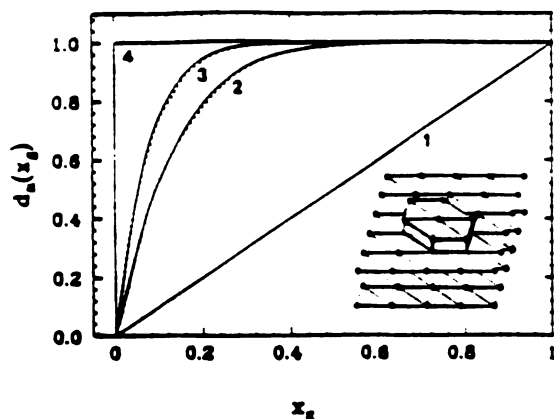


FIG. 3. Monolayer triangular lattice computer simulations (dotted lines) of the composition dependence of the normalized basal spacing of a ternary intercalation compound for several values of the healing length, λ , and rigidity parameter, ρ . The solid lines are from Eq. (4) of the text with (1) $\rho=1$, $\lambda=0$; (2) $\rho=7$, $\lambda=a_0$; (3) $\rho=13$, $\lambda=\sqrt{3}a_0$; and (4) $\rho=\infty$, $\lambda=\infty$. Inset: The puckered region of a triangular lattice with $\lambda=a_0$. Here the number of expanded sites is $\rho=Z+1=7$ where Z is the number of nearest neighbors.

er the bounding layers so that at low x they adopt staggered lateral positions, i.e., no line joining the centers of any pair of large ions in adjacent galleries is perpendicular to the silicate layer. This mechanism is relevant to host materials with low transverse layer rigidity such as graphite while the d -site mechanism is more appropriate to the more rigid layers of clays.

Sources of d sites in our specimens are shown in a scanning tunneling electron micrograph of $(\text{CH}_3)_3\text{NH}^+ \cdot \text{Vm}$ (inset, Fig. 2). The region imaged consists of homogeneously intercalated areas (g sites) which are bounded laterally by layer edge dislocations and are capped by free surfaces (d sites) that bind guest species without inducing c -axis expansion. Since the clay grains have typical basal dimensions of a few micrometers, it is clear from the scale of the micrograph that these free surfaces can represent a significant fraction of the total surface available to guest species. Additional minor sources of d sites are the microcracks and folds that are visible in the micrograph.

We have explored the d -site mechanism by constructing a two-site model in which the basal spacing is assumed to depend upon the gallery A -ion concentration x_g which itself is a function of the total A -ion concentration x . The functional dependence of x_g on x is determined by two parameters, f and Δ/kT , where $f=N_d/N_g$ is the fraction of ions in d sites relative to those in g sites and Δ is the effective binding-energy difference between these sites, the d sites having a lower binding energy. For simplicity we assume only one type of d site. A statistical

mechanics calculation gives

$$x_g = 1/(z+1), \quad (1)$$

$$x = [1/(1+f)]x_g + [f/(1+f)]\{1/[z \exp(-\Delta/kT) + 1]\}, \quad (2)$$

where $z = \exp[(\epsilon_g - \mu)/kT]$ is related to the fugacity and the binding energy ϵ_g of the g sites. Equations (1) and (2) can be solved to obtain $x_g = \phi(x, f, \Delta/kT)$ for different values of f and Δ/kT . Physically then for $x < x_c$, the A ions first preferentially displace B ions from the d sites. This reduces the gallery A -ion concentration for a given x and yields a sublinear increase in $d_n(x)$. For $x > x_c$, additionally ingested A ions enter the galleries. The result is a rapid increase in $d_n(x)$.

Using methods developed by Xia and Thorpe¹⁰ one can obtain the following analytic solution for our monolayer simulation:

$$d_n(x_g) = 1 - (1-x_g)^\rho, \quad 0 \leq x_g \leq 1, \quad (3)$$

where ρ is a layer rigidity parameter. This equation fits the simulation data extremely well as shown by the dotted lines in Fig. 3. For our lattice-gas simulation, $\rho = Z+1$ where Z is the number of neighboring sites that are puckered by the insertion of an isolated A ion (see inset Fig. 3). In the continuum limit ($\lambda \gg d_A/2$), $\rho \sim (2\lambda/d_A)^2$. Using Eq. (3) and $x_g = \phi(x, f, \Delta/kT)$, we obtain

$$d_n(x) = 1 - \{1 - \phi(x, f, \Delta/kT)\}^\rho. \quad (4)$$

Note that the slope of $d_n(x)$ at $x \geq x_c$ is governed by a combination of ρ and Δ/kT while x_c is determined primarily by f for large Δ/kT .

We have used Eq. (4) to obtain a nonlinear least-squares fit to the data of Fig. 2. The parameter values which give very good fits (solid lines in Fig. 2) for the two CIC systems $\{[(\text{CH}_3)_4\text{N}^+]_x [(\text{CH}_3)_3\text{NH}^+]_{1-x} \cdot \text{Vm}\}$ and $\text{Cs}_x\text{Rb}_{1-x} \cdot \text{Vm}$ are $\{\rho=8.0, f=0.5, \Delta/kT=4.3\}$ and $\{\rho=7.0, f=2.2, \Delta/kT=4.1\}$, respectively. The smaller value of the rigidity parameter in the Cs-Rb system is consistent with the fact that alkali ions in CICs can partially penetrate the bounding silicate layers. The mechanism which gives rise to this penetration is a torsional in-plane distortion^{1,6} of the tetrahedral sheets which expands the hexagonal pockets that contain the guest species. Ion penetration of the clay layers causes a reduction of the apparent healing length. But the $(\text{CH}_3)_4\text{N}^+$ and $(\text{CH}_3)_3\text{NH}^+$ ions are much too large to penetrate the clay layer significantly, even in the presence of torsional distortions. Thus one expects the Cs-Rb-Vm system to exhibit a lower value of the rigidity parameter ρ . The f values deduced for the two systems also reveal interesting properties of the clay structure. For singly ionized guest species $N_j = \sigma A_j$, where σ is the layer charge density and A_j is the surface area asso-

erated with j sites, $j=d,g$. If $A=A_d+A_g$ then $A_d = [j/(1+j)]A$ and $(A_d)_{Cs-Rb} / (A_d)_{(CH_3)_4N^+ - (CH_3)_3NH^+} \cong 2$. Thus, of the surface which provides d sites for small Cs-Rb ions only about half (the portion not adjacent to edge dislocations, or derived from some microcracks or folds) can also accommodate the robust $(CH_3)_4N^+$ - $(CH_3)_3NH^+$ ions without inducing basal expansion. Finally, the difference in the Δ/kT values for the two pairs indicates that the d sites are more attractive for the larger ions. This makes physical sense because the more spatially demanding ions prefer the less constrained defect environment to the more restrictive gallery.

The layer rigidity model which we have developed here should be directly applicable to other lamellar solids such as zirconium phosphates and layered niobates which have relatively rigid layers. It can also give insight into the behavior of intercalation compounds whose host layers have low or moderate rigidity. For example Li_xC_6 (Ref. 4) and Li_xTiS_2 ¹¹ exhibit no threshold in $d_s(x)$, and therefore contain few if any d sites. Also, there are conflicting reports of a Vegard's-law $d_s(x)$ for $Rb_xK_{1-x}C_8$ prepared from single-crystal graphite¹² and a thresholdlike sublinear behavior for the same compound prepared single-crystal graphite,¹³ highly oriented pyrolytic graphite,¹⁴ or powder.¹⁵ For clay hosts sublinear threshold behavior can be reasonably associated with d sites. But for floppy-layer hosts such as graphite there is much evidence¹⁵ that interlayer correlations and their associated strain fields dominate the behavior. Therefore, even though the non-Vegard's-law behavior of $Rb_xK_{1-x}C_8$ (Ref. 12) has been attributed to d sites, we do not believe that the model addressed here is applicable to that compound.

Finally, we have assumed that the site binding energies in our model are independent of concentration. This assumption might be relaxed if the binding energy of the g sites drops once the galleries are initially expanded.

The resultant transfer of ions from d to g sites would then contribute to the rapid increase in $d_s(x)$ for $x \geq x_c$.

We thank M. F. Thorpe for the derivation of Eq. (3). Useful discussions with H. X. Jiang and Y. B. Fan are acknowledged. This work was supported by the National Science Foundation under Materials Research Center Grant No. DMR 85-14154 and in part by the Center for Fundamental Materials Research of Michigan State University.

^(a)Department of Chemistry.

^(b)Department of Physics and Astronomy.

¹S. A. Solin, in *Intercalation in Layered Materials*, edited by M. S. Dresselhaus (Plenum, New York, 1986), p. 145.

²T. J. Pennavaia, *Science* **220**, 365 (1983).

³Unlike graphite which is amphoteric, clays have a fixed layer charge. Intercalation in these materials is thus an intragallery ion-exchange process.

⁴There is one exception, $K(NH_4)_2C_{24}$, whose superlinear x -dependent basal spacing is qualitatively distinct from that of clays but is well accounted for by a rigid-layer model which includes both elastic and electronic effects. See B. R. York and S. A. Solin, *Phys. Rev. B* **31**, 8206 (1985).

⁵J. E. Fischer and H. J. Kim, *Phys. Rev. B* **35**, 3295 (1987), and references therein.

⁶B. R. York *et al.*, *Solid State Commun.* **54**, 475 (1985).

⁷H. Kim *et al.*, to be published.

⁸S. Hendricks and E. Teller, *J. Chem. Phys.* **10**, 147 (1942).

⁹D. M. C. MacEwan, *Nature (London)* **171**, 616 (1953).

¹⁰W. Xia and M. F. Thorpe, *Phys. Rev. A* (to be published).

¹¹J. R. Dahn, D. C. Dahn, and R. R. Haering, *Solid State Commun.* **42**, 179 (1982).

¹²D. Medjahed, R. Merlin, and R. Clarke, *Phys. Rev. B* **36**, 9345 (1987).

¹³P. Chow and H. Zabel, to be published.

¹⁴P. Chow and H. Zabel, *Synth. Met.* **7**, 243 (1983).

¹⁵S. A. Solin and H. Zabel, *Adv. Phys.* (to be published).

MICHIGAN STATE UNIV. LIBRARIES



31293008820320